

GDANSK UNIVERSITY OF TECHNOLOGY
FACULTY OF OCEAN ENGINEERING AND SHIP TECHNOLOGY
SECTION OF TRANSPORT TECHNICAL MEANS
OF TRANSPORT COMMITTEE OF POLISH ACADEMY OF SCIENCES
UTILITY FOUNDATIONS SECTION
OF MECHANICAL ENGINEERING COMMITTEE OF POLISH ACADEMY OF SCIENCE

ISSN 1231 – 3998
ISBN 83 – 900666 – 2 – 9

Journal of

POLISH CIMAC

**SELECTED PROBLEMS
OF DESIGNING
AND OPERATING
TECHNICAL SYSTEMS**

Vol. 8

No. 3

Gdansk, 2013

Science publication of Editorial Advisory Board of POLISH CIMAC

Editorial Advisory Board

- J. Girtler** (President) - *Gdansk University of Technology*
L. Piaseczny (Vice President) - *Naval Academy of Gdynia*
A. Adamkiewicz - *Maritime Academy of Szczecin*
J. Adamczyk - *University of Mining and Metallurgy of Krakow*
J. Blachnio - *Air Force Institute of Technology*
C. Behrendt - *Maritime Academy of Szczecin*
P. Bielawski - *Maritime Academy of Szczecin*
T. Chmielniak - *Silesian Technical University*
R. Cwilewicz - *Maritime Academy of Gdynia*
T. Dąbrowski - *WAT Military University of Technology*
Z. Domachowski - *Gdansk University of Technology*
C. Dymarski - *Gdansk University of Technology*
M. Dzida - *Gdansk University of Technology*
J. Gronowicz - *Maritime University of Szczecin*
V. Hlavna - *University of Žilina, Slovak Republic*
M. Idzior - *Poznan University of Technology*
A. Iskra - *Poznan University of Technology*
A. Jankowski - *President of KONES*
J. Jaźwiński - *Air Force Institute of Technology*
J. Kiciński - *Member of MEC*
O. Klyus - *Maritime Academy of Szczecin*
Z. Korczewski - *Gdansk University of Technology*
K. Kosowski - *Gdansk University of Technology*
L. Ignatiewicz Kowalczyk - *Baltic State Maritime Academy in Kaliningrad*
J. Lewitowicz - *Air Force Institute of Technology*
K. Lejda - *Rzeszow University of Technology*
J. Macek - *Czech Technical University in Prague*
Z. Matuszak - *Maritime Academy of Szczecin*
J. Merksiz - *Poznan University of Technology*
R. Michalski - *Olsztyn Warmia-Mazurian University*
A. Niewczas - *Motor Transport Institute*
Y. Ohta - *Nagoya Institute of Technology*
M. Orkisz - *Rzeszow University of Technology*
S. Radkowski - *Member of MEC*
Y. Sato - *National Traffic Safety and Environment Laboratory, Japan*
M. Sobieszczanski - *Bielsko-Biala Technology-Humanistic Academy*
A. Soudarev - *Russian Academy of Engineering Sciences*
Z. Stelmasiak - *Bielsko-Biala Technology-Humanistic Academy*
Z. Smalko - *Air Force Institute of Technology*
M. Ślęzak - *Automotive Industry Institute*
W. Tarelko - *Maritime Academy of Gdynia*
W. Wasilewicz Szczagin - *Kaliningrad State Technology Institute*
F. Tomaszewski - *Poznan University of Technology*
J. Wajand - *Lodz University of Technology*
W. Wawrzyński - *Warsaw University of Technology*
E. Wiederuh - *Fachhochschule Giessen Friedberg*
M. Wyszyński - *The University of Birmingham, United Kingdom*
S. Żmudzki - *West Pomeranian University of Technology in Szczecin*
B. Żóltowski - *Bydgoszcz University of Technology and Life Sciences*
J. Żurek - *Air Force Institute of Technology*

Editorial Office:

GDANSK UNIVERSITY OF TECHNOLOGY
Faculty of Ocean Engineering and Ship Technology
Department of Ship Power Plants
G. Narutowicza 11/12 80-233 GDANSK POLAND
tel. +48 58 347 29 73, e – mail: sek4oce@pg.gda.pl

www.polishcimac.pl

This journal is devoted to designing of diesel engines, gas turbines and ships' power transmission systems containing these engines and also machines and other appliances necessary to keep these engines in movement with special regard to their energetic and pro-ecological properties and also their durability, reliability, diagnostics and safety of their work and operation of diesel engines, gas turbines and also machines and other appliances necessary to keep these engines in movement with special regard to their energetic and pro-ecological properties, their durability, reliability, diagnostics and safety of their work, and, above all, rational (and optimal) control of the processes of their operation and specially rational service works (including control and diagnosing systems), analysing of properties and treatment of liquid fuels and lubricating oils, etc.

All papers have been reviewed

@Copyright by Faculty of Ocean Engineering and Ship Technology Gdansk University of Technology

All rights reserved

ISSN 1231 – 3998

ISBN 83 – 900666 – 2 – 9

Printed in Poland



Introduction

In contemporary science we can observe more and more specialization in various scientific disciplines. This specialization makes that research is conducted with not proper consideration of the knowledge of other scientific disciplines even if they belong to the same field of knowledge. Thus, the specialists dealing with the theme that belongs to the „Machine Building and Operating” discipline, are reluctant to study achievements of the related disciplines such as: „Automation and Robotics”, „Electronics”, „Electrical Engineering”, „Energetics”, „Computer Science”, „Mechanics” or “ Transport”. Much more unconcerned is the knowledge of such disciplines as: „Biocybernetics & Biomedical Engineering” and „Biotechnology”, although they are classified to the field of knowledge defined as „technical sciences”. The situation is understandable. It follows from the anxiety that study of developments in other scientific disciplines may cause falling behind with developments in the discipline practiced by the given scientist. In consequence, making a Doctoral Thesis can be admittedly easier but making a Habilitation Thesis – much more difficult. Habilitation can be achieved among others when a candidate in his/her research output can prove application for the first time the knowledge of any other discipline, e.g. „Mathematical Sciences”.

In each scientific discipline, independently which field of knowledge it belongs to, the science is being developed in result of applying proper scientific methods. However, regardless of application of the specific methods, in each scientific discipline there are also used deductive and inductive methods if the created knowledge is supposed to have essential cognitive properties. Deductive methods are used when it is necessary to prove a thesis statement (statements). When a hypothesis (hypotheses) is (are) to be verified then the inductive or deductive methods are applied. As a rule, underestimated is the method called analogy. The analogy, however, enables searching for a common *reason (rationale, cause)* characterizing different research objects (specific for particular scientific disciplines), while deduction consists in matching *consequence (result, conclusion)* to *reason*, and induction – *reason to consequence*.

For this reason it might be of interest to many scientists and also beneficial for development of technical sciences to present in the *Journal of POLISH CIMAC* designed for publication of articles concerning the knowledge enclosed in the „Machine Building and Operating” discipline, also these works which are classified to other mentioned scientific disciplines belonging to the field of knowledge - „technical sciences”, although they are not directly related to the theme being the mainstream of this journal. This volume contains precisely this kind of publications. I remain with the conviction that such an approach to the dissemination of knowledge comprising both cognitive properties (important for science) and utilitarian properties (important in practice of designing, manufacturing and operating technical equipment), will contribute to accelerating the development of the technical sciences.

Editor-in-Chief
prof. Jerzy Girtler

CONTENTS

Cichański A., Burak M., Stopel M.: NUMERICAL ANALYSIS OF FRAME STRUCTURE OF SINGLE AXIS MANURE SPREADER	9
Cichański A., Skibicki D., Lis Z., Burak M., Stopel M.: STRAIN GAUGE VERIFICATION OF NUMERICAL CALCULATIONS OF FRAME STRUCTURE OF SINGLE AXIS MANURE SPREADER	15
Domanowski P., Wocianiec R.: EXPOSURE OF PRINTED CIRCUITS BY SUB-PIXEL SCROLL METHOD	25
Ławrynowicz Z.: AFFECT OF CEMENTITE PRECIPITATION ON THE EXTEND OF BAINITE REACTION IN ADI	31
Leppert T.: CUTTING FORCES IN DRY AND NEAR DRY CUTTING OFF MACHINING	37
Mroziński M., Piotrowski M., Burak M., Pejkowski Ł.: INFLUENCE OF CONNECTION TYPE ON THE FATIGUE LIFE OF WELDED	45
Pejkowski Ł., Skibicki D., Burak M., Piotrowski M.: FATIGUE BEHAVIOR OF PURE COPPER IN NON-PROPORTIONAL LOAD CONDITIONS	57
Pepliński K.: ASSESSMENTS OF THE IMPACT EXTRUSION DIE GAP ON THE QUALITY IN TECHNICAL BLOWING PRODUCT	63
Pepliński K.: SELECTED ASPECTS OF VIRTUAL PROTOTYPING THE BLOWING PREFORM PROCESS IN THE ANSYS-POLYFLOW SOFTWARE	69
Piątkowski T.: RESEARCH ON ELASTIC-DAMPING PROPERTIES OF UNIT LOADS	75
Sadowski J.: THE PROBLEM OF ASSESSMENT OF INITIAL POINT OF CRACK DEVELOPMENT IN IMPACT BENDING TEST	83
Skibicki D., Burak M., Pejkowski Ł., Piotrowski M.: STRUCTURAL ANALYSIS OF THE FAN SECTION OF THE AIR HANDLING UNIT ON DYNAMIC LOAD DEFINED BY SEISMIC SPECTRUM	93
Strzelecki P., Sempruch J.: PROBABILISTIC APPROACH FOR ANALITICALLY-DETERMINED FATIGUE CURVE	103
Tomaszewski T., Sempruch J.: MULTIFRACTAL SCALING LAW FOR HIGH-CYCLE FATIGUE STRENGTH APPLIED TO ALUMINUM ALLOY	109
Wirwicki M., Topoliński T.: ANALYSIS OF THE WEIBULL DISTRIBUTION FOR STATIC 3-POINT BENDING OF ZIRCONIUM DIOXIDE	117
Zachwieja J.: VIBRATION SUPPRESSION PROBLEMS IN NON-RIGID STRUCTURES TAKING A VIBRATING SIFTER AS AN EXAMPLE	123

NUMERICAL ANALYSIS OF FRAME STRUCTURE OF SINGLE AXIS MANURE SPREADER

Artur Cichański, Michał Burak, Michał Stopel

*University of Technology and Live Sciences in Bydgoszcz
ul. Kaliskiego 7, 85-789 Bydgoszcz, Poland
tel.: +48 52 3408235, fax: +48 52 3408245
e-mail: artur.cichanski@utp.edu.pl*

Abstract

The study describes issues of research of frame structure of single axis manure spreader of loading capacity 14t. During the tests state of stress in frame structure and manure box have been specified. Manner of preparation of numerical model and results of tests performed with its use have also been described. On the basis of the results modification of the construction in critical areas has been proposed. Introduction of modifications resulted in improvement of frame structure of manure spreader strength state.

Keywords: *agricultural machinery, manure spreader, construction testing, FEM, ANSYS,*

1. Introduction

One of the most crucial factors having impact on frame structure of manure spreader is a number of axis of driving system. The most common are single and double axis solutions, more rare triple axis solutions applied when huge loading capacity is required. In case of single axis spreaders (Fig. 1) significant portion of load is transmitted by rear axis of a tractor resulting in increase of vehicle thrust force due to reduction of sliding of driving wheels [2].



Fig. 1. The tested manure spreader

Lower load present in case of a single spreader allows for application of smaller driving wheels. The advantages of such solutions are, connected with tyre diameter, lesser resistances of rolling, and, connected with tyre width, reduced soil compaction. As for spreader rolling on the field greater portion of tractor power is used, reduction of specified movement losses results in reduction of tractor fuel consumption [1].

2. Obiekt i warunki badań

The tested object was frame structure of a single axis manure spreader of loading capacity 14t. The main element of spreader equipment is a double drum manure spreading adapter. Mounted in rear part of manure box, the adapter with vertical system of drums is driven by mechanical gear. Characteristic dimensions of the analysed object are specified in Fig. 2. The welded frame is made of steel S235JR.

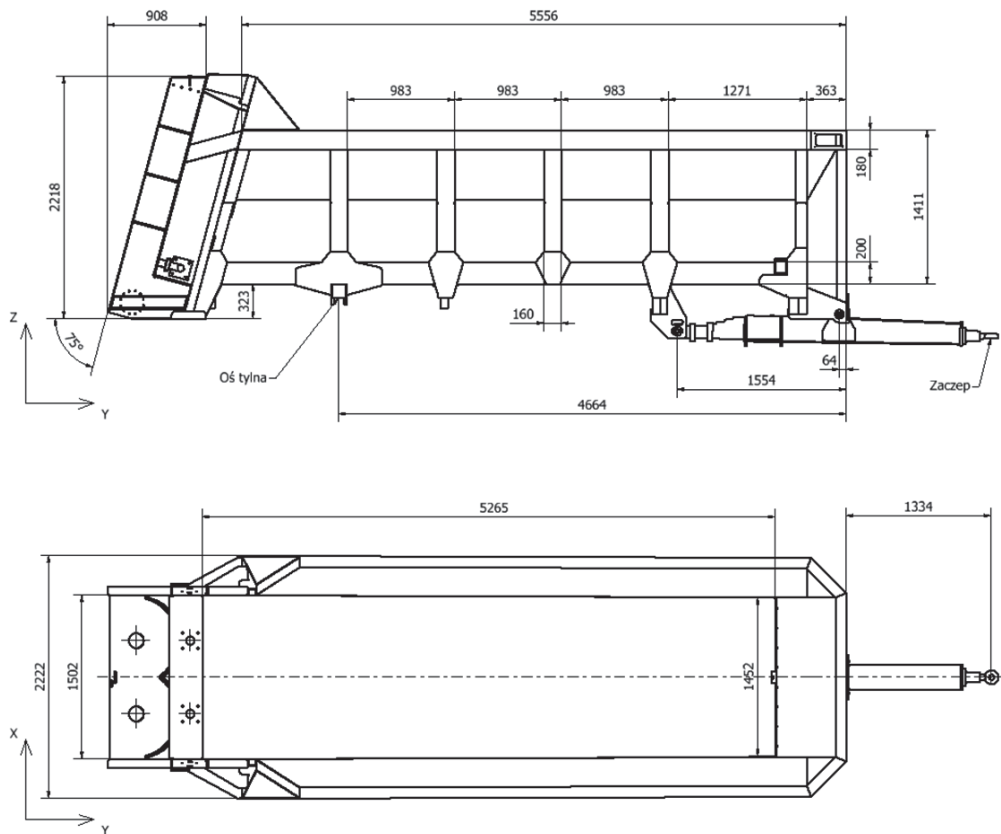


Fig. 2. Size dimensions of manure spreader

In its rear part spreader is supported in two points located on both ends of rear axis. To this axis the wheels are mounted. In its front part spreader is supported in one point, corresponding with joint for single axis trailers. Total load of frame structure of manure spreader consists of: manure mass 14 000 kg, mass of two manure spreading adapters 2x160 kg and mass of two gears for adapters driving 2x250 kg. The analyses take into account the frame structure weight of its own.

3. Conditions of performance of numerical analyses

Numerical tests were performed with a method of finite elements [3] in ANSYS Workbench environment. On the basis of geometric models of frame structure of manure spreader, shell mesh was prepared. For analyses boundary conditions were selected in such manner that at rear supports translation degrees of freedom were fixed in direction 0Y (Fig. 3). At front support the condition of *Remote displacement* [4] type was specified, fixing all three degrees of freedom. Main load resulting from manure mass was distributed on the whole floor surface.

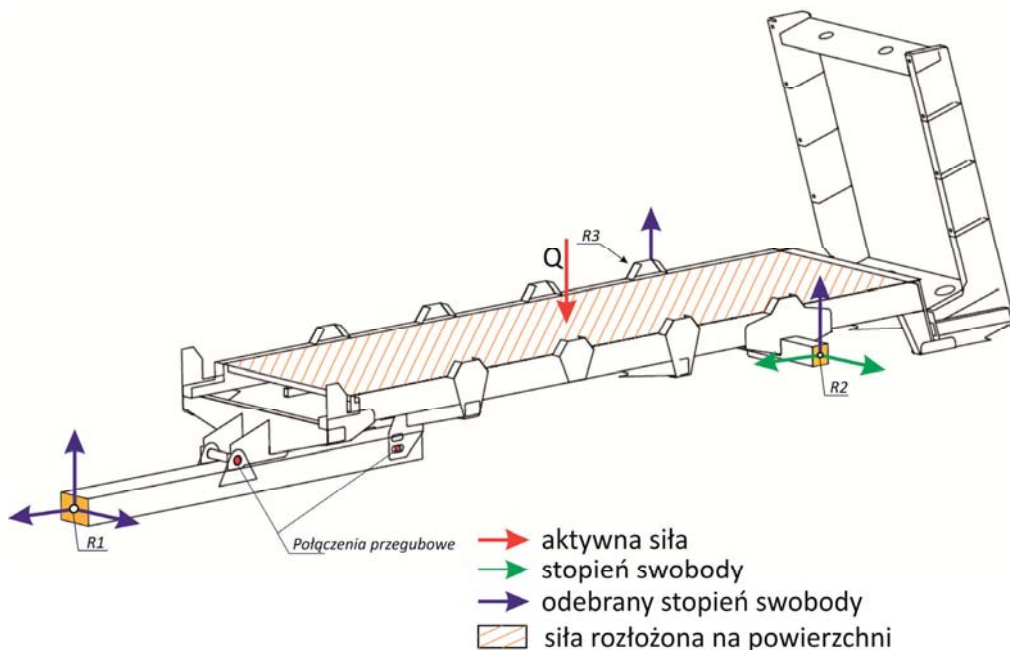


Fig. 3. Diagram of selection of threshold conditions for manure spreader

For the analyses it was assumed that in bottom part of applicator frame there should be two forces applied $P=2.5$ kN representing transmission gears. The forces were applied to right and left side of applicator frame assigning them appropriate index on Fig. 4. Applicator rotors were mapped by forces $W=1.6$ kN with appropriate index on Fig. 4. It was assumed that forces W should be applied at points of rotors bearing mounting locations.

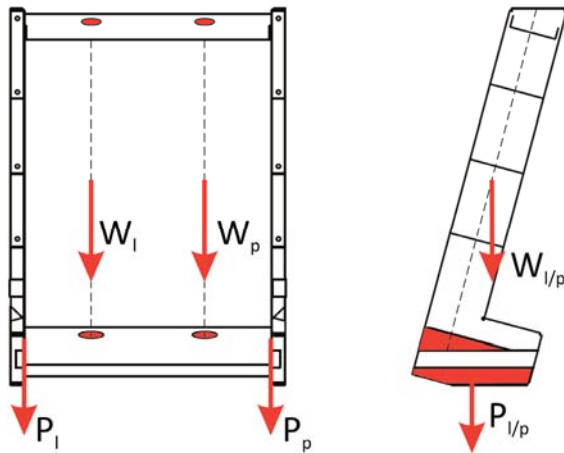


Fig. 4. Diagram of distribution of load on applicator frame

4. Numerical tests and modification of frame structure

After preparation of mesh and defining of material properties and boundary conditions numerical solution of the problem was achieved. Calculation results were presented in the form of stress distribution on frame structure in Fig. 5.

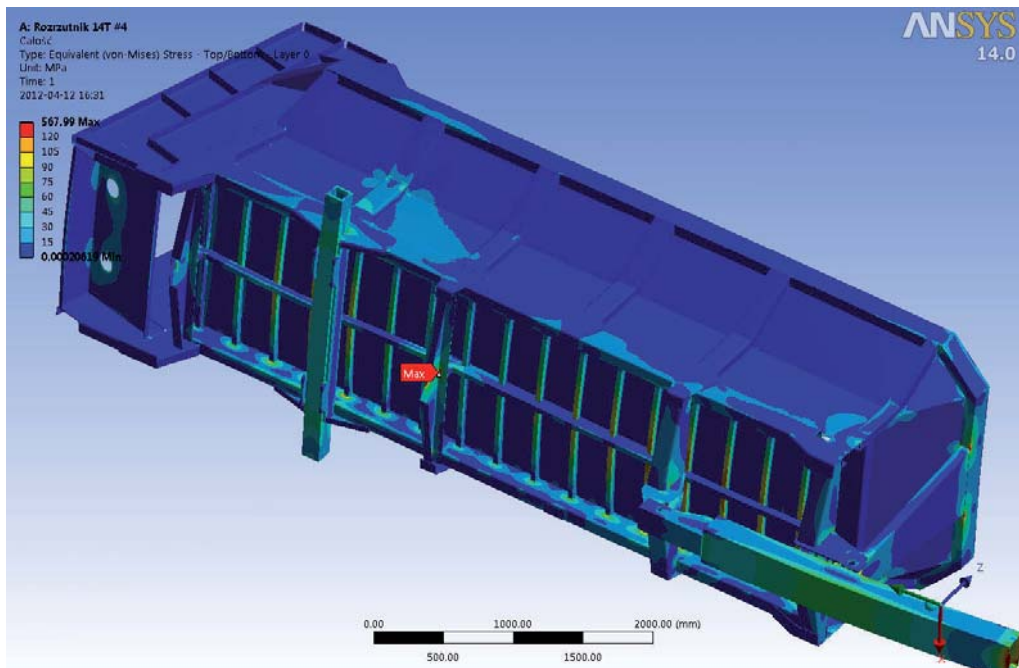


Fig. 5. Distribution of reduced stresses on spreader frame prior to modifications

It was noted that specified values of maximum stresses significantly exceed permitted stresses for the frame. Extreme stress identified with symbol Max in Fig. 5 is present in support of third horizontal beam, numbered in sequence from tow bar side. Also, exceeding of permitted

stresses was noted on supports of remaining beams and on the very beams. In order to improve the condition of frame strength state modifications of elements, in which the highest stress was noted, were proposed. For the purpose of analyses the following were changed:

- supports of horizontal beams (Fig. 6, item 1). Their thickness was increased to 6mm. To 10 mm thickness of support located over third horizontal beam, numbered in sequence from tow bar side, was changed;
- first horizontal beam, numbered in sequence from tow bar side (Fig. 6, item 2). Thickness was increased to 8mm;
- second horizontal beam, numbered in sequence from tow bar side (Fig. 6, item 3). Thickness was increased to 7mm;
- third horizontal beam, numbered in sequence from tow bar side (Fig. 6, item 4). Thickness was increased to 9mm;
- main beam bottom (Fig. 6, item 5). Thickness was increased to 7mm;
- top front beam (Fig. 6, item 6). Thickness was increased to 7mm;
- front tow bar support (Fig. 6, item 7). Thickness was increased to 16mm.

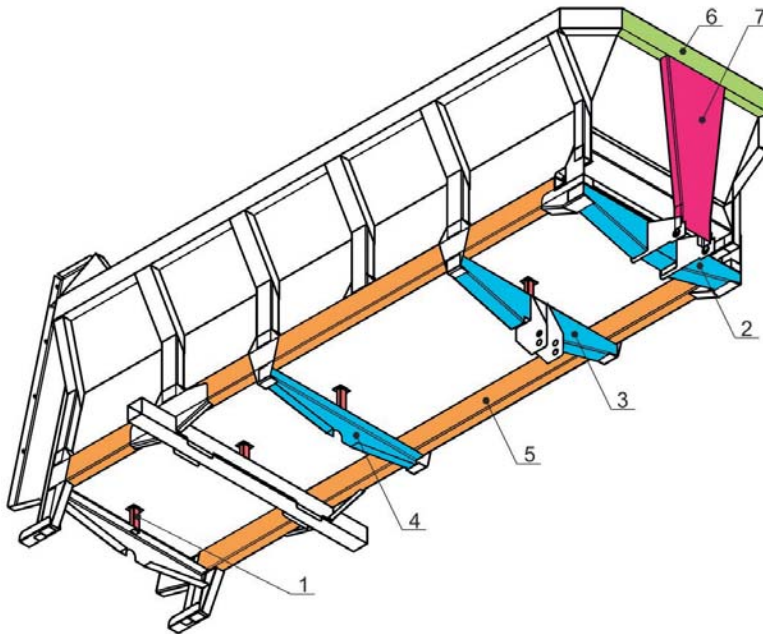


Fig. 6. Modified elements

After introduction of modifications of geometric form for unchanged boundary conditions, numerical analyses were repeated. Calculation results were presented in the form of distribution of stresses in frame in Fig. 7.

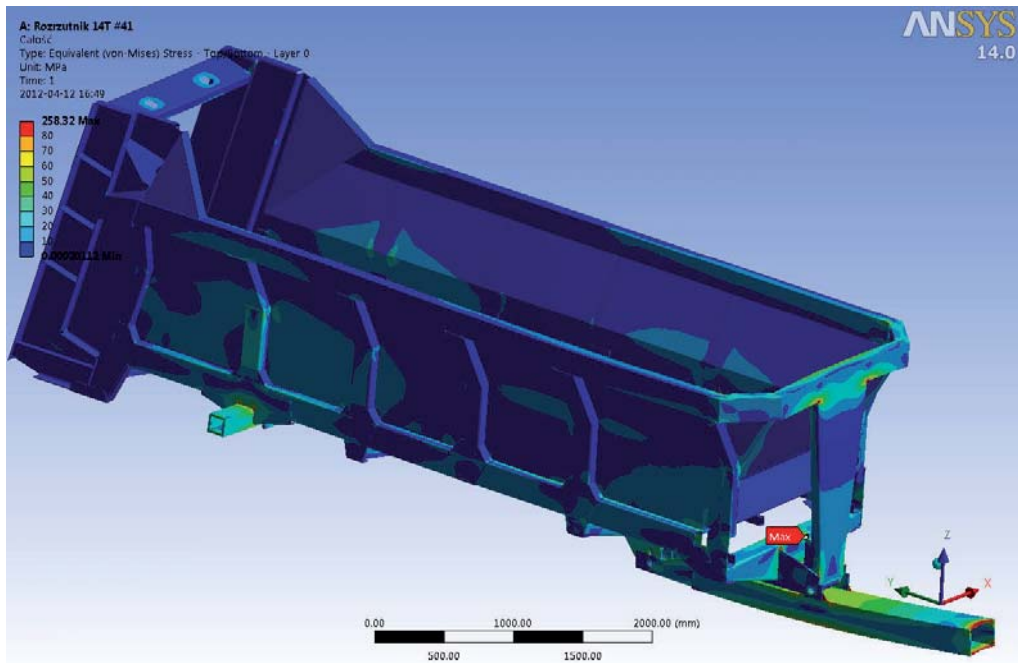


Fig. 7. Distribution of reduced stresses on spreader frame after modifications

5. Summary

The study presents conditions of conducting and results of numerical analyses of frame structure of a single axis manure spreader. After performing of calculations significant exceeding of values of permitted stress on horizontal beams and their supports were noted. Also exceeding of permitted stresses on main load bearing beam and on tow bar support and cooperating top front beam were stated. In order to reduce stresses on critical frame joints constructional modifications were proposed. Introduction of such modifications resulted in improvement of the construction strength state.

As a result of performed calculations information on stresses, which due to degree of construction complexity could not be determined analytically, was obtained. In order to verify correctness of performance of numerical analyses, in the scope of model preparation and estimation of boundary conditions, one should perform experimental verification of the construction e.g. by tensometric method at selected points of frame structure.

References

- [1] Marczuk A., Kamiński E., *Effect of spreader loading capacity of manure spreaders on soil compactness*, Problems of Agricultural Engineering, z. 4 (78), 2012, ss.85-93.
- [2] Marczuk A., Kamiński E., *Effect of spreader loading capacity on the values of operational-economic indices of manure application*, Problems of Agricultural Engineering, z. 4 (78), 2012, ss.109-120.
- [3] Hutton D.V., *Fundamentals of Finite Element Analysis*, Tata McGraw-Hill, New York, 2005.
- [4] ANSYS Inc., *ANSYS Mechanical Application User's Guide*, ANSYS 14.5, 2012.

TENSOMETRIC VERIFICATION OF NUMERICAL CALCULATIONS OF FRAME STRUCTURE OF SINGLE AXIS MANURE SPREADER

Artur Cichański, Dariusz Skibicki, Zbigniew Lis, Michał Burak, Michał Stopel

*University of Technology and Life Sciences in Bydgoszcz
ul. Kaliskiego 7, 85-789 Bydgoszcz, Poland
tel.: +48 52 3408235, fax: +48 52 3408245
e-mail: artur.cichanski@utp.edu.pl*

Abstract

The study presents a manner of experimental testing of frame structure of single axis manure spreader. The work aimed at verification of strains determined by FEM in two areas. The first area was the manure box floor, which operated in harshest conditions. The other issue involved verification of correctness of maximum strains determined for the entire structure. Significant issue was to consider of variability of distribution and values of loads. The work suggests reflecting of the variable values through a set of manure box load variants describing stages of the manure spreader loading, unevenness of loading as well as unloading. Obtained by experiment values of stresses have been compared with results of numerical calculations by finite elements method which has proven their high compliance. Maximum stresses have been determined with accuracy of ca. 7%. A load variant affects determined strain values. Strains determined in variants reflecting loading and unevenness of load are characterised by a smaller error than in the case of variants reflecting unloading. This indicates to a greater accuracy of determination of strains with higher values.

Keywords: *agricultural machinery, manure spreader, strain gauge measurements, numerical analyses*

1. Introduction

Numerical analyses of construction resistance conducted with finite elements method allow for determination of stress condition in construction of complex geometrical form. Conditions for performance of such analyses require adaptation of a series of assumptions the most important of which is the continuum and isotropic characteristics of material mechanical properties [8]. Real constructional elements include defects resulting from technological process. The effects as well as inaccuracies of evaluation of boundary conditions and differences between nominal and real geometrical dimensions result in the fact that stresses determined numerically can differ from stresses present in real constructional elements during operation. In order to estimate values of such differences experimental tests of constructions are conducted.

One of the more commonly used methods of measurements of deformation in structural elements include resistance strain gauge measurements [7]. Deformations measured with the use of this method are compared to results of numerical analyses as averaged in a given cross-section [6] or reduced to a point selected on the surface of the considered object [3]. The difference between results of analyses and resistance strain gauge measurements made as part of the work [6] did not exceed 1%. In case of small-sized objects, where it is not possible to use a resistance strain gauge, experimental measurements are made with the use of laser methods [5]. The difference between results of analyses and laser measurements performed as part of the work [6] was approx.

9%. In case of large-sized objects with subassemblies creating various spatial configurations, the verification is done in various measurement points separately for each configuration [4]. In such conditions, each of the configurations can be characterized by a different error. An example of the error for a given measurement point presented in this work [4] and all considered configurations changed from -17.4% to 17.7%. Another method of verification of accuracy of FEM analyses is a verification done on the basis of analytical results [1]. Due to a different character of both modelling methods, an error resulting from comparison of the results may change with the change of boundary conditions.

In this work, we made verification tests of numerical analyses of the structure of a manure spreader bearing frame as described in the work [2]. Numerical analyses of strain of relatively long structures may give reliable results only for a certain range of work of the tested object [1]. Therefore, during experimental verification it is significant to consider variability of distribution and values of loads. The work suggests reflecting of the variable values through a set of manure box load variants describing stages of the manure spreader loading, unevenness of loading as well as unloading. The work aimed at verification of strains determined by FEM in two areas. The first area was the manure box floor, which operated in harshest conditions. The other issue involved verification of correctness of maximum strains determined for the entire structure.

2. The tested object

The tested object was frame construction of single axis manure spreader of carrying capacity of 14t (Fig. 1). Geometrical form of the tested frame structure was described in detail in the study [2]. Main frame beams are made of closed profiles 100x200. Frame is made of steel S235JR. On the one side the spreader is supported on both sides of rear axis. On the other side the spreader is supported at the end of tow bar in joint for single axis trailers. The load is distributed evenly across manure box floor, fixed with lateral ribs. Manure applicators frame is mounted in rear part of the box.

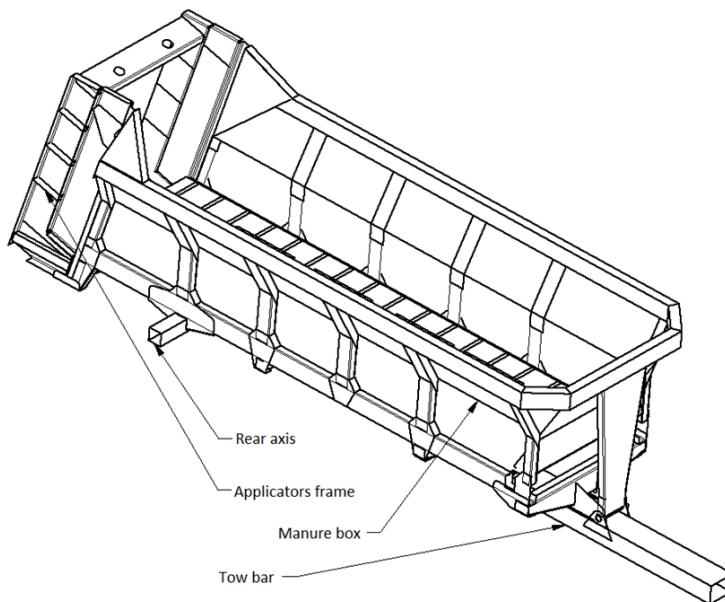


Fig. 1. The tested object.

3. Conditions for research performance

The analysis of the method of operation of the manure spreader indicates that the manure box floor is the part, which operates in harshest conditions. In the course of operation the floor is subject to greatest deformations. Its behaviour as a whole is determined, above all, by rigidity of the system of ribs. The results of numerical analyses [2] served as a reference for determination of most loaded ribs. In places, where extreme strains appeared, they indicated characteristic points on the surface the rib No. 7, 8 and 15. In order to verify the symmetry of load distribution, they indicated an ancillary point found on the surface of the rib No. 7 symmetrically to the axis of the manure spreader. Moreover, FEM analyses constituted a basis for determination of the third transverse beam as a place, where maximum strains for the tested structure can be found. Strain gauge measurements were conducted at these points. The diagram of numbering of strain gauges is presented on Fig. 2.

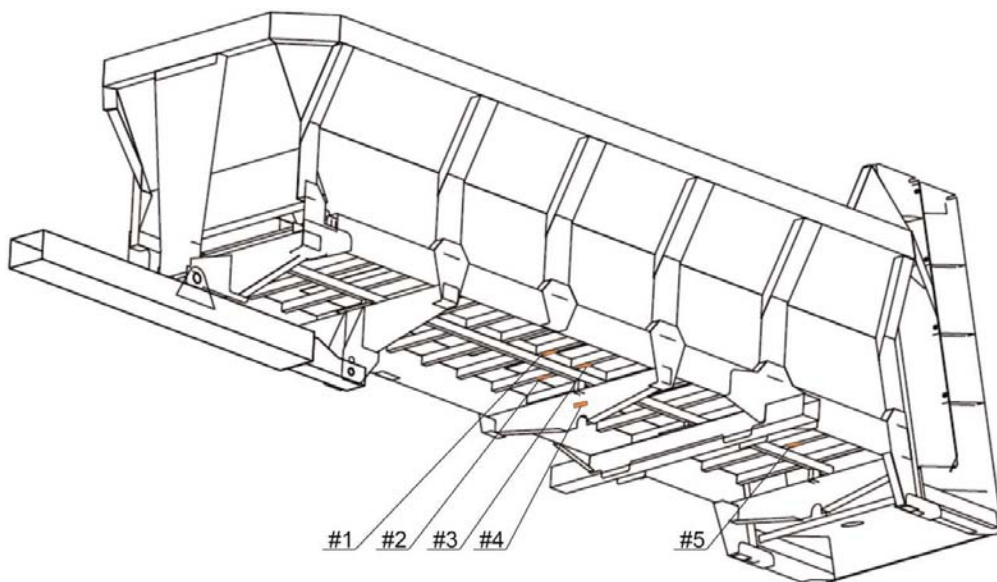


Fig. 2. Diagram of numbering of strain gauges.

Strain gauge No. 4 was located over recess in third transverse beam counting from tow bar side (Fig. 3). Other strain gauges were located in beams reinforcing the floor ribbed structure. Strain gauges No. 1 and No. 2 were located on rib No. 7 symmetrically along the spreader axis (Fig. 3). Strain gauge No. 3 was located on rib No. 8, and strain gauge No. 5 on rib No. 15 (Fig. 3).

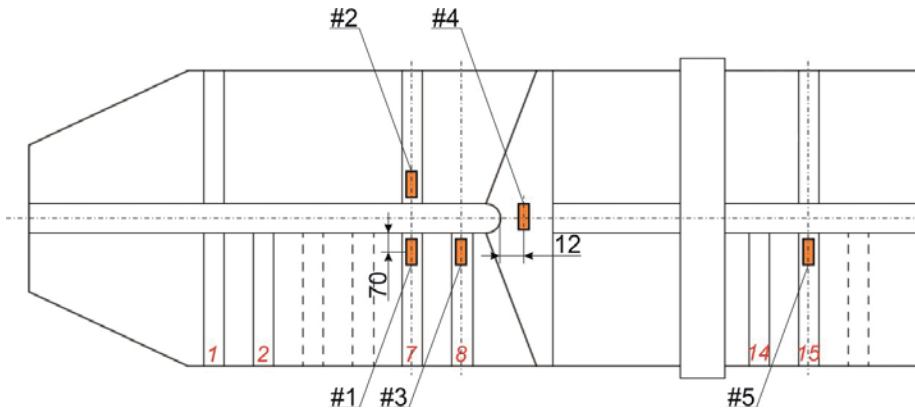


Fig. 3. Diagram of location of strain gauges.

Strain gauge measurements were conducted for the spreader loaded with various sets of forces applied to five areas specified on floor surface. Diagram of identification of the areas is presented on Fig. 4, and their location on Fig. 5. Measurements were conducted on the complete manure spreader. Load was applied at selected areas by locating one – three boxes of mass 540 kg each. Values of loads realized in subsequent variants are presented in table 1. During operation of the manure spreader, variability of loads results from the change of manure distribution along the length of the manure box. In the course of the tests they reflected load increase during the box loading in variant 1 to 4 (table 1). Unevenness of load distribution is reflected in variant 5 to 9. The load decrease during the box unloading is reflected in variant 10 to 14 (table 1).

For reading of values measured with tensometric sensors, 8-channel universal strain gauge bridge made by National Instruments – NI SCXI-1520 and USB module for acquisition of data of 16bits resolution and sampling frequency 200 kS/s – NI SCXI-1600 were used. For data recording NI LabVIEW SignalExpress software was used. During tests strain gauges made by HBM – 1-LY11-6/120-3-3m, of measuring base 6mm and fast drying glue 1-Z70 were used.

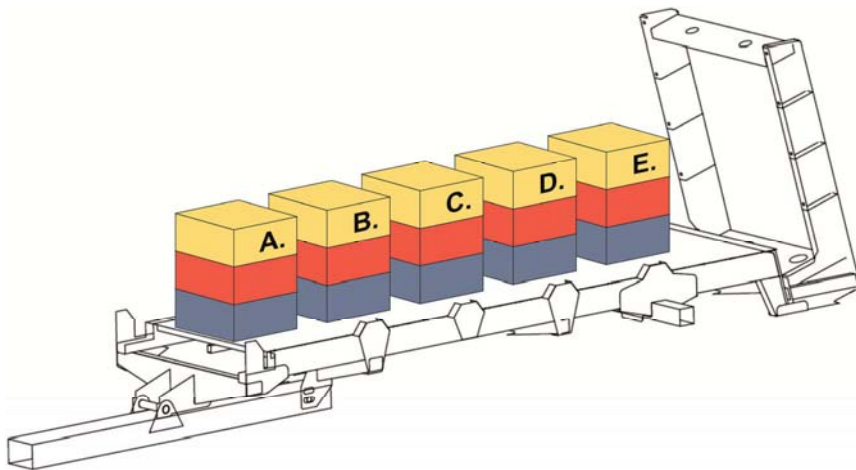


Fig. 4. Diagram of identification of the areas for load application.

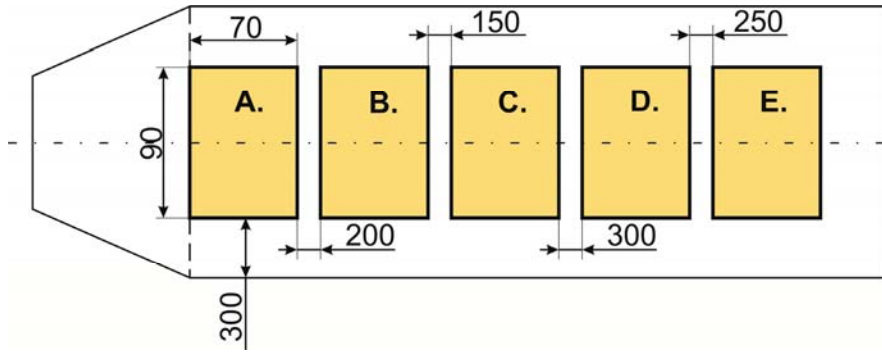


Fig. 5. Diagram of location and size of the areas for load application.

Table. 1. Variants of load realized in subsequent measurements.

Variant	Load in the area [kN]				
	A.	B.	C.	D.	E.
1.	16.2	16.2	10.8	0	0
2.	16.2	16.2	10.8	5.4	0
3.	16.2	16.2	16.2	5.4	0
4.	16.2	16.2	10.8	10.8	0
5.	16.2	10.8	10.8	10.8	5.4
6.	10.8	10.8	10.8	10.8	10.8
7.	5.4	10.8	10.8	16.2	10.8
8.	5.4	10.8	16.2	10.8	10.8
9.	5.4	16.2	10.8	10.8	10.8
10.	5.4	10.8	10.8	10.8	10.8
11.	5.4	10.8	10.8	10.8	5.4
12.	5.4	10.8	10.8	5.4	5.4
13.	5.4	10.8	10.8	5.4	0
14.	5.4	10.8	10.8	0	0



Fig. 6. Manner of loading of the tested frame structure

4. Results of strain gauge measurements

Results of strain gauge measurements measured with strain gauge No. 1 for subsequent variants of load are presented on Fig. 7 with values of stresses read from FEM analyses at the location of strain gauge application. Results of measurements and numerical analyses for strain gauges No. 2 – No. 4 are presented subsequently on Fig. 8 to Fig. 10. Due to location of strain gauge No. 5 at edge area of manure box, for this strain gauge the reading was performed starting from load variant No. 7 from which load in rear part of manure box significantly increased (Table. 1).

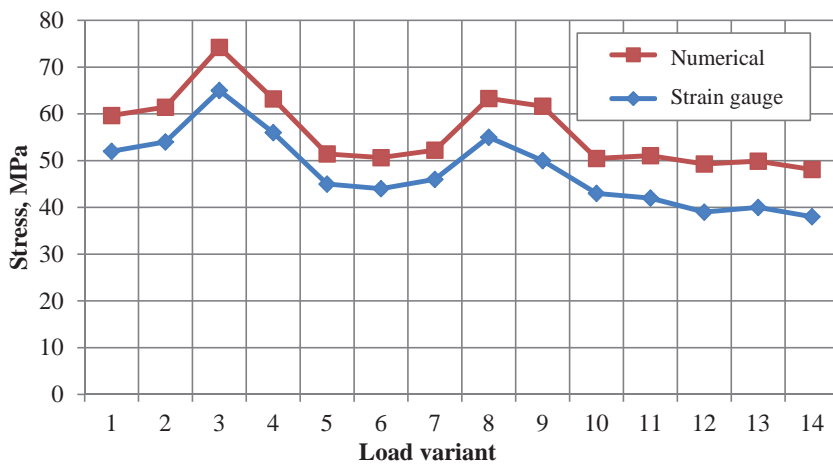


Fig. 7. Results of experimental measurements and numerical calculations for strain gauge #1.

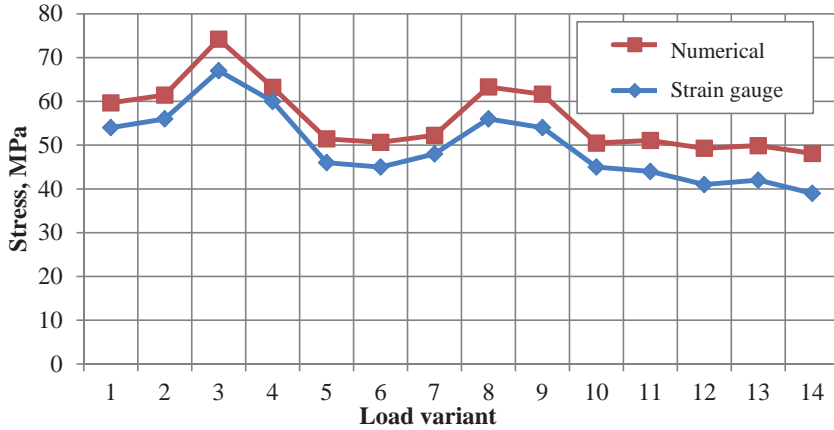


Fig. 8. Results of experimental measurements and numerical calculations for strain gauge #2.

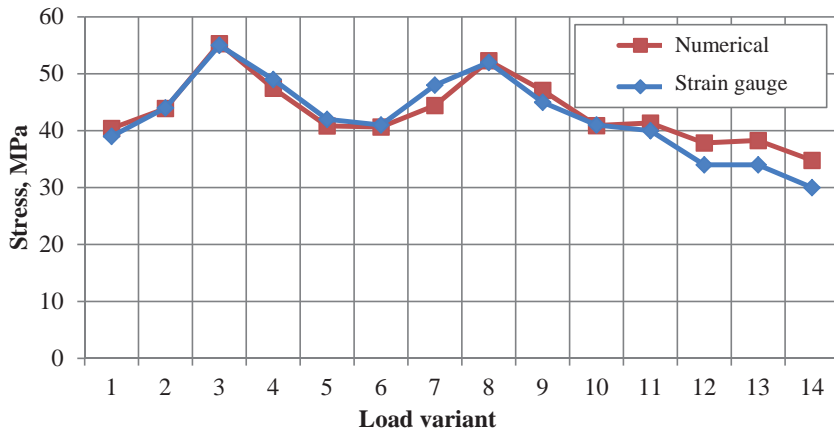


Fig. 9. Results of experimental measurements and numerical calculations for strain gauge #3.

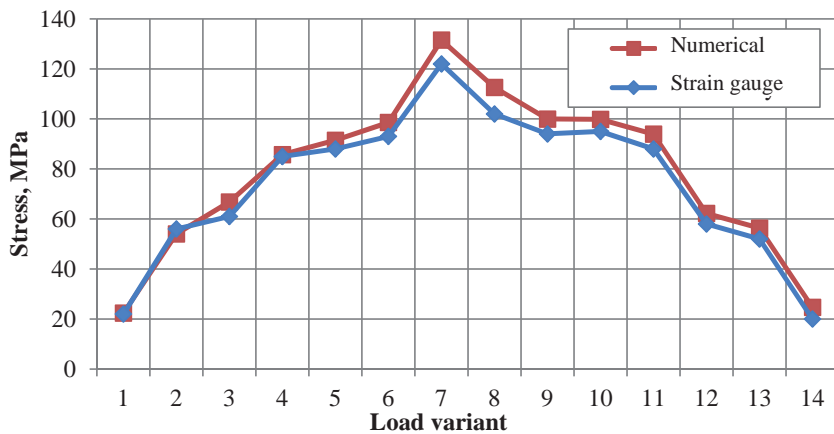


Fig. 10. Results of experimental measurements and numerical calculations for strain gauge #4.

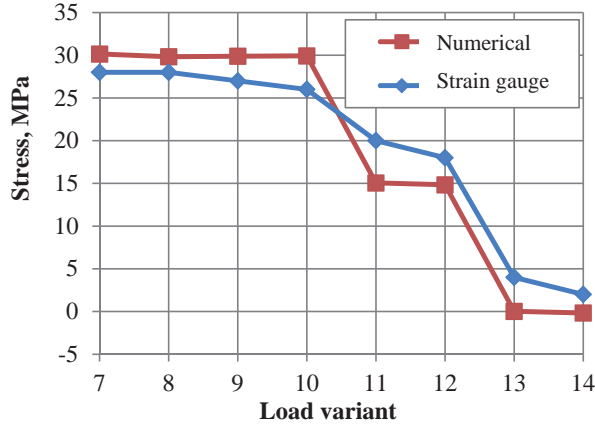


Fig. 11. Results of experimental measurements and numerical calculations for strain gauge #5.

For stresses obtained as a result of strain gauge measurements percentage error was determined from dependencies (1):

$$\delta = \left| \frac{\sigma_{FEM} - \sigma_{meas}}{\sigma_{MES}} \right| * 100\% \quad (1)$$

Values of percentage error for each load variant calculated for individual strain gauges are presented in the form of a plot on Fig. 12. Due to the plot legibility readings of strain gauge No. 5, for which in case of stresses of several MPa significant error values were obtained, were omitted.

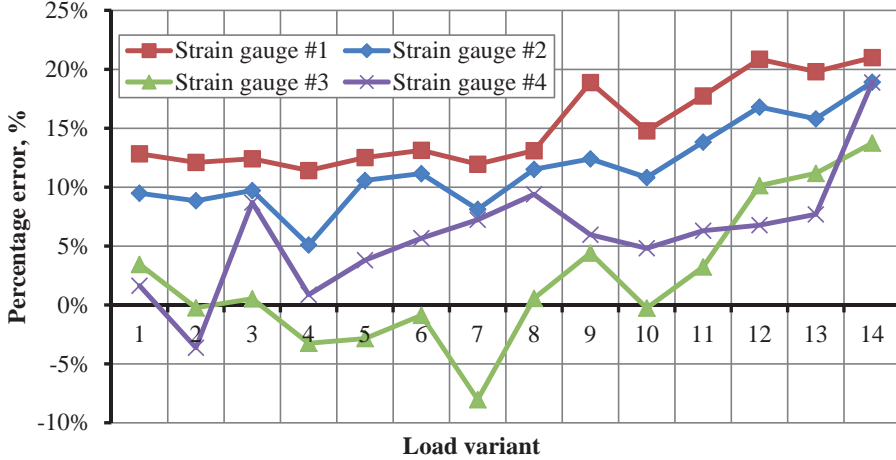


Fig. 12. Strain gauge measurements errors

Comparison of measurement error for strain gauges No. 1 and No. 2 indicates that the stresses determined at selected points located at right side of frame (Fig. 7) reach higher values than analogical stresses at left frame side (Fig. 8). Maximum stress value for the tested frame structure amounting to ca. 130 MPa was determined by strain gauge No. 4 for 7 variant of load with error not exceeding 10%. Maximum error for the whole analysis reached the value of ca. 20%. For strain gauges No. 1 to No. 3 starting from 8 load variant relative error increases as the stress value decreases.

5. Summary

The study presents the conditions for performance of strain gauge measurements of frame structure of manure spreader and values of stresses determined at selected frame structure points. Experimental measurement results were compared with FEM numerical calculation results. Good compliance between values of stresses specified by both methods was achieved which confirmed correctness of performance of numerical analyses. In the vast scope of comparison of results of calculations and measurements overestimation of values of stresses specified numerically was noted which locates measurement results on safe side. Increase of values of determined stresses was accompanied by increase of accuracy of calculations.

A load variant affects determined strain values. Strains determined in variants reflecting loading and unevenness of load are characterized by a smaller error than in the case of variants reflecting unloading. This indicates to a greater accuracy of determination of strains with higher values.

In the course of measurements they also found that strains in the manure box floor ribs and maximum strains for the structure had been determined correctly. They also found a slight asymmetry of distribution in the course of the manure box load during tests.

References

- [1] Chłus K., Krasoń W., Analiza wytrzymałości mostu składanego z uwzględnieniem luzów montażowych, Modelowanie Inżynierskie, 41, Gliwice, 2011, s.19-26
- [2] Cichański A., Burak M., Stopel M., *Numerical analysis of frame structure of single axis manure spreader*, Journal of Polish CIMAC, Gdańsk, 2013.
- [3] Dobrot O-M, Tocu F., Mocanu C.I, Numerical and experimental method to align 2500 TF press columns, Journal of Engineering Studies and Research, 18, 2012, s. 29-34
- [4] Kosmol J., Wilk P. Doświadczalna weryfikacja numerycznego modelu pionowego centrum obróbkowego. Modelowanie Inżynierskie, 41, Gliwice, 2011, s. 187-195.
- [5] Pilch Z., Trawiński T., Pomiarowa weryfikacja odkształceń ramienia aktuatora dysku HDD określonych metodą analityczną i MES, Modelowanie Inżynierskie, 42, Gliwice, 2011, s.342-350
- [6] Ryś J., Malara P., Barski N., Analiza numeryczna wpływu sztywności uszczelki na obciążenie śrub w połączeniu kołnierзовym, Mechanika. Czasopismo Techniczne, Wydawnictwo Politechniki Krakowskiej, Zeszyt 5, Rok 108, Kraków, 2011, s.93-112.
- [7] Roliński Z., *Tensometria oporowa: podstawy teoretyczne i przykłady zastosowań*, Warszawa, WNT, 1981
- [8] Ugural A.C., *Mechanics of materials*, John Wiley&Sons, 2008.

EXPOSURE OF PRINTED CIRCUITS BY SUB-PIXEL SCROLL METHOD

Piotr Domanowski, Ryszard Wocianiec

*University of Technology and Life Sciences in Bydgoszcz
al. Prof. S. Kaliskiego 7, 85-789 Bydgoszcz, Poland
e-mail: piotr.domanowski@utp.edu.pl*

Abstract

The article shows principle of operation of the direct transfer of the image, and the idea of sub-pixel image scroll used in digital platesetter. It consists of a UV radiation source, the micro mirror image forming, system of the projection of an image onto the photopolymer and placed in the optical path mirror deflecting UV rays at an angle of 45°, and associated with the piezoelectric actuator. Such shaped optical system allows the usage of sub-pixel scrolling image projected on the photopolymer. The second mirror with the actuator deflecting the image in a direction perpendicular to the primary scanning direction placed in the optical path allows to increase the accuracy of the transfer of the image.

Keywords: *photolithography, exposure, DMD*

1. Introduction

In the production of microelectronic devices are used photolithography methods of direct transfer of the image on the panel covered a photopolymer without printing plates. "Digital matrixes of mirrors" (DMD), e.g. Texas Instruments can be used for direct transfer of the image. DMD consists of a system of mini-mirrors covering 415 872 individual mirror elements (DLP3000) [1], each of which can be set in two positions (Fig. 1). The slope of the mirror elements of the mini-mirror system produced a surface consisting of the deflected and undeflected mirror element, whose image is projected by the optics projection on the photosensitive surface. Further, successive images are generated by using a computer and then transferred to the surface. At reproduction ratio of 1:1, the substrate surface about the size of 6571.8 x 3699 microns (DLP3000) [1] is exposed to light.

Most recent application of DMD for direct image transfer are using mainly two methods of irradiation of larger areas of the substrate:

1. Static method (step-and-repeat) [2, 3],
2. By scrolling (scrolling method) [2, 4].

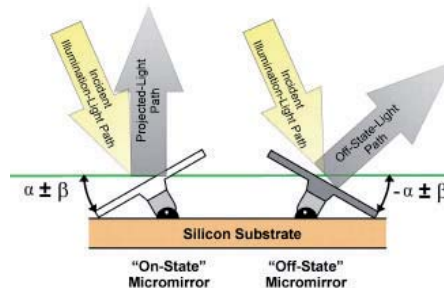


Fig. 1 The principle of operation of the system DMD (Digital Mirror Devices) Texas Instruments Inc. [1]

A continuous scrolling method (2) can be described as exposure the substrate surface element (pixel) by the mirror element. Mirror element and the substrate surface element are moving relative to each other with carefully controlled rate. In order to obtain an image of the same dimensions as the DMD mirror matrix, the relative movement takes place at a distance equivalent to the length of the matrix of mirrors. When matrix is moving to a new location, transferring the next image to the DMD takes place.

Both methods have some disadvantages. In the method of step-and-repeat you need to make thousands of precise positioning, leading to the complex mechanics and long periods of dead time. The scrolling method accomplishes the uniform feed motion at the cost of "smeared" edge transition and with a scan velocity limited by the mirror switching frequency, for example with a imaging ratio of 1:1 is approximately 135 mm / sec. The mentioned scrolling methods require a precisely controlled speed, thus inexpensive toothed belt drives are not usable.

2. Construction of a system for direct transfer of the image by sub-pixel scrolling method

"Sub-pixel method" (Sub-pixel Scroll Method), uses an additional element in the form of a mirror inclined at an angle of 45° , which is placed between the matrix and the DMD projection optics [2] for the optical shift position mirror elements relative to the axis of each projection the size of a single sub-pixel. In a preferred embodiment, the 45° mirror is shifted by $1/4$ the width of a mirror element by a controllable actuator. The size of this change of position and the time point are synchronized by the position indicator signals of the scan sled in such a way that the mirror element (as with the standard scrolling method) seems to stand relative to the substrate surface element. Differently than with the standard scrolling method is the resetting, which however is not bound to the DMD switching speed of 10 kHz. Due to its higher resolution, the present invention reduces the blur at the edge transition and makes a higher scan velocity possible, whereby the scan velocity depends on the dynamics of the actuator, the effective UV-power of the UV source and

the sensitivity of the photosensitive polymer. A further advantageous function of the present invention is the possibility of transferring a pattern with higher resolution than given by the mirror element size. For an increase of the resolution in X (scan direction) and Y perpendicular to the scan direction) two mirror actuators are necessary, which work in X and Y.

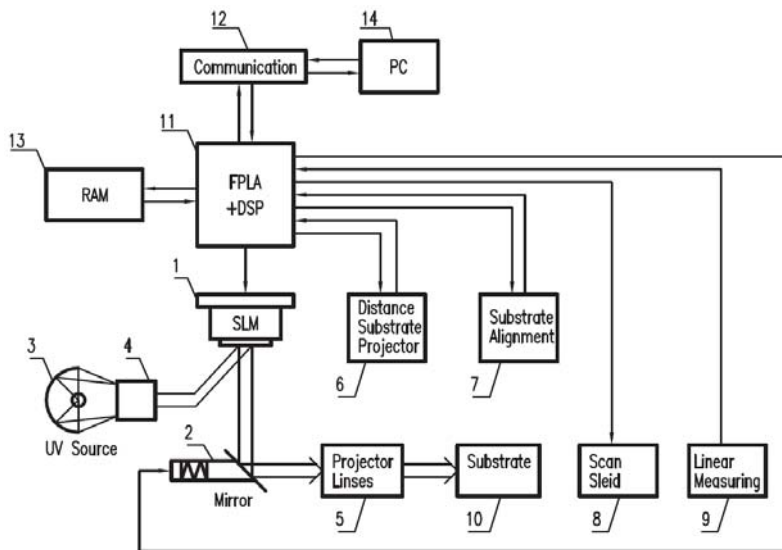


Fig.2 System for direct transfer of the image by sub-pixel scrolling method
(a description is in the contents of Chapter 2)

Designed lithographic system shown in Figure 2 contains a source of ultraviolet radiation - 3, condenser optics - 4, a spatial light modulator (SLM) - 1 (in this project modulator is equipped with a digital array of mirrors (DMD), such as the Discovery 1100 from Texas Instruments), the projection lens system - 5 and mirror's controllable actuator sloping at an angle of $45^\circ - 2$.

The beams reflected by the mirror matrix 1 are optically shifted along the projection axis 2 controlled mirror actuator. Additionally, Fig. 1 shows the control system of digital signal processor (DSP) and free programmable logic array (FPLA) 11, that controls all functions of the lithographic system. In a computer system (PC) 14 the layout data of a pixel pattern are prepared.

For a preferred substrate format 600x500 mm and a preferred resolution of 12.7: per pixel, the size of the prepared data set is about 275 megabyte. This amount of data is transferred via a fast communication means 12 to the RAM 13. The exact distance of the projector optics 5 to the substrate 10 is measured and adjusted constantly by the distance substrate projector feature 6 of the DSP/FPLA 11. Before beginning the exposure, each new substrate 10 is measured: exactly and aligned to the scan direction of the scan sled 8 by the substrate alignment feature 7 of the DSP/FPLA 11. The linear measuring system 9 supplies the trigger signals for the exact synchronization of all switching processes of the SLM 1, and the optical displacement of the reflected UV beams by the mirror actuator 2. The synchronization of all switching processes with only the position indicator signals makes the-exact lithographic transfer of the patterns independent of the speed of the projection optics relative to the substrate. At low speed about the

point of reversal of the scan direction, the UV energy is controlled by variation of the on-off relationship of the mirror elements 1.

3. The direct transfer of the image

Referring to the drawings, the preferred details of the present invention are graphically and schematically shown. Like elements in the drawings are indicated by numbers, and any similar elements are indicated by the corresponding numbers with the addition of letters.

Figures 3a-3f show the process of the present sub-pixel scroll method with the exposure of a substrate surface element by three mirror elements. In this example, each step of correction by the 45° mirror actuator amounts to 0.5 pixels. In the embodiment illustrated in the figures, the 45° mirror actuator has a total correction potential of 2 pixels, i.e., after four steps of correction of 0.5 pixels each, the 45° mirror actuator must be pulled back to the zero value (reset). However, any number of correction steps may be practiced in the present invention under appropriate process control and scale of the actuator mirror 2. The sub-pixel scroll method is described with the drawings. 3a-3f [3, 4].

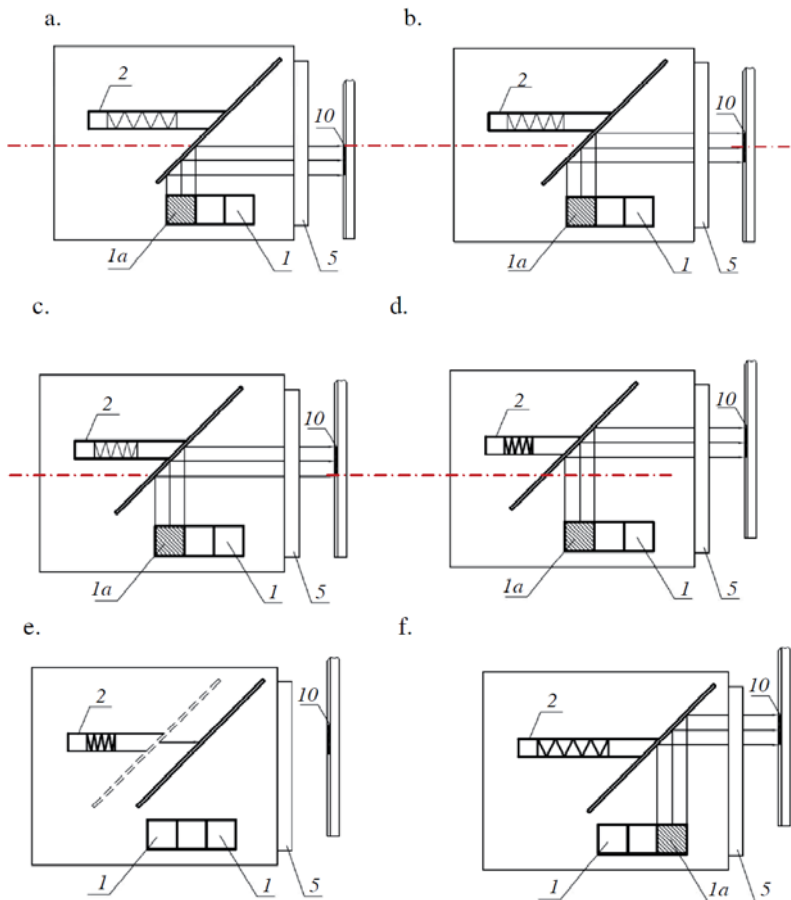


Fig. 3 The next phases exposure by sub-pixel scrolling method

The Sub-pixel Scroll method exposes a substrate surface element of the substrate 10 while exposure optics and substrate move relative to each other. The blur of the substrate surface element edge depends on the number of correction steps per substrate surface element, can thus amount to 1/10 the width of the substrate surface element. The speed of the exposure system is not limited to switching frequency \times substrate surface element width, as with known scrolling methods. The maximum scan velocity and thus the exposure time for the entire substrate depends on the correction potential of the mirror actuator, the switching time for loading of a new pattern in the DMD, the resist sensitivity and the effective UV power on the substrate.

Figs. 4a-4d show the method for the improvement of the resolution, a more advantageous function of the Sub-pixel scroll method, the increase of the resolution of the pixel pattern by using of a mirror actuator with deflection possibility in X/Y. The Sub-pixel Scroll method is advantageous because it increases the resolution of the pixel pattern by usage of a mirror actuator with deflection possibility in X/Y. A substrate surface 301 is to be exposed, which is larger than two substrate surface elements and has edges, which lie in the raster 0.5 \times width of the substrate surface element. For known maskless lithographic procedures the resolution is fixed by the size of the mirror elements, the smallest raster thus is 1 \times width of the substrate surface element.

- Fig. 4a shows a substrate surface 1 and a mirror element 2, which exposes substrate surface element 3 with the deflection mirror in zero position and substrate surface element 4 with a deflection mirror deflected in X/Y.
- In Fig. 4b, a program for processing of pixels generates a mirror pattern that exposes the surface substrate 1 as far as possible with substrate surface elements 3.
- In Fig. 4c, for the non-exposed partial surface of the substrate surface, then a mirror pattern is generated by the program, which exposes these surfaces as far as possible with substrate surface elements 304. In the corners partial surface squares with an edge length of 0.5 \times width of a substrate surface element can remain unexposed.
- Fig. 4d shows the distribution of the exposure energy in the substrate surface after the exposure illustrated in Figs. 4b and 4c.

In order to avoid unnecessary scanning paths, the process steps shown in Figs 4b and 4c should be mutually changed after the cycle of Figure 3 during exposure of the substrate surface.

Conclusions

- The higher resolution of this method is accomplished by doubling of the exposure time. By introduction of further partitioning steps and exposure passages the resolution potentially can be increased at will.
- The described method reduces the blur at the edge transition and makes a higher scan velocity possible, whereby the scan velocity depends on the dynamics of the actuator, the effective UV-power of the UV source and the sensitivity of the photosensitive polymer.

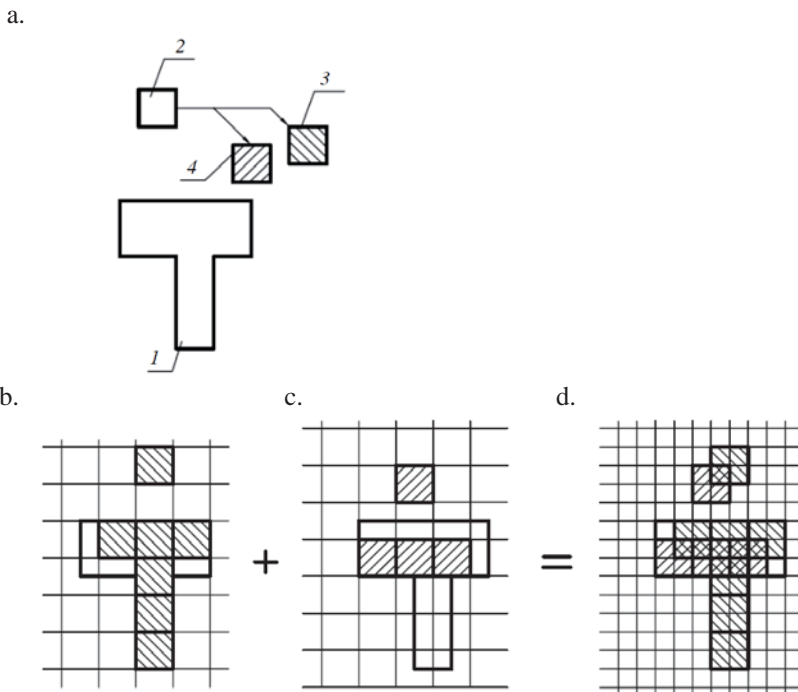


Fig. 4 Function of increase in resolution by the method of sub-pixel scrolling

- Sub-pixel scrolling method allows the transfer of a pattern with a higher resolution than that which is determined by the size of the matrix element DMD mirror.
- Multiple variations and modifications are possible in the embodiments of the invention described here. Although certain illustrative embodiments of the invention have been shown and described here, a wide range of modifications, changes, and substitutions is contemplated in the foregoing disclosure. In some instances, some features of the present invention may be employed without a corresponding use of the other features. Accordingly, it is appropriate that the foregoing description be construed broadly and understood as being given by way of illustration and example only, the spirit and scope of the invention being limited only by the appended claims.

References

- [1] *DLP3000 Technical Documents*, <http://www.ti.com/product/DLP3000>, 24 Oct 2012
- [2] Domanowski P., Wocianiec R.: *Wpływ jakości montażu układu optycznego cyfrowej naświetlarki obwodów drukowanych na dokładność odwzorowania obrazu*, Projektowanie Mechatroniczne – Zagadnienia wybrane, praca zbiorowa pod redakcją Tadeusza Uhla, Kraków, 2011
- [3] Skibicki D., Paczkowski T., Domanowski P.: *Lithographic method for mask less pattern transfer onto a photosensitive substrate*, United States Patent, US 7,982,853, B2, 2011
- [4] Domanowski P., Wocianiec R.: *Konstrukcja cyfrowej naświetlarki obwodów drukowanych*, Projektowanie Mechatroniczne – Zagadnienia wybrane, praca zbiorowa pod redakcją Tadeusza Uhla, Kraków, 2013

AFFECT OF CEMENTITE PRECIPITATION ON THE EXTEND OF BAINITE REACTION IN ADI

Zdzisław Ławrynowicz

*University of Technology and Life Sciences, Mechanical Engineering Faculty
Department of Materials Science and Engineering, av. Kaliskiego 7
85-789 Bydgoszcz, Poland, e-mail: lawry@utp.edu.pl*

Abstract

Presented paper demonstrates how the precipitation of cementite from ferrite or/and austenite in ADI may influence the extend of bainite reaction. Analytical calculations and experimental measurements of volume fraction of bainitic ferrite and volume of the untransformed austenite indicate that there is a necessity of carbides precipitation. A consequence of the precipitation of cementite from austenite during austempering is that the growth of bainitic ferrite can continue to larger extent and that the resulting microstructure is not an ausferrite but it is a mixture of bainitic ferrite, retained austenite and carbides. In case of this microstructure, the product of austempering reaction in ductile iron is rather bainite than "ausferrite". The results are discussed in the context of displacive mechanism of bainite transformation.

Keywords: carbon diffusion, bainite transformation, cementite precipitation

1. Introduction

The development of austempered ductile iron (ADI) is a major achievement in cast iron technology. The starting material for the production of ADI is the high quality ductile or nodular cast iron. In 1948 the invention of ductile iron was announced jointly by the British Cast Iron Research Association (BCIRA) and the International Nickel Company (INCO). By the 1950's, both the material, ductile iron, and the austempering process had been developed. By the 1990's, ASTM A897-90 and ASTM A897M-90 Specifications for Austempered Ductile Iron Castings were published in the US that consist the five Grades of ADI according to ASTM A897/897M.

The attractive properties of bainitic irons without carbides are related to its unique microstructure that consists of ferrite and high carbon austenite. Because of this microstructure, the product of bainitic reaction is often referred to as "ausferrite" rather than bainite [1-4]. The mixture of bainitic ferrite and untransformed austenite is an ideal combination from many points of view. Once the ausferrite has been produced, the components are cooled to room temperature. The cooling rate will not affect the final microstructure as the carbon content of the austenite is high enough to lower the martensite start temperature to a temperature significantly below room temperature. If the bainitic ferrite-austenite microstructure is held for long time periods, the blocks of high carbon austenite will eventually undergo a transformation to bainite, the two phase ferrite and carbide ($\alpha + \text{Fe}_3\text{C}$).

The purpose of the present paper is to demonstrate how the precipitation of cementite from ferrite or/and austenite in ADI may influence the extent of bainite reaction.

2. Material and methods

The chemical composition of the experimental ductile iron is listed in Table 1. The concentration of alloying elements in the matrix is obtained from the chemical analysis. Ductile iron blocks were produced in a commercial foundry furnace. The melt was poured into a standard Y block sands molds (ASTM A-395), which ensured sound castings. Specimens austenitised at $T_{\gamma}=950^{\circ}\text{C}$ for 60 minutes were rapidly transferred to a salt bath at austempering temperatures 250, 300, 350 and 400°C , held for 15, 30, 60, 120 and 240 minutes and then water quenched to room temperature. The microstructure of the as-cast material matrix contains 40% ferrite and 60% pearlite, however graphite nodules in material is 11.5%.

Tab. 1. Chemical composition of ductile cast iron ADI, wt-%

C	Si	Mn	P	S	Mg	Cr	Ni	Mo
3.21	2.57	0.28	0.06	0.01	0.024	0.036	0.098	0.015

The X-ray investigations were performed on the specimens heat treated after specific time of the isothermal bainite reaction at the given temperature. The total volume fraction of the retained austenite was measured from the integral intensity of the $(111)\gamma$ and $(011)\alpha$ peaks. The presence of high silicon content in ADI retards the formation of cementite in ferrite and austenite. Then, the measurements of carbon concentration in retained austenite were carried out by using X-ray diffraction. The carbon concentration was calculated from measured lattice parameter of the retained austenite. The 2θ values for austenite peaks were used to calculate the d spacing with Bragg's law and then the lattice parameters. The lattice parameter of austenite (a_{γ}) is related to the known relationship between the parameter and the carbon concentration [2,3]:

$$a_{\gamma}(\text{nm})=0.3573 + 0.0033 x_{\gamma} \quad (1)$$

where x_{γ} is the carbon concentration in austenite, in weight %.

The matrix carbon concentration, x_{γ}^m , of the ductile iron was also determined experimentally with Dron 1.5 diffractometer using $\text{CoK}\alpha$ radiation on specimens austenitised at 950°C for 60 minutes and quenched to ambient temperature. It was found that after quenching from austenitising temperature 950°C the calculated carbon content in matrix is $x_{\gamma}^m=1.044\% \text{C}$ and measured carbon content is $x_{\gamma}^m=1.05\% \text{C}$ thus, the measured value was taken for further calculation.

3. Results and discussion

When the matrix of ADI only consist of ausferrite, thus:

$$V_{\gamma} + V_{\alpha} = 1 \quad (2)$$

and the permitted fraction of bainite (V_α) can be determined from Lever rule applied to the T_0 ¹ curve, Fig. 1.

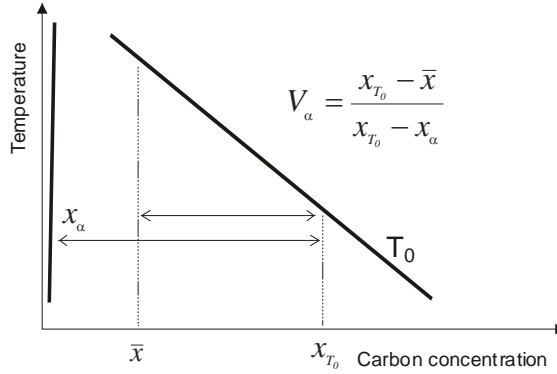


Fig. 1. Application of the Lever-rule to the T_0 curve allows the estimation of the permitted fraction of bainite (V_α) at any temperature (where for 950°C $\bar{x} = 1.05$ wt.% C $x_\alpha = 0.03$ wt.% C)

The maximum volume fraction of retained austenite (V_γ) will then equal $1 - V_\alpha$. In case of carbides precipitation the maximum volume fraction of bainitic ferrite (V_α) can be calculated using the following equation [4]:

$$V_\alpha = \frac{x_{T_0} - \bar{x}}{x_{T_0} - x_\alpha - x_C} \quad (3)$$

where V_α is volume fraction of bainitic ferrite, \bar{x} is the average carbon concentration in the matrix of the alloy, x_α is the paraequilibrium carbon concentration in the bainitic ferrite (0.03 wt. %), x_{T_0} is the carbon concentration of the austenite corresponding to the T_0 curve, x_C is the amount of carbon, which is tied up as carbides (cementite). Thus, the maximum volume fraction of bainite taking into account cementite precipitation can be calculated using the relationship (3).

It is seen in Fig. 2 that precipitation of cementite leads to an increase of volume fraction of bainitic ferrite. Carbides locally reduce the carbon content of the parent austenite and increase the driving force for further ferrite growth.

The measured volume fraction of retained austenite, bainitic ferrite and carbon concentrations in residual austenite are shown in Tab. 2. Comparison of the calculated (Fig. 2) and measured (Tab. 2) fraction of bainite indicate that during bainite transformation in ADI must be intensive cementite precipitation.

Cementite can precipitate from supersaturated bainitic ferrite and also from austenite. The growth of bainite is probably diffusionless but any excess carbon in the supersaturated ferrite soon

¹ The T_0 temperature can be defined [5-8] such that stress free austenite and ferrite of the same composition (with respect to both the interstitial and the substitutional alloying elements) are in metastable equilibrium. Thus any displacive transformation involving a full supersaturation of carbon (i.e. bainitic ferrite would then inherit the carbon content of the parent austenite) can occur only below the appropriate T_0 temperature. Strain energy would have effect of shifting curve to lower carbon concentration, T_0' curve [9]. The T_0' line accounts for 400 J/mol of stored energy in the bainite. If this energy is reduced by plastic deformation of the surrounding austenite then a higher volume fraction of bainite should be able to form.

afterwards partitions into the residual austenite or precipitates within bainitic ferrite in the form of carbides [7-10]. When the process of carbon partitioning into the residual austenite is rapid relative to that of carbide precipitation, the transformation product is called “upper bainite”, whereas “lower bainite” is obtained when some of the carbon supersaturation is relieved by precipitation within the bainitic ferrite [8,9,11].

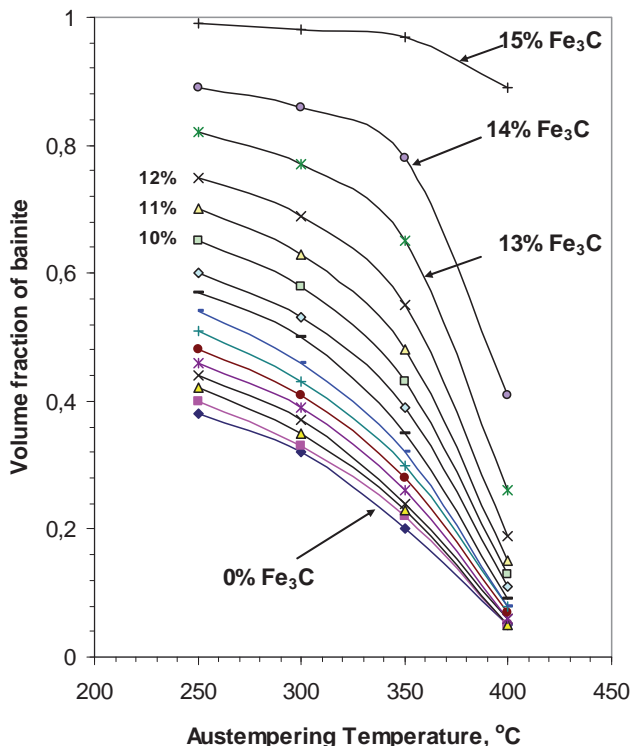


Fig. 2. Calculated the maximum volume fraction of bainite in investigated ADI taking into account cementite precipitation in the range from 0% to 15 wt. % Fe_3C

Austenite is supersaturated with respect to cementite precipitation when $x_\gamma > x^{\gamma\theta}$, where $x^{\gamma\theta}$ denotes carbon concentration at the extrapolated A_{cm} boundary. This means for the bainite reaction, that $x_{T_0} > x^{\gamma\theta}$ since the growth of bainitic ferrite stops when x_γ reaches the value x_{T_0} given by the T_0 curve of the phase diagram. A consequence of the precipitation of cementite from austenite is that its carbon concentration drops below x_{T_0} , so that the growth of bainitic ferrite can continue to an extent larger than would be otherwise possible (see Fig. 2).

The large discrepancies among calculated and measured volume fractions of bainite can be explained by intensive cementite precipitation during bainitic reaction. The thermodynamic restriction imposed by the T_0 curve on the extent of bainite transformation can result in the formation of pools of retained austenite with a coarse, blocky morphology, Fig. 3.

Tab. 2. The measured volume fraction of retained austenite, bainitic ferrite and carbon concentrations in residual austenite

Austempering conditions		Austenitisation temperature, 950°C			
°C	Time, min.	Measured volume fractions of, %		Carbon concentrations of the residual austenite x_γ , wt. %	
		retained austenite V_γ	bainitic ferrite, V_α	x_γ , calculated	x_γ , measured
400	15	43.6	56.4	2.37	1.42
	30	38.3	61.7	2.69	1.50
	60	45.1	54.9	2.29	1.54
	120	44.7	55.3	2.32	1.54
	240	31.3	68.7	3.29	1.54
350	15	40.3	59.7	2.56	1.50
	30	38.1	61.9	2.71	1.50
	60	35.5	64.5	2.90	1.62
	120	36.3	63.7	2.84	1.58
	240	29.8	70.2	3.45	1.38
300	15	38.3	61.7	2.69	1.25
	30	32.2	67.8	3.19	1.54
	60	31.8	68.2	3.24	1.50
	120	25.1	74.9	4.09	1.62
	240	18.3	81.7	5.60	1.62
250	15	29.8	70.2	3.45	0.88
	30	29.8	70.2	3.45	1.02
	60	30.1	69.9	3.42	1.01
	120	24.2	75.8	4.25	1.25
	240	16.4	83.6	6.25	1.22

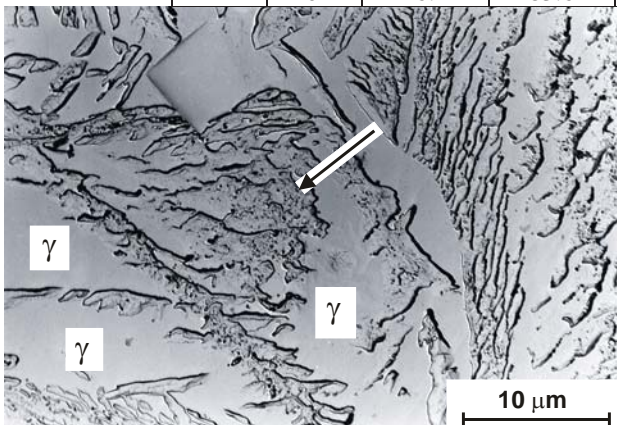


Fig. 3. Carbon replica taken from sample austenitised at 950 °C and austempered at 400 °C for 120 min. This replica reveals the presence of carbides inside of bainite (arrowed) and shows large pools of blocky retained austenite

Because of the inhomogeneous distribution of carbon and other solutes in the matrix after transformation to bainite the retained austenite is enriched to a greater extent in the immediate vicinity to bainite platelets or in the region trapped between the platelets and in the eutectic cell boundary (Fig. 3) while other region contains relatively poor carbon [12]. The above effect can be exaggerated in ADI, since cast iron is usually extremely segregated. Martensite is usually found to be in the cell boundary which solidified last [13]. It indicates that the austenite in cell boundary is less enriched with carbon, and therefore is thermally unstable.

4. Conclusions

The following conclusions were reached:

1. Analytical calculations and experimental measurements of volume fraction of bainitic ferrite and volume of the untransformed austenite indicate that there is a necessity of carbides precipitation.
2. A consequence of the precipitation of cementite from ferrite or/and austenite during austempering is that the growth of bainitic ferrite can continue to larger extent and that the resulting microstructure is not an ausferrite but is a mixture of bainitic ferrite, retained austenite and carbides.

References

- [1] Chang, L.C., *Carbon content of austenite in austempered ductile iron*, Scripta Materialia, vol.39, No 1, pp. 35-38, 1998.
- [2] Pietrowski, S., *Nodular cast iron of bainitic ferrite structure with austenite or bainitic structure*, Archives of Materials Science, vol. 18, No.4, pp.253-273, 1997. (in Polish)
- [3] Guzik, S.E., *Austempered cast iron as a modern constructional material*, Inżynieria Materiałowa, nr 6, pp.677-680, 2003. (in Polish)
- [4] Takahashi, M., Bhadeshia, H.K.D.H., *A Model for the Microstructure of Some Advanced Bainitic Steels*, Materials Transaction, JIM, 32, pp. 689-696, 1991.
- [5] Ławrynowicz, Z., *Transition from upper to lower bainite in Fe-Cr-C steel*, Materials Science and Technology, 20, pp.1447-1454, 2004.
- [6] Ławrynowicz, Z., *A discussion on the mechanism of bainite transformation in steels*, Technology and Materials, Gdańsk, Politechnika Gdańska, 4, pp.149-155, 2006, (in Polish)
- [7] Ławrynowicz, Z., *Mechanism of bainite transformation in Fe-Cr-Mo-V-Ti-C steel*, International Journal of Engineering, 12, pp.81-86, 1999.
- [8] Christian, J.W., *Theory of transformations in metals and alloys*, 778, Oxford, Pergamon Press, 1965.
- [9] Bhadeshia, H.K.D.H., *Bainite in Steels*, Institute of Materials, 1-458, London, 1992.
- [10] Shiflet, G.J., Hackenberg, R.E., *Partitioning and the growth of bainite*, Scripta Materialia, 47, pp.163-167, 2002.
- [11] Bhadeshia, H.K.D.H., *Diffusion of carbon in austenite*, Metal Science, 15, 477-479, 1981.
- [12] Kutsov, A. at al., *Formation of bainite in ductile iron*, Materials Sci. and Engineering, A273-275, pp.480-484, 1999.
- [13] Bhadeshia, H.K.D.H., Christian, J.W., *Bainite in Steels*, Metallurgical Transactions A, 21A, pp.767-797, 1990.



CUTTING FORCES IN DRY AND NEAR DRY CUTTING OFF MACHINING

Tadeusz Leppert

*University of Technology and Life Sciences
ul. Kordeckiego 20, 85-225 Bydgoszcz, Poland
e-mail: tleppert@utp.edu.pl*

Abstract

The article presents research results on the effect of cooling and lubrication on the cutting force in cutting off process of A11and C45 steel rods using different rake face shapes and cutting parameters. The aim of the investigation was to determine outcomes of elimination (dry cutting) or reduction (minimum quantity lubrication – MQL) of a cooling and lubricating fluid in the cutting off process. It has been concluded that the minimum quantity lubrication allowed decreasing the cutting force compared to dry cutting. The impact of eliminating or reducing the quantity of the cooling and lubricating medium on the cutting force in the cutting off process of both types of steel depend on the applied feed rate and cutting speed. Taking into account environmental reasons, the dry and MQL cutting off is advisable and highly justifiable.

Keywords: cutting off, dry cutting, MQL, cutting force

1. Introduction

Lubricating and cooling liquids in cutting processes have a considerable impact on durability of cutting tools, dimensional accuracy and quality of machined surfaces. They also influence chip formation and all the phenomena in the cutting zone. As research has shown [1,7,9], machining without any cutting liquid (dry cutting) or with a minimal quantity of cooling and lubrication liquid is becoming more and more widespread in industrial environments. This can be attributed to more stringent environmental regulations, advancement in developing new tool materials and coatings, which increase tool durability as well as new solutions in machining equipment [2,5,6]. Eliminating cutting liquids from machining processes or their considerable reduction requires further investigation into the cutting process as well as determining optimal cutting conditions for different types of machined materials, which will lead to high quality surfaces obtained at reduced production costs [3,7,9].

The cutting forces are important features of the cutting process. One needs to know them to be able to determine the required power of a machine tool, tool life and ensure static and dynamic stability of the machining system. Their values depend on existing cutting conditions, including the cooling and lubrication mode of the cutting zone. Because of their importance for the cutting process,

they should be taken into account while considering eliminating or reducing the application of cutting liquids [2,8].

The conducted research was aimed at determining cutting forces in cutting off machining of automatic A11 and construction C45 steel in dry and with minimum lubrication conditions in a wide range of cutting parameters.

2. Experimental procedure

The research was conducted on a TUD 50 lathe, equipped with an air-oil aerosol generator Accu-Lube MiniBOOSTER MBII. The steel samples were \varnothing 30 mm rods made of both types of steel, whose composition and mechanical properties are presented in table 1 (according to PN-73/H-84026 and PN-93/H-84019).

Table 1. Chemical composition and properties of A11 and 45 steels

Steel grade	Chemical composition, %							
	C	Si	Mn	P	S	Cr	Mo	Ni
A11	0,07-0,13	0,15-0,40	0,50-0,90	$\leq 0,06$	0,15-0,25			
45	0,42-0,50	0,17-0,37	0,5-0,8	$\leq 0,04$	$\leq 0,04$	$\leq 0,30$	$\leq 0,10$	$\leq 0,30$
	Mechanical properties							
	R_{ϵ} , MPa		R_m , MPa		A_5 , %		HB	
A11	400		500-750		8		159	
45	340		620		16		207	

The tool used in the research was a Mircona R-151S 2525x20x3 tool holder with interchangeable inserts made of TMC150 sintered carbide (P35 according to ISO) and CVD coated with TiC + Ti(C,N) + TiN, also produced by Mircona. The tool has been designed to be used with MQL equipment. The flat rake face (F) inserts had the following geometrical properties: $\kappa_f=90^\circ$ $\gamma_o=10^\circ$, $\alpha_o=5^\circ$, $\alpha_o'=6^\circ$ $\lambda_s=0^\circ$, $r_{\epsilon}=0,25$ mm. In the case of the shaped rake face with a chip breaker (B) it was $\kappa_f=90^\circ$ and $\kappa_r=95^\circ$ (Fig. 1).

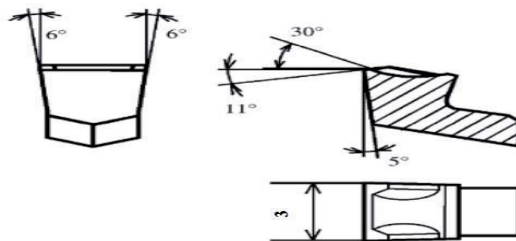


Fig. 1. Shape and geometry of tool insert with chip breaker.

In order to reduce tool wear on research results, for each cooling and lubrication mode a new insert was used.

The following cooling and lubrication modes were used:

MQL – minimal lubrication with oil aerosol,

D – dry cutting off, without cooling and lubrication liquid.

For MQL with Accu-Lube Minibooster MBII a LB8000 plant oil by Accu-Lube was used, which was designed for cutting steels, cast steels and non-ferrous metals. The aerosol generated by the Minibooster was fed into the cutting zone by means of channels in the tool holder, in the direction of the rake and flank face.

The cutting parameters used in the research are presented in table 2. Three different cutting speeds v_c and feed rates f were chosen. The cutting depth of cut was 3 mm, which equals to the width of the primary cutting edge.

Table 2. Cutting parameters

A11 steel					
$\kappa_r=90^\circ\text{F}, 90^\circ\text{B}, 95^\circ\text{B}$					
v_c (m/min)	67	105			132
f (mm/rev)	0,08	0,08	0,19	0,24	0,24
45 steel					
$\kappa_r=90^\circ\text{F}$					
v_c (m/min)	67	105			132
f (mm/rev)	0,08	0,19			0,24
a_p (mm)	3				

The cutting forces were measured with a Kistler 9247B force dynamometer connected to an amplifier and a computer with Dyno Ware software created by the manufacturer of the dynamometer.

3. Results and discussion

3.1. Cutting forces in cutting off A11 steel

The results of the research into an impact of the cooling and lubrication mode in the cutting zone on the total value of the cutting force in A11 steel cutting off machining are presented in fig 2. However the influence of the oil aerosol fed into the cutting zone depended on the used cutting parameters. For most cutting force values and feed rates employed in this research, the influence of the cooling and lubrication mode on the total force value proved negligible. The application of MQL in cutting off the A11 steel led to a decrease in the total cutting force in all the used cutting parameters. However, the influence of the MQL did not prove significant in each case. Apart from cooling and lubrication of the cutting zone, also the cutting edge angle and rake face shape proved to affect significantly the total force value.

For cutting off the A11 steel the greatest differences in this factor were observed for the following settings of the cutting speed and feed rate: 67/0,08; 105/0,19 for the insert with a chip breaker as well as 105/0,24 for the flat rake face. A comparison of cutting force values for cutting off with inserts with the flat rake face and with the chip breaker using the same angle $\kappa_r=90^\circ$ proved that shaping this surface for desired chip formation, which facilitates its movement in the groove, caused an increase in the cutting force, especially at higher cutting speeds and feed rates.

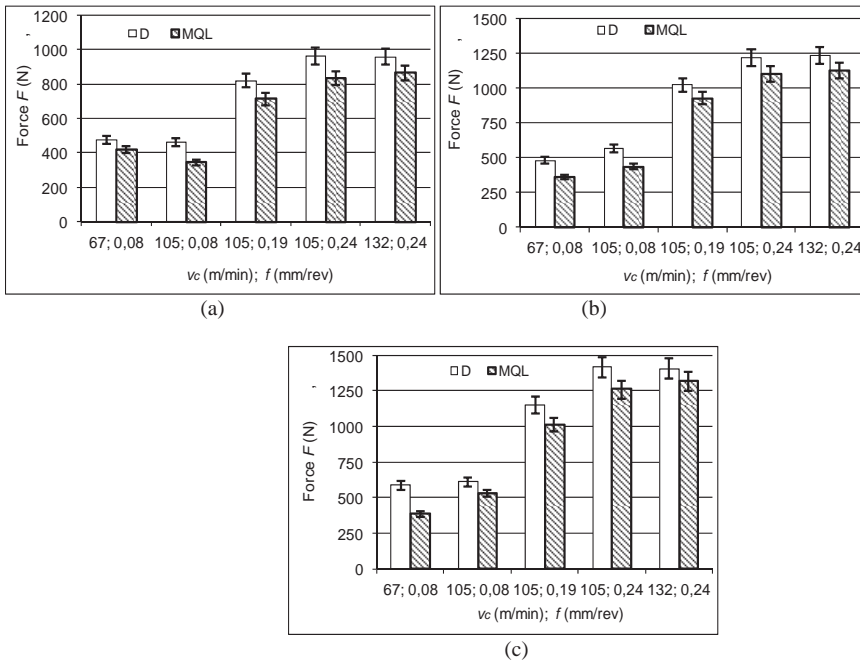


Fig. 2. Impact of cooling and lubrication mode on the total force F: a) $\kappa_r = 90^\circ F$, b) $\kappa_r = 90^\circ B$, c) $\kappa_r = 95^\circ B$

An analysis of the total force dependent on cooling and lubrication points to a positive influence of oil aerosol in the cutting off the A11 steel (fig. 3). In the range of used cutting parameters, the greatest impact on the total cutting force was exerted by the feed rate. Its increase always caused a significant increase in the cutting force and this holds for all cutting speeds set during the research. The impact of the cutting speed depends on the applied feed rate and increases as the feed rate increases. This contributes to a slight decrease in the cutting force resulting from a higher cutting temperature and a lower cutting resistance of the machined material. The impact of the cooling and lubrication mode is greater in the range of the increased feed rates (fig. 3b).

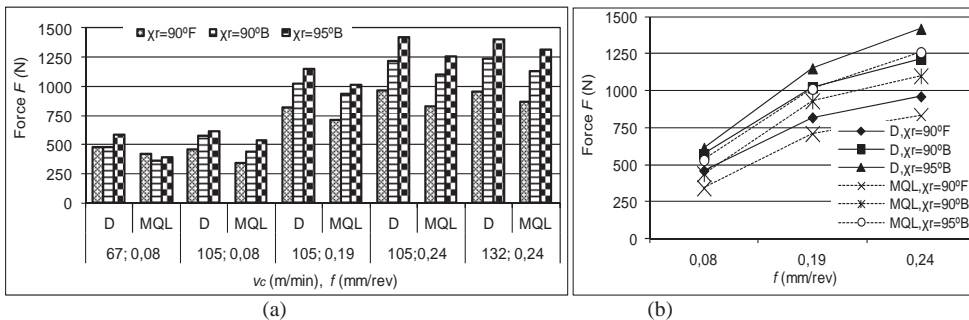


Fig. 3. Impact of κ_r angle, chip breaker and the cooling and lubrication mode (a) and feed rate (b) on the total force F

The progression of total cutting force components in the function of the cutting off diameter is shown in fig. 4. The greatest changeability especially at the end of the cutting off process was recorded for the cutting force component F_c , whose values increase or decrease in the final phase of the cutting off process as the cutting speed changes proportionally to the decreasing diameter of the machined sample. This is caused by unstable cutting conditions resulting from changes in tool edge angles during the cutting off process and its smaller cutting efficiency as well as from the loss of material continuity between the cut off object and the rod, which takes a form of a small pin on the rear surface of the cut off object. The diameter of the pin depends to a large extent on the tool cutting edge angle and for the angle $\kappa_r=90^\circ$ it reaches the highest values. The value of the F_f force ranges from 40 to 60% of the value of the F_c force and is characterized by greater stability during cutting. In the case of the angle $\kappa_r=90^\circ$ the force F_p takes minimum values around zero, which are negligible from the point of view of their impact on the other component forces as well as on the total force. An increase in the tool cutting edge angle up to $\kappa_r=95^\circ$ causes greater stability of the F_p force, but its value still remains low compared to those of the other component forces. Lubricating by means of oil aerosol did not reveal any significant impact on the component forces of the total force.

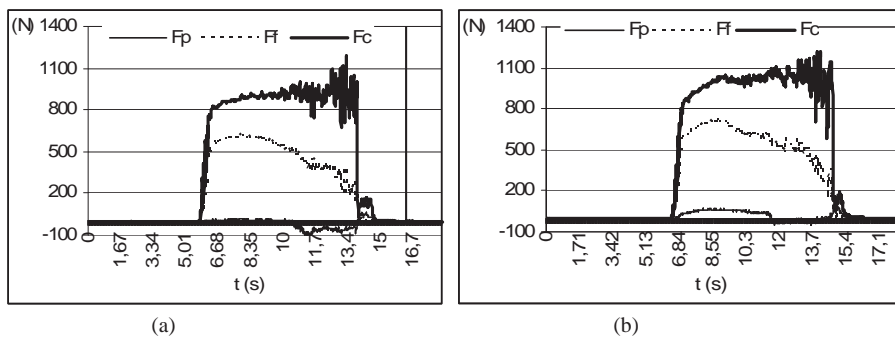


Fig. 4. Component forces F_c , F_f , F_p of the total force: a) $\kappa_r=90^\circ$ B, cutting dry, b) $\kappa_r=95^\circ$ B, MQL

The cooling and lubrication mode in the cutting zone as well as cutting parameters have a considerable influence on the component forces. The dependence of the component forces F_c and F_f in the function of tool cutting edge angle and the shape of the rake face is presented in fig. 5. For cutting speeds of 67 and 105 m/min and a feed rate of 0,08 mm/rev, the values of the component forces did not differ significantly although an increasing tendency was observed, which resulted from using a chip breaker and an increased tool edge angle. Clear differences between the values of the component forces appear at feed rates of 0,19 and 0,24 mm/rev. The highest values were recorded for an insert with a chip breaker and an angle $\kappa_r=95^\circ$, the lowest for flat rake face. The dependence of the component forces in dry machining and machining with MQL are similar.

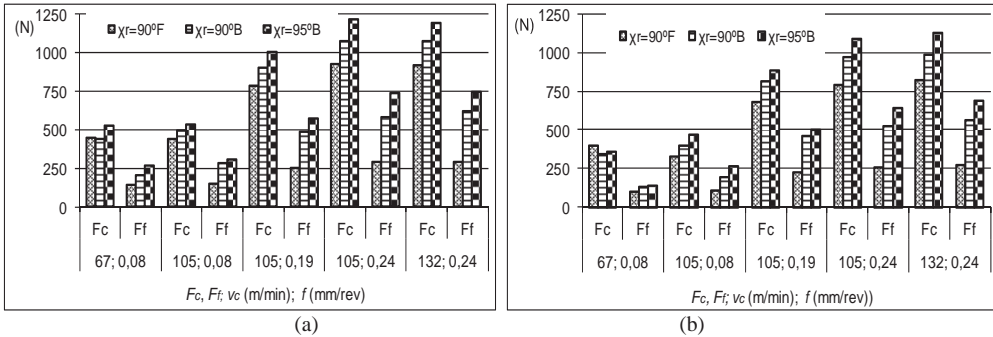


Fig. 5. Impact of κ_r angle, chip breaker and cooling and lubrication mode on component forces F_c and F_f in the range of used cutting parameters: a) machining dry, b) MQL

3.2. Cutting forces in cutting off C45 steel

The cooling and lubrication mode applied in the research into cutting off the C45 steel proved insignificant (fig. 6). In the range of used cutting parameters slightly lower values of the total force were observed in dry cutting off than in cutting off with oil aerosol. This considerably smaller impact resulted from worse access of the oil aerosol to the rubbing surfaces of the chip and tool point. A higher temperature in dry cutting of C45 steel may have caused lower material strength and thus a decreased cutting force. Minimal cooling and lubrication did not cause any significant differentiation of the component forces of the total force either. Depending on the cutting parameters, they had lower or higher values compared to dry cutting. The recorded cutting force for the same cutting parameters and tool point geometry was considerably higher for C45 steel than for A11 steel. For $v_c=132$ m/min and $f=0,24$ mm/rev the difference in the total force value as compared to A11 steel reached 25%, which means that the cutting conditions are much more difficult.

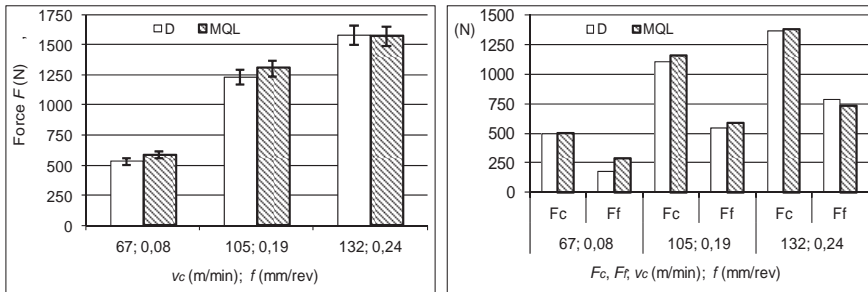


Fig. 6. Impact of cooling and lubrication mode on the total force F (a) and its components F_c and F_f (b), $\kappa_r=90^\circ F$

4. Conclusions

The conducted research has revealed a limited influence of minimal quantity cooling and lubrication in the cutting zone on reducing the cutting force as compared to dry machining in cutting off the A11 steel.

For the used cutting parameters minimal quantity lubrication allowed decreasing the cutting force compared to dry cutting. The action of the cooling and lubricating medium largely depended on the chosen cutting parameters.

In cutting off C45 steel the influence of minimal cooling and lubrication on the cutting force proved insignificant. The forces observed for the used cutting parameters were slightly lower in dry cutting off than in cutting off with MQL.

The research showed a significant impact of the cutting parameters on component forces and the total force in machining of both types of steel. The greatest impact was exerted by the feed rate and at a fixed feed rate the increase in the cutting speed caused the component forces and total force to decrease, especially at higher feed rates.

The research showed that with carefully chosen parameters it is possible to decrease the value of the cutting force in cutting off A11 steel. Replacing the conventional and generous application of machining liquid to the cutting zone with minimal cooling and lubrication helps reduce the negative impact of the machining liquid on the working environment.

References

- [1] Chen, W., *Cutting forces and surface finish when machining medium hardness steel using CBN tools*, International Journal of Machine Tools & Manufacture, 40, 455–466, 2000.
- [2] De Chiffre, L., Andreasen J. L., Lagerberg S., Thesken I.B., *Performance testing of cryogenic CO₂ as cutting fluid in parting/grooving and threading austenitic stainless steel*, CIRP Vol. 56 (1), 101-104, 2007.
- [3] Diniz, A.E., Micaroni R., *Cutting conditions for finish turning process aiming: the use of dry cutting*, International Journal of Machine Tools & Manufacture, 42, 899–904, 2002.
- [4] Gunay, M., Seker U., Sur G., *Design and construction of a dynamometer to evaluate the influence of cutting tool rake angle on cutting forces*, Materials and Design, 27, , 1097–1101, 2006.
- [5] Gunay, M., Korkut I., Aslane., Seker U., *Experimental investigation of the effect of cutting tool rake angle on main cutting force*, Journal of Materials Processing Technology, 166, 44–49, 2005.
- [6] Li Kuan-Ming, Liang S.Y., *Modelling of cutting forces in near dry machining under tool wear effect*, International Journal of Machine Tools & Manufacture, 47, 1292–1301, 2007.
- [7] Machado, A.R., Wallbank J., *The effect of extremely low lubricant volumes in Machining*, Wear, 210, 76-82, 1997.
- [8] Obikawa, T., Kamata Y., Shinozuka J. *High-speed grooving with applying MQL*, International Journal of Machine Tools & Manufacture, 46, 1854–1861, 2006.
- [9] Wienert, K., Inasaki I., Sutherland J.W., Wakabayashi T. *Dry machining and minimum quantity, lubrication*,. CIRP vol. 53 (2), 511-537, 2004.

INFLUENCE OF CONNECTION TYPE ON THE FATIGUE LIFE OF WELDED

Stanisław Mroziński¹, Michał Piotrowski²
Michał Burak³ Łukasz Pejkowski⁴

*University of Technology and Life Sciences in Bydgoszcz, Faculty of
Mechanical
Engineering, Al. Prof. S. Kaliskiego 7, 85-789
Bydgoszcz*

tel.: 48 52 340-82-64, fax: 48 52 340-82-71

¹ *e-mail: mrozinski.stanislaw@utp.edu.pl*

² *e-mail: m.piotrowski@utp.edu.pl*

³ *e-mail: mibu@utp.edu.pl*

⁴ *e-mail: lukasz.pejkowski@utp.edu.pl*

1. Introduction

The technology of welding materials together is one of the most widespread methods of inseparable joining. The predominant majority of the mechanical industry uses this joining method to build new constructions and as well as to regenerate damaged objects.

There has been invented many different methods of making joints characterized by the thermal energy input, the way of creating the protected atmosphere, etc. There can be distinguished a few basic types of Welded joints (Fig.1):

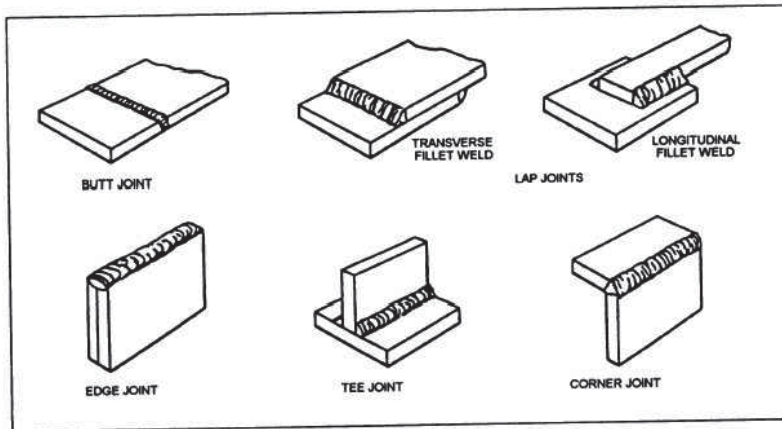


Fig. 1. Welded joints

Each of the welding methods and the type of weld has many various advantages in the form of: the possibility of joining different kinds of materials, easy process automation, the possibility of welding in unfavorable environments (e.g. underwater), tightness of the joint and many more. Nevertheless, despite the many advantages the welding process has a number of drawbacks, which oftentimes prevent employing this method entirely [1]. The most detrimental of them are: the material structural change in the heat affected zone and the thermal deformations, which are caused by the distribution of condensed thermal energy in huge amounts. The structural change of the material has an obvious impact on the tensile and fatigue strength. After-welding deformations cause a large amount of stresses in the weld itself, in the heat affected zone, but also in the whole constructions in specific cases. By employing various welding methods we can reduce the degree of stresses, but they can never be fully eliminated. In the case of an inappropriately designed construction there is a possibility of a huge accumulation of stresses, which is shown in Fig. 2. It is vitally important to appropriately design the routes and types of the welds used [4]. The scope of the experiment encompassed testing four types of samples in a environment of static and variable loads.

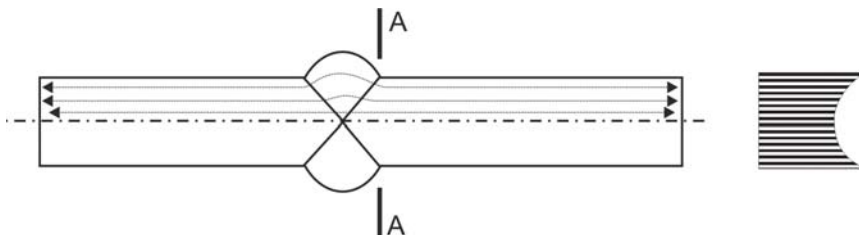


Fig. 3. Stress accumulation in the weld

In welds there can be found stress accumulation resulting from:

- mechanical notch (local change of the object's shape)
- structural notch (local change of the material's structure)
- welding defects
- additional welding stresses

2. Test samples

The experiment was conducted according to norms PN-EN ISO 6892-1:2009 and PN-74/H-04327- Fatigue Testing of Metals. The static elongation test was carried out in the room temperature. Four types of test samples were used out of steel grades 650 (6) and 700 (7). The shape of the samples is shown in Fig. 3.

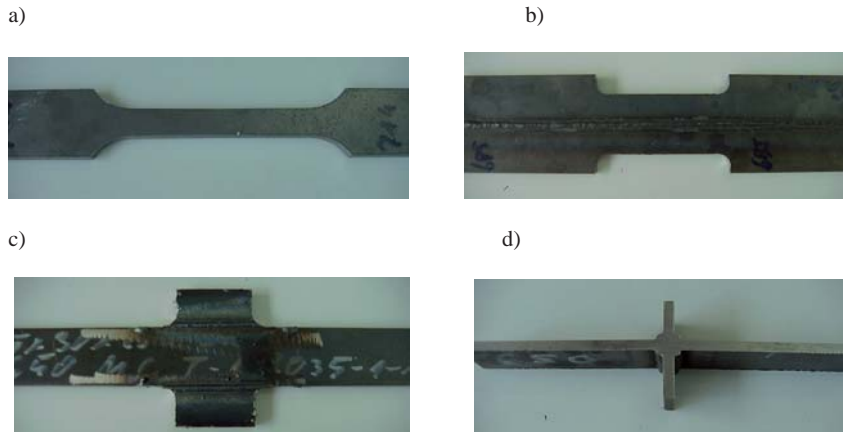


Fig. 3. Test samples: a) uniform sample (type A), b) with a longitudinal weld (type B), c) with longitudinal welds (type C), d) cross joint (type D)

3. Experiment methodology

3.1. Static tests

Fatigue tests were preceded by static tests [2]. Static elongation tests were conducted using the Instron 8501 tester machine equipped with a force gauge head of the ± 100 kN measuring range. Elongation values were taken using an extensometer for static tests with the measuring base of 50mm secured on the measured part of the sample. The experiment composed of subjecting the test samples to loads which increased with the speed of the piston feed of the tester machine equaled 0.05 mm/s. Fig.4 shows the samples secured in clamps of the tester machine.

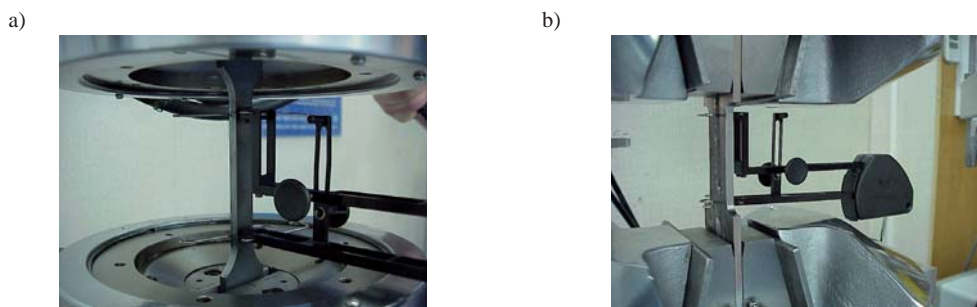


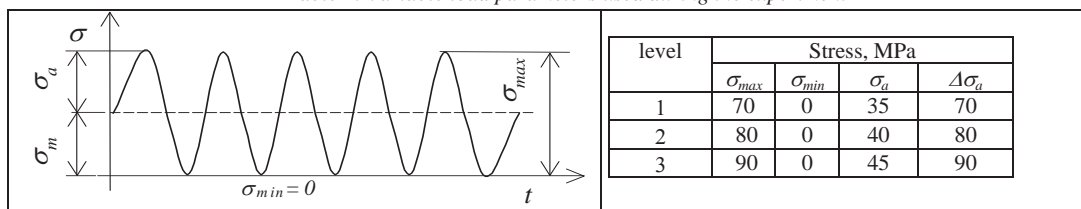
Fig. 4. Samples in the clamps of the tester machine: a) samples with a weld (type A), b) sample with the longitudinal weld (type B)

The experiment was conducted at the temperature of 21°C. The tests were being conducted up to the point of the sample split within the measuring range of the extensometer. During the test the temporary values of load force affecting the sample were registered and its elongation.

3.2. Fatigue tests

The test samples were subjected to sinusoidal elongation loading (Tab. 1) [3]. Load levels were determined after an analysis of the static elongation tests' results. The variable load parameters are shown in Table 1.

Table 1. Variable load parameters used during the experiment



Fatigue tests were ended at the point of the sample split. Fig 5 shows the samples already prepared for the fatigue tests.

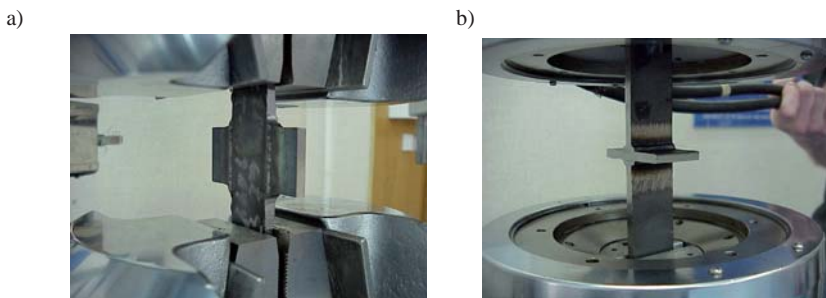


Fig. 5. The samples during the fatigue tests: a) with longitudinal welds (type c), b) cross-type sample (type D)

4. Results and analysis

4.1. Static tests

The form of the sample's damage was interconnected with the type of the sample. In the case of the sample with the weld (type A) and the sample with the longitudinal weld the crack always appeared in the sample measured area (Fig. 6 a, b). This applied to both steel grades. As for the two remaining sample types the crack always appeared in the vicinity of the weld. An exception here is the cross-joint sample where the welded joint always broke in the weld area. The cracks of type samples C and D are shown in Fig. 6c i 6d.

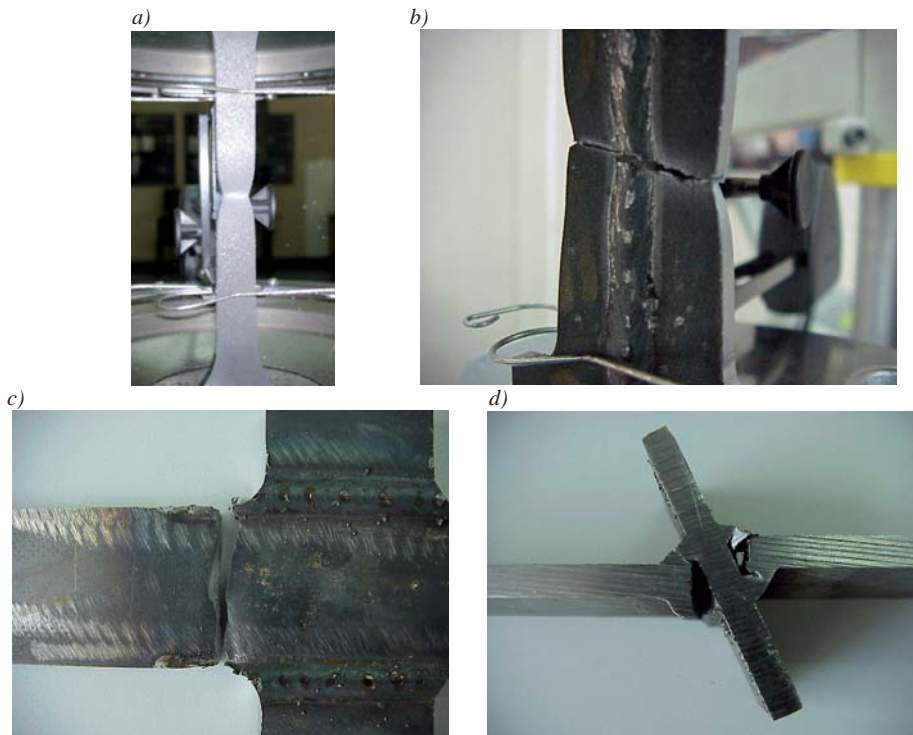


Fig. 6. Forms of the damage during the static tests: a) damage of the type A sample, b) damage of the type B sample, c) damage of the type C sample, d) damage of the type D sample

The static elongation test are shown in the form of graphs on the coordinate system: test sample elongation – stress. The stresses in the test sample subjected to tensile load were calculated dividing the temporary values of load force by the initial cross-sectional area of the sample. As the initial cross-sectional area of the sample the following was assumed:

- for type A sample – section determined by crosswise dimensions of the sample;
- for type B sample – section determined by crosswise dimensions of the sample outside the weld;
- for type C sample – section determined by crosswise dimensions of the sample outside the weld;
- for type D sample – section determined by crosswise dimensions of the sample outside the weld.

The graphs depicting elongation can be found in Fig 8.

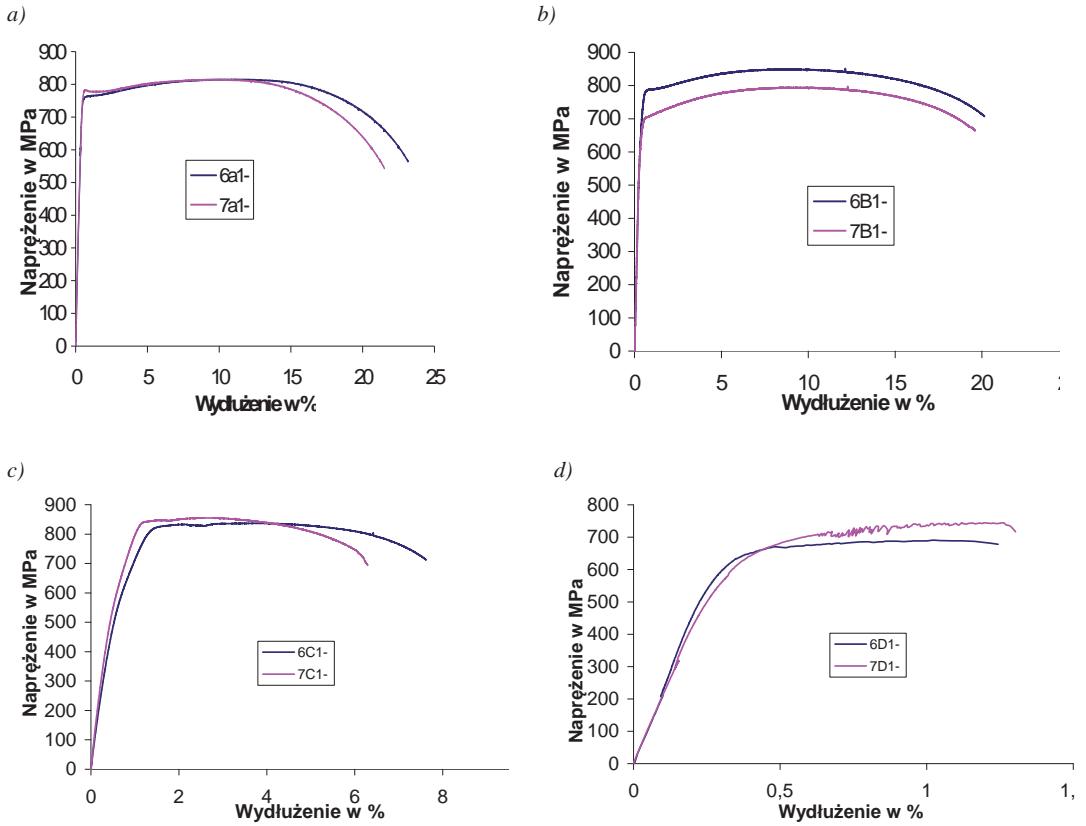


Fig. 8. Static elongation graphs: a) sample with the weld Type A, b) Type B, c) Type C, d) Type D

The graphs analyzed in detail. The results are grouped in Table 2.

Table 2. Result of the static elongation graphs' analysis

No.	Sample type	Steel grade 650			Steel grade 700		
		R _m	R _e	A	R _m	R _e	A
1	A	815	754	22,66	814	779	21,51
2	B	850	766	21,12	797	695	20,68
			R _{p0.2}			R _{p0.2}	
3	C	855	594	8,02	872	664	6,67
4	D	691	668	1,25	744	689	1,3

Fig. 8 shows the most common forms of damage during the fatigue tests.

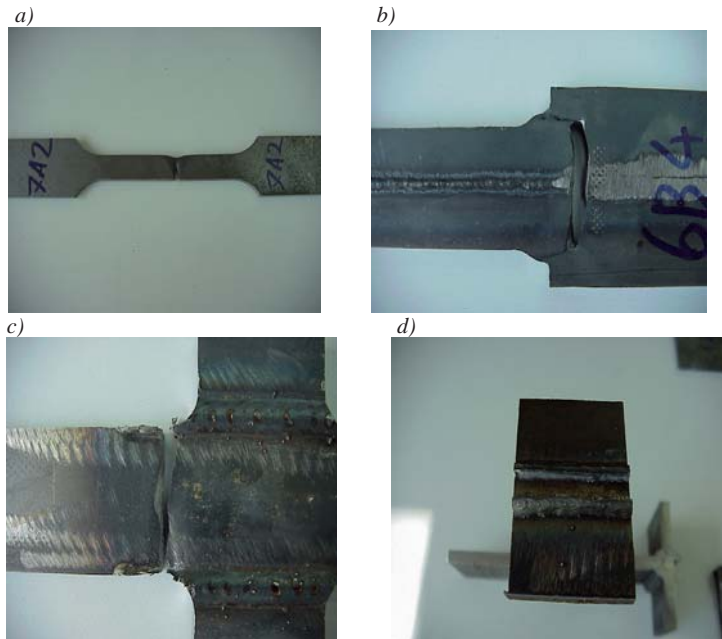


Fig. 8. Forms of damage during the fatigue tests: a) type A, b) type B, c) type D, d) type D

The results obtained during the fatigue tests are shown in Fig. 10 and 11 in the forms of fatigue graphs on the coordinate system: cycle number till the point of break N – stress σ_{max} . The fatigue graphs in the bilogarithmic form were approximated using the following equation:

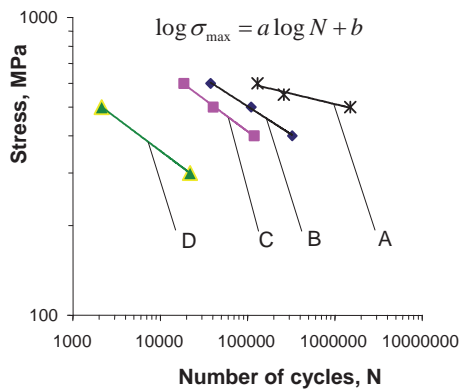
$$\log \sigma_{max} = a \log N + b, \quad (1)$$

where:

a - gradient of the graph,

b - the intercept of the regression graph.

a)



b)

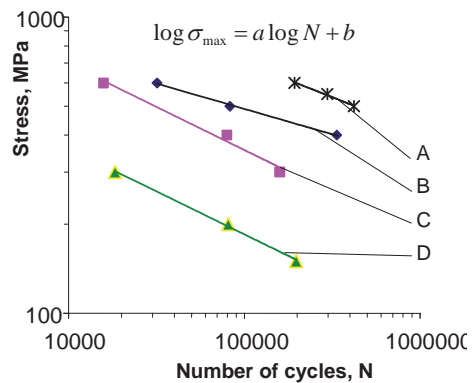


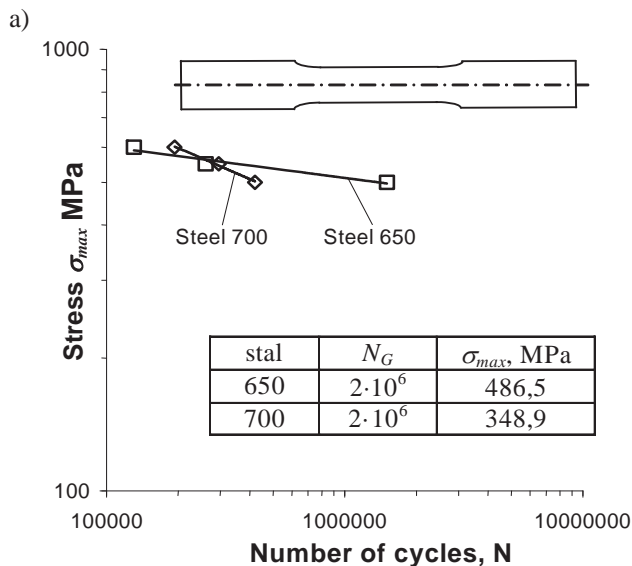
Fig. 9. Fatigue graphs: a) steel grade 650, b) steel grade 700

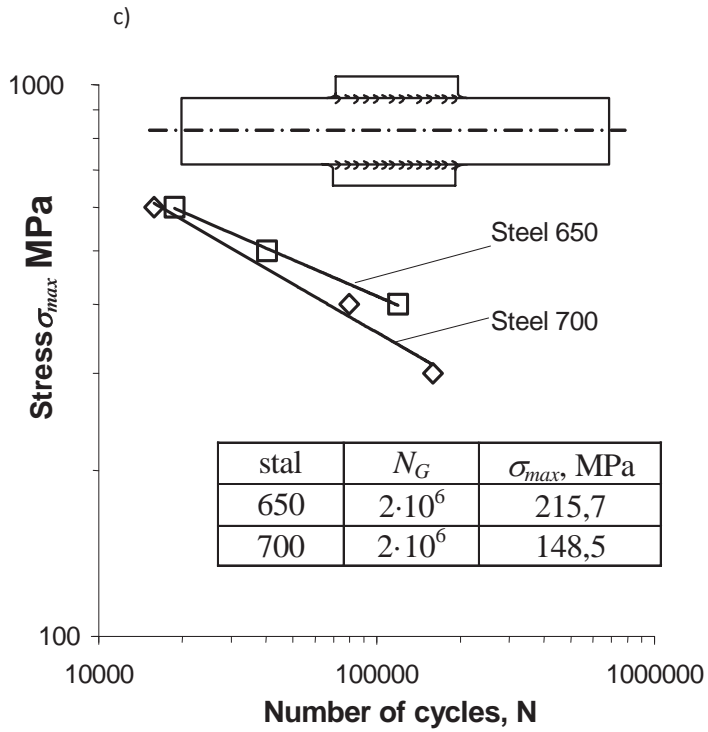
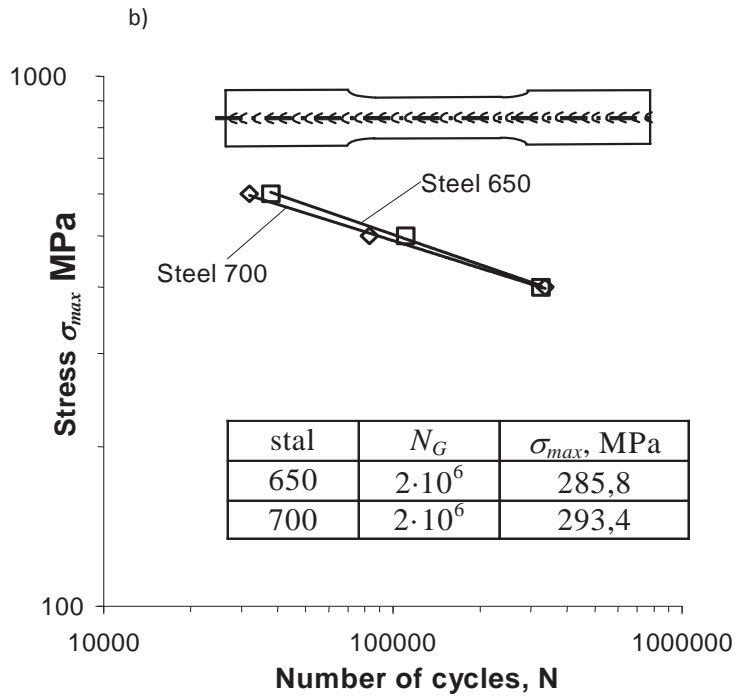
From the fatigue graph equation the values of stresses were calculated corresponding to the base number of cycles: $N_G=10^6$, $N_G=2 \cdot 10^6$ and $N_G=10^7$. The obtained results are listed in Table 3 and in Fig. 10.

Table 3. Fatigue graph parameters for the test sample from steel 650 and 700

Sample type	Steel	Equation	a	b	σ_{max} for $N_G=2 \cdot 10^6$
A	650	$\sigma_{max}=a \log N+b$	-	1355	486,5042
	700		0,0706	10300	348,9851
B	650		-	4403,9	285,8204
	700		0,1885	3518	293,4672
C	650		-	5079	215,7963
	700		0,2177	10189	148,5975
D	650		-	5226,6	77,45158
	700		0,2903	3576,2	91,57599

For the comparison of the fatigue life results of the same type samples made from steel 650 and 700 fatigue graphs in Fig. 9 were plotted.





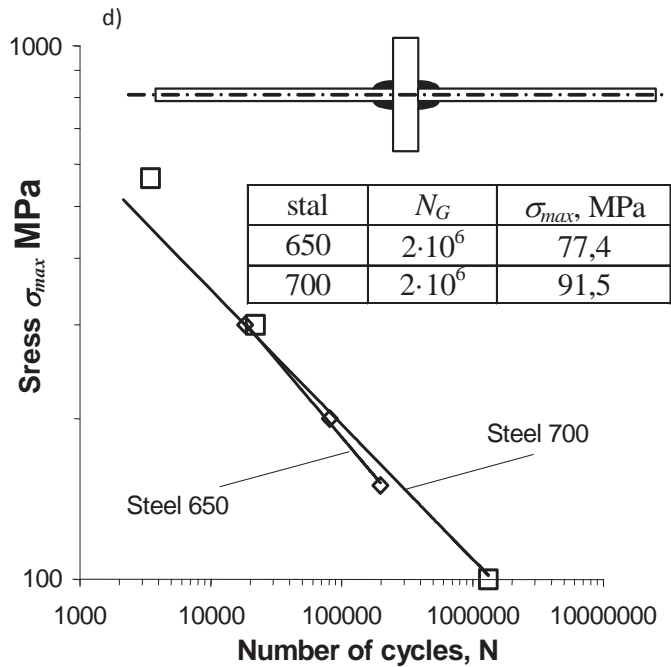


Fig. 10. Fatigue graphs obtained from different sample types: a) uniform sample (type a), b) with the longitudinal weld (type b), c) with the longitudinal welds (type c), d) cross-joint (type d)

4. Summary

The results of the laboratory tests containing counterfeit and without weld joints are made of two sheets of homogeneous species allows us to formulate the following general conclusions: strength is strongly dependent on the type of weld as well as a method of congestion;

- fatigue life of samples arranged in a sequence dependent on the nature of the sample (in the order of D, C, B, A) which does not change its place for the different materials;
- fatigue limit of $2 \cdot 10^6$ cycle for samples A and C has a higher level of stress for steel 650, which is changed in favor of the steel type 700 for samples B and D;
- the occurrence of weld samples tested leading to immediate increases strength and reduces fatigue strength compared to the native materials.

The results of the study sheets bonded the two most common types of welds showed that the type of bond has a significant effect on the strength and fatigue received emergency calls:

- Front - high load capacity fixed and variable;
- fillet - easy to make, lower strength especially in the case of variable loads.

Junction and its location due to strength should be considered in the design of welded objects.

Reference

- [1] http://engineeringtraining.tpub.com/14070/css/14070_37.htm

- [2] PN-EN 10002-1:2004. *Metale. Próba rozciągania. Metoda badania w temperaturze otoczenia.*
- [3] PN-74/H04327- *Badanie metali na zmęczenie. Próba osiowego rozciągania ściskania przy stałym cyklu obciążeń zewnętrznych*
- [4] Muchryj J., Stachurski M., *Badania złączy spawanych*, Biuro Gamma, Warszawa 2003

FATIGUE BEHAVIOR OF PURE COPPER IN NON-PROPORTIONAL LOAD CONDITIONS

Łukasz Pejkowski, Dariusz Skibicki, Michał Burak, Michał Piotrowski

*University of Technology and Life Sciences
al. Prof. S. Kaliskiego 7, 85-789 Bydgoszcz
tel.: +48 52 3408202, +48 52 3408247*

*e-mail: lukasz.pejkowski@utp.edu.pl, dariusz.skibicki@utp.edu.pl, mibu@utp.edu.pl,
m.piotrowski@utp.edu.pl*

Abstract

This paper deals with fatigue behavior of pure copper in different load conditions, including complex proportional and non-proportional loads. The material has been chosen due to its potential high sensitivity for non-proportional loads. The aim of this paper is search for relationship between the fatigue life of pure copper and shear stress vector paths in non-proportional load conditions.

Keywords: *multiaxial fatigue, non-proportional load, copper*

1. Introduction

For many materials an influence of non-proportional load on fatigue life and strength can be observed [1, 2]. This influence is manifested by decrease of fatigue life and fatigue limit. It can be shown on S-N curves diagram for equivalent stresses calculated using the common fatigue criteria (Fig .1).

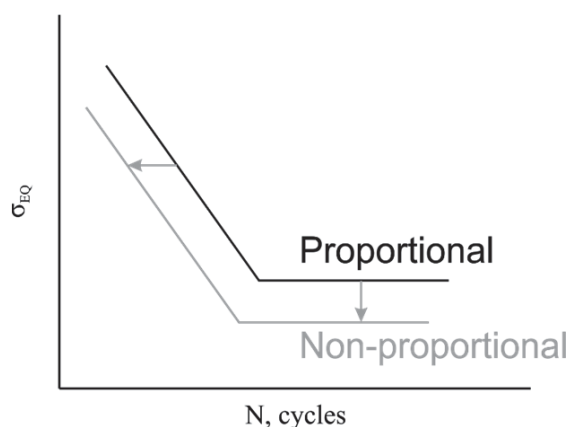


Fig. 1 – Influence of non-proportional load on fatigue life and fatigue limit.

An example of non-proportional load is out-of-phase tension-compression with torsion. In this case, non-proportionality of load is caused by phase shift between sine signals of axial and torsional load. From the point of view of signals, the highest non-proportionality of load takes place when the phase shift angle is $\delta = 90^\circ$ [3, 4] (Fig. 2).

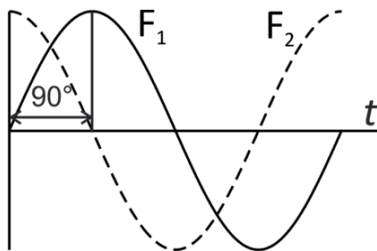


Fig.2 – Highest non-proportionality of load in out-of-phase load type.

Another factor that affects the level of non-proportionality of load is axial amplitude $\sigma_{TC,a}$ and torsional amplitude $\sigma_{T,a}$ ratio, denoted as λ , which can be written as follows:

$$\lambda = \frac{\sigma_{TC,a}}{\sigma_{T,a}}. \tag{1}$$

A characteristic feature of non-proportional load is a change of shear stress vector direction, acting on a sectional plane Δ . In case of uniaxial and proportional load the shear stress vector path is straight line, because, the vector changes only its magnitude. But when load components changes non-proportionally also the direction of the shear stress vectors changes. The result is path, different than straight line. In case of out-of-phase load it is always an ellipse (Fig. 3.). The shape of this ellipse depends on phase shift and λ ratio.

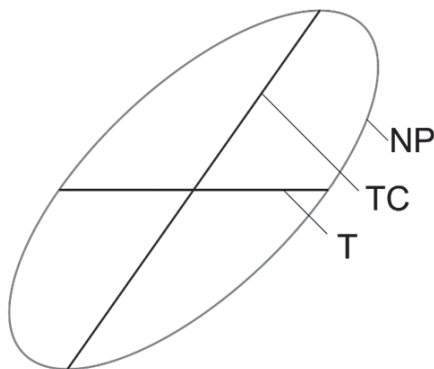


Fig. 3 – Shear stress vector paths for tension-compression TC, torsion T and non-proportional out-of-phase load NP.

The objective of this paper is to find relationship between the shape of shear stress vector's path for out-of-phase load and fatigue life of pure copper Cu-ETP.

2. Testing methods and conditions

Hourglass shape specimens for fatigue tests have been made of pure copper Cu-ETP (EN: CW004A, DIN: E-Cu58, ASTM: C11000) by machining. Basic monotonic and cyclic

properties of the material are given in Tab1. The geometry of specimen has been shown on Fig. 4.

Tab. 1. Monotonic and cyclic properties of Cu-ETP copper

$R_{p,0.2}$, MPa	R_m , MPa	A, %	E, GPa	Z_{so} , MPa [5]	Z_{rc} , MPa [5]
360	367	36,16	131	28	50

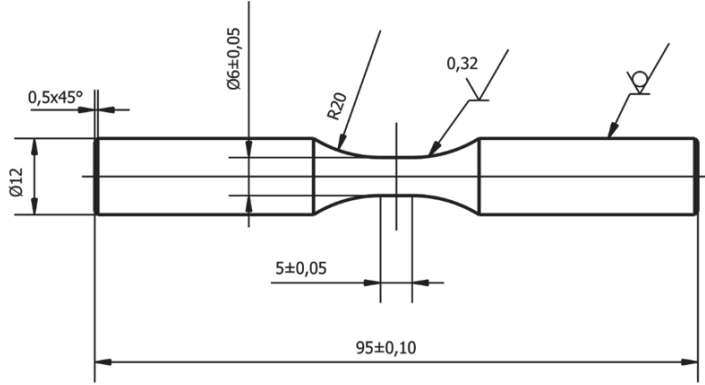


Fig. 4 – Tested specimen's geometry.

Specimens has been tested on INSTRON 8874 multi-axial testing system, using different fully reversed load types: tension-compression, torsion, combined proportional tension-compression with torsion ($\lambda = 0.5$, $\delta = 0^\circ$) and combined out-of-phase tension-compression with torsion ($\lambda = 0.3$ to 0.8 , $\delta = 90^\circ$).

Amplitudes of load components were chosen in the way that gives the same maximum value of equivalent stress calculated with use of Zenner and Liu criterion [5] during the load's cycle (Fig. 5). For loads with no mean values this criterion can be written as follows:

$$\sigma_z = \sqrt{\frac{15}{8\pi} \int_{\gamma=0}^{\pi} \int_{\varphi=0}^{2\pi} (a\tau_{\gamma\varphi,a}^2 + b\sigma_{\gamma\varphi,a}^2) \sin \gamma \, d\gamma d\varphi} \leq Z_{rc}, \quad (2)$$

where a and b are coefficients calculated from fatigue limit for tension-compression and torsion:

$$a = \frac{1}{5} \left(3 \left(\frac{Z_{rc}}{Z_{so}} \right)^2 - 4 \right), \quad b = \frac{2}{5} \left(3 - \left(\frac{Z_{rc}}{Z_{so}} \right)^2 \right), \quad (3)$$

$\tau_{\gamma\varphi,a}$ and $\sigma_{\gamma\varphi,a}$ are the amplitudes of nominal shear stress $\tau_{\gamma\varphi}$ and normal stress $\sigma_{\gamma\varphi}$ acting on a sectional plane Δ [3, 7]:

$$\sigma_{\gamma\varphi} = \mathbf{n} \cdot \boldsymbol{\sigma} \cdot \mathbf{n}, \quad \tau_{\gamma\varphi} = \boldsymbol{\sigma} \cdot \mathbf{n} - (\mathbf{n} \cdot \boldsymbol{\sigma} \cdot \mathbf{n})\mathbf{n}, \quad (4)$$

where the unit vector normal to Δ plane is denoted as \mathbf{n} .

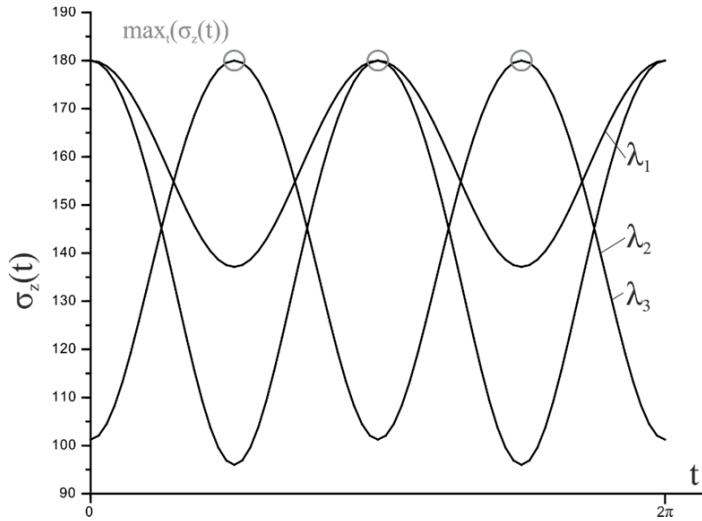


Fig. 5 – Result of equivalent stress calculation for each moment of the non-proportional load cycle with different values of λ ratio.

Non-proportional load cycles that gives the same value of equivalent stress but has different values of λ ratio, also gives different shapes of shear stress vector path. On the Figure 6 shear stress vector paths for λ ratio range from 0.3 to 0.8 has been shown. One can notice that the path with the greatest area occurs for $\lambda = 0.5$, which is approximately equal to quotient of fatigue limit for torsion Z_{s0} and fatigue limit for tension-compression Z_{rc} [5].

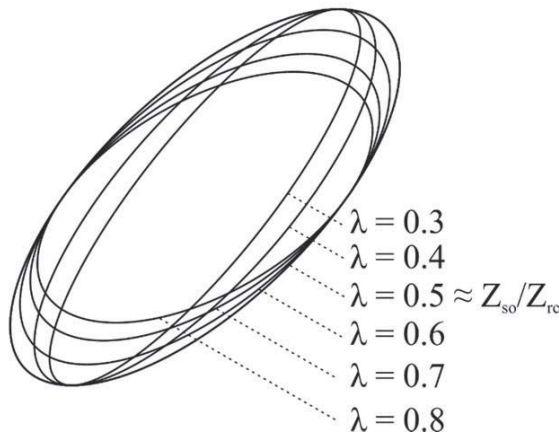


Fig. 6 – Shear stress vector paths for λ ratio range from 0.3 to 0.8.

3. Results

The results are shown on the S-N curves diagram, made for equivalent stresses calculated with use of Zenner and Liu criterion, in the way described above (Fig. 7). Curves are depicted by the Basquin equation [8]:

$$\sigma_{eq} = AN^B. \quad (5)$$

Coefficients A and B are given in Tab. 3. For torsion and proportional load curves approximately overlaps with tension-compression curve, which means that equivalent stresses are calculated properly. Difference occurs for non-proportional loads. One can observe decrease of fatigue strength. It can be also interpreted as an underestimation of fatigue life. The maximum decrease appears for λ ratio equal to 0.5.

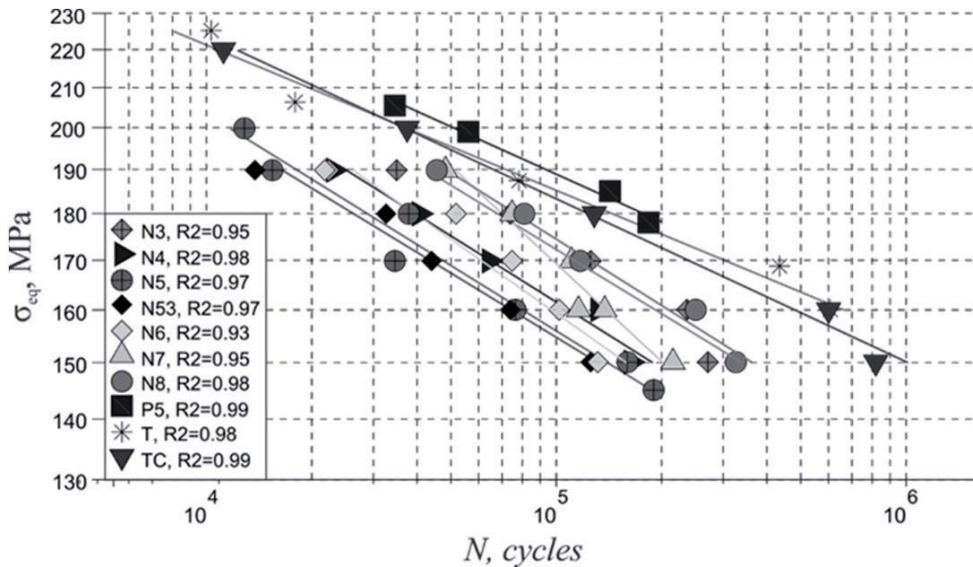


Fig. 7 – S-N curves diagram made for different types of load: TC – tension-compression, T – torsion, P – proportional load, N – non-proportional load. Numbers next to the letters are values of λ ratio times 10. Coefficient of determination was denoted as R2.

Tab. 3. Basquin equation coefficients for different types of load

Load type	Test frequency, HZ	A	B	λ	δ , degrees
TC	5	496.69	-0.087	0	0
T	2	450.74	-0.077	∞	0
P5	2	496.15	-0.084	0,5	0
N3	2	635.18	-0.113	0,3	90
N4	2	619.67	-0.117	0,4	90
N5	2	588.27	-0.115	0,5	90
N53	2	570.47	-0.113	0,53	90
N6	2	718.43	-0.131	0,6	90
N7	2	1228.70	-0.172	0,7	90
N8	2	671.12	-0.117	0,8	90

4. Conclusions

The material that has been tested has shown high sensitivity for non-proportional loads. For the most damaging non-proportional load, which for this material is the one with λ ratio equal to 0.5, fatigue strength calculated with frequently used Zenner and Liu criterion is approximately 15% lower than for tension-compression. Values of λ above and below 0.5 are gradually less damaging for material

The λ ratio value equal to 0.5 gives also the shear stress vector path with the largest area which also encloses other paths. The size of these paths seems to be related to λ value and fatigue life and strength. The larger the area of the path is, the higher level of fatigue strength decrease and shorter life occurs.

References

- [1] McDiarmid D. L., *Fatigue under out-of-phase bending and torsion*, Fatigue Fract. Engng Mater. Struct., 9, pp. 457-475, 1987.
- [2] Ellyin F., Goloś K., Xia Z., *In-phase and out-of-phase multiaxial fatigue*, ASME Journal of Engineering Materials and Technology 113, pp. 112-118, 1991.
- [3] D. F. Socie, G. B. Marquis, *Multiaxial fatigue*, SAE International, 2000.
- [4] M. Noban, H. Jahed, A. Ince, *Loading Phase Angle Effect on Multiaxial Behaviour of 30CrNiMo8HH*, proceedings of ICMFF9, Parma, Italy, June 7-9, pp. 479-486, 2010.
- [5] J. Zhang, Y. Jiang, *Fatigue of polycrystalline copper with different grain sizes and texture*, Int. J. Plasticity, 22, pp. 536 – 556, 2006.
- [6] H. Zenner, A. Simbürger, J. Liu, *On the fatigue limit of ductile metals under complex multiaxial loading*, Int. J. Fatigue, 22, pp. 137 - 145, 2000.
- [7] I. V. Papadopoulos et al., *A comparative study of multiaxial high-cycle fatigue criteria for metals*, Int. J. Fatigue, 19, pp. 219 – 235, 1997.
- [8] R. I. Stephens et al., *Metal fatigue in engineering*, Wiley 2000.

ASSESSMENTS OF THE IMPACT EXTRUSION DIE GAP ON THE QUALITY IN TECHNICAL BLOWING PRODUCT

Karol Pepliński

Bydgoszcz University of Technology and Agriculture
ul. Aleja Prof. S. Kaliskiego 7, 85-789 Bydgoszcz, Poland
tel.: +48 52 3408224, fax: +48 52 3408222
e-mail: karolpep@utp.edu.pl

Abstract

Extrusion blow molding is the technological process of processing polymeric materials for the growing market popularity, resulting from the increase demand for container produced manufacturing by this technique for cosmetics, pharmaceuticals as well as technical product used in the automotive industry. Implementation of the extrusion blow molding process in the work polymer processing system is determined by many factors including technological parameters, which influence the quality of a manufacturing hollow product. Obtaining a product with the most uniform wall thickness distribution is made possible by the use in the extrusion heads control systems such as VWDS. The system can change the size of the opening die gap, resulting in thickening or thinning the extruded parison in the places where the parison is blown in a different blow ratio degree, so as to avoid excessive thinning final product. In the present study was shown the effect of opening die gap on the quality blowing parts (intake manifold airflow in a motor vehicle) in relation to the value of the product weight and wall thickness in critical areas required by the customer of the product.

Keywords: *extrusion blow molding, die gap, wall thickness, product weight*

1. Introduction

Extrusion blow molding (EBM) is one of the major technological processes used in blow plastic. In addition to its significance is injection blow molding (IBM) and injection stretch blow molding (ISBM). Extrusion blow molding is the biggest share among the three of these technologies. It is estimated that the total blow molding industry is growing every year in the number of 3 to 5% and this trend is maintained [1].

Extrusion blow-molding is a manufacturing process that in the great advantage as a base material using a high density polyethylene. European demand for PE-HD, to the wider plastics processing technology, in 2011 accounted for 12% of the total production of plastics [9].

This type of plastic is used for the production of blowing packaging for cosmetics, chemicals and all kinds of technical creations. Blow molding products can counted to the group of hollow products. They can be classified in this group if they meet the following geometrical requirements: have a relatively thin wall, which runs around a hollow space, and the holes present in these objects are much smaller than the inner surface such as: bottles, fuel tanks, road cones. Hollow plastic parts reach a volume of several milliliters to several hundred liters [2].

2. Description of blowing process

In a conventional extrusion blow molding process, in the extruder take place the preparation of melting polymer. Plasticized material is directed to the extrusion head, where the parison is placed in a blow mold, welded in a pinch off area and shut off. Welding and prepare to cut the parison is due to specially shaped elements on the surface of pinch-off section. Blowing process, usually by compressed air, followed until the contact of the parison with the cavity walls and mapping the surface [7]. Finally blown product, after cooling in the mold cavity, leaving the mold, followed by removal of the flash in the finishing station (or partially by hand in the case of complex structure of the technical products), where the product goes to the quality control station. If hollow product meet the requirements goes to the customer.

In the case of blowing technical products of larger sizes, or extruded weight of the parison (over 2 kg) apply discontinuous extrusion blow molding. This includes the periodic rapid extrusion of parison by accumulator head. Extrusion cycle is starting when the mold is ready to accept a parison. Blowing mold is placed just below the extrusion head. Fast discontinuous extrusion reduces the tendency to stretch the parison under its own weight, and is usually achieved by accumulating head. Also in the case of an extruded parison diameter exceeding 130 mm is used the divergent die head extrusion nozzle [4]. During extrusion blow molding should also take into account aspects of the energy resources management [8] due to that, in the case of some technical parts reaching up to 85% the technological flash. These flashes are selected to be recycled. A much more detailed description of the process of extrusion blow molding products can be found in Meyer Kutz [1].

3. Explanation of experiment

For research task of assessing the impact of the extrusion gap on the quality of a blowing part with respect to the values of the weight and wall thickness in critical areas required by the customer of the product, used blow molding machine type Battenfeld VK3-200 with accumulator head, blow mold (Fig. 1) and partially automated waste disposal stations. Discussed produced part is airflow duct for one of the leading brands of cars, visible in the CAD form model in Figure 2. Investigations were realized in an industrial company Graform Bydgoszcz [3].

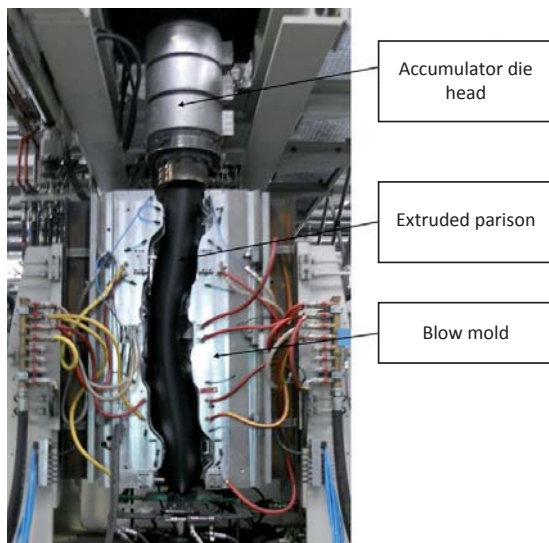


Fig. 1. Extrudate parison when locating in a blow mold [3]

The material, which was performed technical product is high density polyethylene trade name Marlex HHM 5502 BN of 0.35 g/10 min melt flow index. Recommended processing temperature for this type of material are within 171÷204 °C. To the blowing process used this same recycled material added in the number of 70% of virgin material and added a black dye added to the material in an amount of 1%.



Fig. 2. Air duct geometry for motorization (technical product) [3]

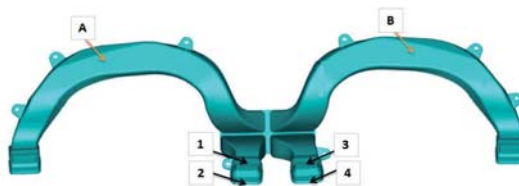


Fig. 3. The critical measurement points which should be saved referred dimensional tolerances

The research began with the adjustment the die gap in extrusion head of value 8.5 mm, after which in each case after the experimental trials for 12 blown products, these setting increased by 0.5 mm up to a value 13.5 mm. The aim is to determine at what value of the die land and programmed VWDS parison profile controlled at 62 points of its length are possible to meet the criteria the value of weight and wall thickness. Blow pressure was $p = 8$ bar, cycle time $T = 68.2$ s. The criterion of weight values according to the findings of the client must be $620 \text{ g} \pm 31 \text{ g}$ while maintaining a wall thickness value criterion in mounting areas (1, 2, 3, 4) should be $1,2^{+0,2}_{-0,4}$ mm and wall thickness of a product in the area A and B within $1,3^{+0,3}_{-0,3}$ mm. These points are shown in Figure 3.

As a result of the extrusion blow molding process was obtained products with flash – technological overmeasure (Fig. 4). The flash was removed by finishing station and directed to a recycling. Next, using a wall thickness device – Magna Mike 8500 GE Panametric, at designated locations wall thickness and the weight of a product were measured.

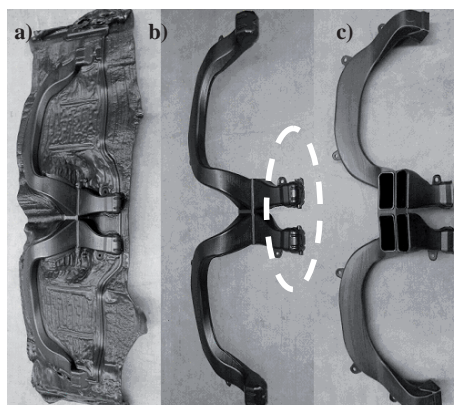
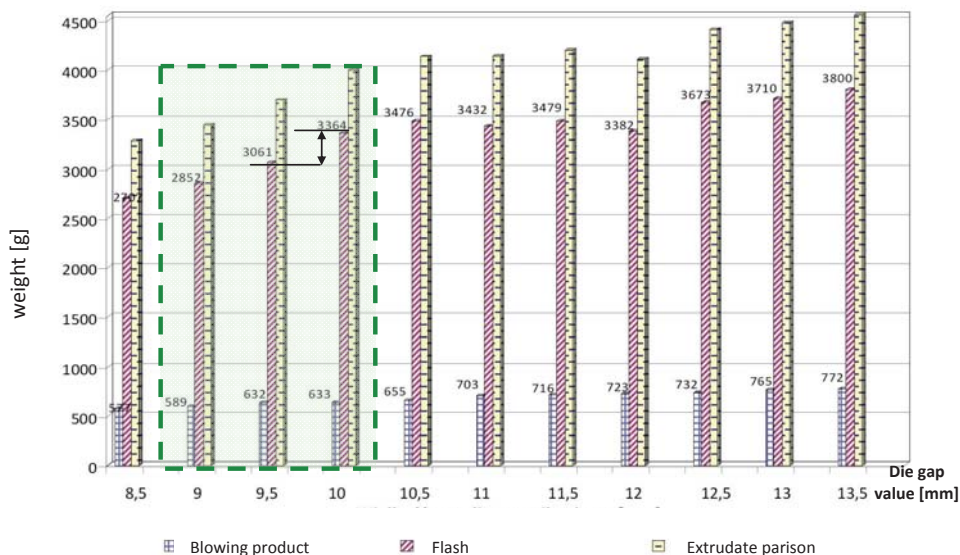


Fig. 4. Real production of air duct product: a) product with technological flash, b) the blowing product with of waste technological flash in assembly area, c) the final product

4. The results of blowing process

As a result of measures both the thickness and weight of the air ducts was obtained results with a average value (weight of a product, technological waste weight – flash and the total mass of the extruded product) is given in Figure 5. According to the criterion of weight air duct, it is noted that the weight of a blow product is accepted for die gap range 9.5÷10 mm.



Rys. 5. The weight change of a blowing product depending on the die gap value

Table 1 illustrated measurements of the wall thickness in the areas designated by the client of final product. It is noted that these values are not met in all these places. In the case of assembly place the assurance of the wall thickness is met, the adopted set acceptable tolerance zone to the die gap set by the following values: 9.5, 10, 10.5 and 11 mm. In other analyzing points: A and B, only at the point A, we have got acceptable value. However, at the point B is a range of values beyond the upper value of the tolerance field.

Tab. 1. The range of the wall thickness in consideration point of blowing technical products

Die gap value [mm]	Thickness value in the assembly area [mm]				The wall thickness in the specific points [mm]	
	1	2	2	4	A	B
8,5	0,85	0,55	0,95	0,80	1,22	1,44
9	0,95	0,75	0,95	1,00	1,39	1,67
9,5	0,95	0,75	1,00	1,00	1,42	1,72
10	1,00	0,80	0,95	1,20	1,48	1,77
10,5	1,05	0,83	1,05	0,93	1,42	1,78
11	1,00	0,85	1,05	1,10	1,56	2,08
11,5	1,20	0,85	1,05	1,00	1,73	2,07
12	1,10	0,90	1,05	1,25	1,74	2,08
12,5	1,00	0,85	1,10	1,25	1,52	2,07
13	1,05	0,85	1,20	1,15	1,79	2,01
13,5	1,15	1,00	1,22	1,30	1,75	2,14

Taking into account the performance two criteria: product weight and value of the wall thickness, it is estimated that only case in which the value of the die gap is 9.5 and 10 mm can be considered as appropriate to the potential customer acceptance.

5. Final consideration and summary

Extrusion blow molding process enables molding technical hollow products of varying geometric complexity as a result of parison extrusion and then blow in the mold cavity. However, for the fulfillment of assumptions certain related to the assurance of a product weight and thickness distribution, it is important immense selection of appropriate technological parameters of processing, which in this case means the specified die gap value. Seen from the point of energy view, the process should be extruded parison profile VWDS system, while maintaining the value of the output die gap 9.5 mm. This means that in the present case the production material savings in the number of about 300 g for each product in relation to the setting 10. Almost total value of the material weight is contained in the technological flash. The weight difference products of to setting the die gap 9.5 mm and 10 mm is only 1 g. Also lower the overall flash weight helps to minimize the energy input on the line for recycling, during flash recycling.

From the viewpoint of giving of the new guidelines for the implementation of the extrusion blow-molding should be considered necessary to have to carry out the optimization procedure the thickness distribution in the extruded parison VWDS. Whereas that during the extrusion stretch parison follows its own weight in the area to produce at point A is in the space of tolerance, in turn, point B in due to the lack of any gravitational tension is too thick. Indication could be to attempt to reduce the range of the thickness of the extruded parison at the bottom, due to the fact that there is no practical stretched. The task significantly may be easier to use the calculation algorithm (optimization) available in the software Ansys-Polyflow often presented in some papers [5, 6]. By using this tool you can get guidelines for even greater savings in materials and energy.

Literature

- [1] Kutz M., *Applied plastics engineering handbook*, 1st ed., pp. 280 – 284, Elsevier 2011
- [2] Belcher S.L., *Practical guide to injection blow molding*, Taylor & Francis Group, 2007.
- [3] Kotecki M., Influence technological blowing parameters on quality technical product, UTP Bydgoszcz, final work 2012
- [4] Norman, C. L., *Practical guide to blow moulding*, Smithers Rapra Technology, 2006.
- [5] Pepliński, K., Bieliński, M., *Polyflow software use to optimize the parison thickness in blowing extrusion*, Journal of Polish CIMAC, 4, Gdańsk 2009.
- [6] Pepliński K., Mozer A., Ansys-Polyflow software use to select the parison diameter and its thickness distribution in blowing extrusion, Journal of Polish CIMAC, 5, Gdańsk 2010.
- [7] Pepliński, K., Bieliński, M., *Processing and functional properties of the containers prepared by blowing extrusion in variable processing conditions, and evaluation of yield and quality of the process*, Polimery, 54, nr 6, pp. 448–456, 2009.
- [8] Pepliński, K., *Select technical aspect of energy using and management in injection molding process*, Journal of Polish CIMAC, 6, Gdańsk 2011.
- [9] www.plasticseurope.org, *The Compelling Facts About Plastics 2011*, Plastics Europe, Brussels – Belgium 2012.

SELECTED ASPECTS OF VIRTUAL PROTOTYPING THE BLOWING PREFORM PROCESS IN THE ANSYS-POLYFLOW SOFTWARE

Karol Pepliński

Bydgoszcz University of Technology and Agriculture
ul. Aleja Prof. S. Kaliskiego 7, 85-789 Bydgoszcz, Poland
tel.: +48 52 3408224, fax: +48 52 3408222
e-mail: karolpep@utp.edu.pl

Abstract

Technological processes of blowing the polymer preform occupy a prominent position among the widely understood blowing technology side extrusion blow molding or direct injection blow molding. Efficient design of a structural preform for a specific final polymer product needs to give its geometric form suitable thickness distribution in the different peripheral sites under consideration of the preform and the appropriate temperature field adapted to the blow ratio and the final geometry of the product or user requirements. Often it is a time consuming task in the absence of adequate knowledge about the blowing process phenomenality in general-purpose software Ansys–Polyflow. This may result in the occurrence of different errors in the numerical calculations. In a virtual design of Polyflow environment is possible to check whether a particular geometry application specific blowing preform parameters and their impact on the final form of a product.

Keywords: *blowing preform, virtual prototyping, Ansys-Polyflow simulation, blowing abnormalities*

1. Introduction

Blow molding of polymers is one of the main processes of plastics processing. For blow molding technologies include, in particular: extrusion blow molding (EBM), injection blow molding (IBM), injection stretch blow molding (ISBM) and 3D blow molding (3DBM). Injection blow molding is the third largest share of these four technologies [1]. The products formed in the injection blow molding technology, compared to the extrusion blow molding, are formed without the technological wastes (flashes). For complete implementation of the process involves the following steps: injection a molten plastic into the mold cavity to form a parison with a given geometry, the stabilization of heat to a certain temperature blow molding processing, transfer preform to blow cavity, blowing with compressed air, cooling and eject a product of the form [2].

Nowadays, due to the increasing need to market the blowing products relating in particular to minimize material and energy requirements [8] on the unit implementation plastics process, it is necessary to take into account modern and advanced computer aided (CA) tools – computer simulations. In the present case concerns software dedicated to computer aided blowing materials such as: Polyflow, Abaqus, BlowView, Simblow, B-Sim, etc. Often, the carry out these tasks in a virtual environment requires a broad knowledge of polymer processing such as: polymer rheology, knowledge processing technology, the design principles and current realities of technological machines. However, it should be noted that thanks to advanced CA and technology tools of

machinery and equipment was possible in the past 30 years reduce bottle weight: for extrusion blowing product – average of about 100%, and the injection blow bottles with about 30% [9].

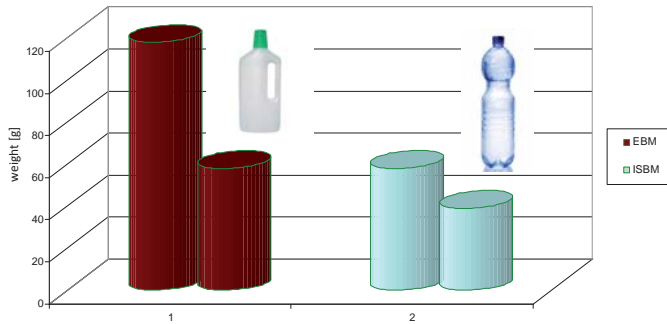


Fig. 1. Reducing the weight of the blowing product over the last thirty years, for example, bottles made in the EB and ISBM technology [9]

2. Outline of Polyflow design simulation

Outline of simulation design using CAE software to the design blowing process involves several consecutive stages. The most important and advanced step of virtual modeling and design is environment of Polydata module.

The first step necessary for the simulation is to create or import the geometry of the test piece of software CAD3D. For this purpose is using a module Design Modeler. In the realized task used in surface models without thickness attribute. Then, in the module ANSYS Meshing, applied to the model, finite element mesh and determines the characteristics and parameters. There are several possible choices in the types of networks in this module: automatic, square (Fig. 2a), triangular (Fig. 2b), mixed referred to as a square – triangle (Fig. 2c).

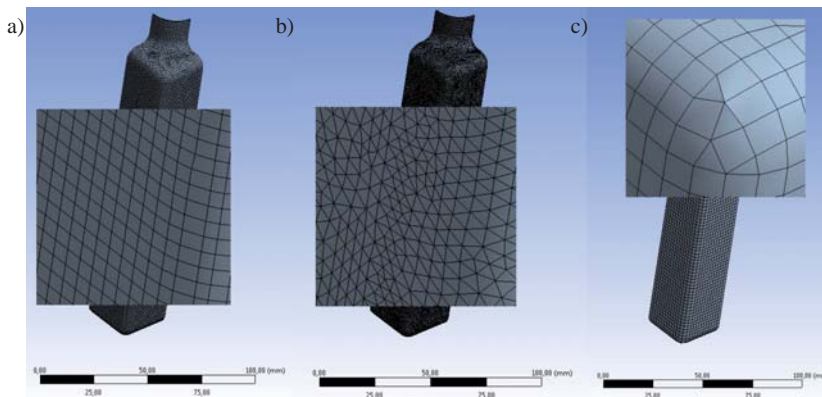


Fig. 2. Types of finite element mesh: a) square grid, b) triangular mesh, c) net mixed

Type of selected grid has a significant impact on the accuracy of reproduction the object surface during the implementation of numerical calculations for blowing preform. The basic parameters of the grid depend on its type. Typically, the accuracy of numerical calculations depends on degree of the net density. There is also the possibility to use different grids for each object (preform – mold).

Thanks to Face Sizing option can be determined various parameters of the grid for each of the

planes of a single object, which can significantly control the accuracy of the location of the grid, the appropriate density and time calculations. Another important option that is available in the ANSYS Meshing module is optional Virtual Topology. It enables connect the surface with a common edge. The operation to remove the division edge of the surface changes the distribution grid. Its use generally results in an increase in the number of finite elements used to create the grid (maximum increase in the number of finite element simulation during realizing task exceeded 40%). This option is shown in Figure 3 This module also defines the boundary conditions in the consideration issues.

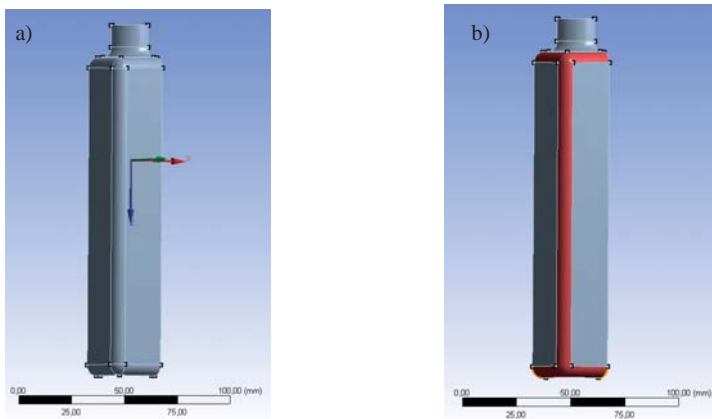


Fig. 3. Virtual Topology option: a) detail before using Virtual Topology, b) detail after use of this option

Polydata module represents the next stage of design simulation. It is introduced in the material parameters (such as: viscosity, density, heat capacity, etc.), blow-molding processing conditions (pressure and blowing time, preform temperature and wall thickness) and flow conditions (the type of flow, the type of liquid polymer used in the simulation). Introduced the parameter values associated with the same simulation, among others: its duration, the maximum number of steps. Adaptive Meshing option available in Polydata module allows inherent thickening grid in sensitive areas during the implementation of numerical calculations. Typically, the connection surfaces are arranged relative to each other at a small angle or a small radial passage. By using this option, the grid can be compacted as much as 16 times. The use of auxiliary tasks as a postprocessor allows for batch files for the next steps (simulation) optimization. The optimization can be carried out in terms of the volume of the bottle, the weight, the temperature distribution or preform distribution thickness. Following the establishment of the relationship and specific processing conditions for the object, it can proceed for numerical computations in a module Solution.

The final step is to present the results of the simulation. Visual presentation is made possible by the use of CFD Post module. The module allows you to present selected individual calculation steps in the form of color objects. Results can also be displayed as graphs. This module allows the simultaneous presentation of the results of different parameters.

3. Selected errors in the design and implementation of simulation

Simulations of improper conduct are a significant problem in the design of polymer processing and associated with relatively large waste of time, even last twice as long as simulations programmed in the right way. It should be noted, however, that the wrong course of simulation calculations can be seen even after a small number of steps, others become apparent only after several steps. It is worth mentioning that during the complex process of optimization problems

blowing and difficult to predict outcomes, it is not easy to choose the right strategy in dealing with the simulations carried out. One way to quickly selecting the mistake is to monitor the simulation, but this requires the user to sacrifice a significant amount of time during several hours of calculations.

The most common mistakes made by users include incorrectly described the boundary conditions (Fig. 4), incorrectly selected processing parameters such as the range of process temperature, the blowing pressure setpoint value and the incorrectly chosen finite element mesh. Sample preform geometry with inadequately described boundary conditions, it is not blown only gradually flattened and deformed into one of the walls. The breakthroughs around sharp corners of the mold (Fig. 4d) are formed in the absence of sufficient quantities of material. The wall thickness is determined by the program as a negative.

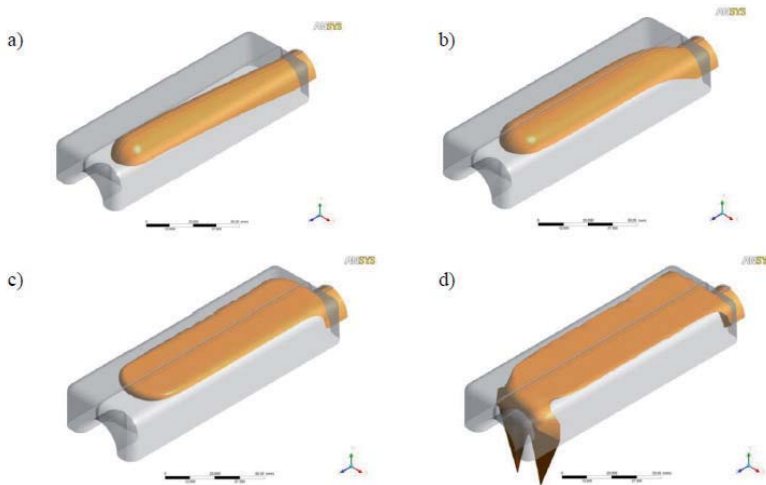


Fig. 4. Errors associated with the inappropriate selection of the boundary conditions: a), b), c), d) - improperly running blow process stages

If you specify the wrong temperature range processing in conjunction with preform thickness occurs of irregularities blow the wall. Area with the lowest temperature of 91°C (Figure 5, indicated by the field - blue) is simultaneously the zone with significantly increased wall thickness, thickening is more than six times as compared to the zone at a temperature of 120°C. Thickening and the much lower temperature caused a much slower blowing (stretching) of the area, resulting in each other superposition and penetration of the two layers of the stretched material, and an error simulation (Fig. 5).

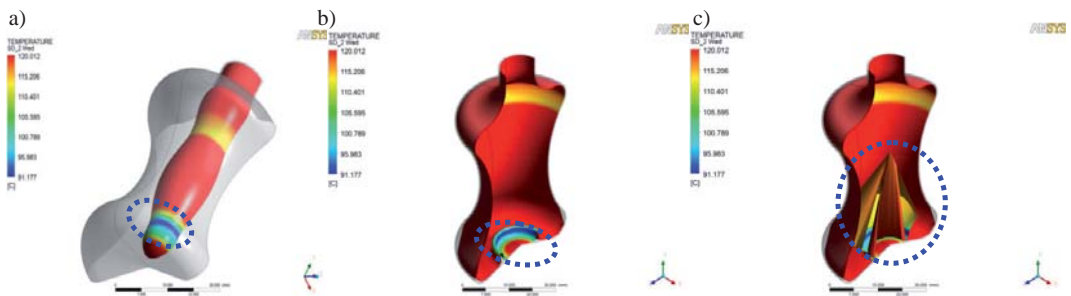


Fig. 5. Improperly selected interval processing temperature range blowing preform: a) preform during the initial blowing to the area of reduced temperature, b) the beginning of the visible improper preform blowing, c) the penetration of thin layers of material in the border area of low and high temperature fields

4. Summary

Virtual prototyping of blowing preform process often requires an amendment at the stage of the finite element mesh or modifying certain boundary conditions, material properties or conditions associated with the process window of blow molding processing: temperature, pressure, etc. Also, as soon as possible in order to identify design errors and accuracy of the simulation running should monitor the course of the calculations in the module CFD Post, and not only upon completion of the calculation. Many other correct blowing simulation results are presented in previous publications [3-8]. It should be noted that despite the difficulties during the implementation of virtual prototyping blowing process, should use this tool because of the opportunity to test a specific geometry or application specific blowing preform parameters and their impact on the final form of a product beyond the typical industrial conditions.

Literature

- [1] Kutz M., *Applied plastics engineering handbook*, 1st ed., pp. 280 – 284, Elsevier 2011
- [2] Belcher S.L., *Practical guide to injection blow molding*, Taylor & Francis Group, 2007.
- [3] Pepliński K., Mozer A., *Ansys Polyflow software use to optimize the sheet thickness distribution in thermoforming process*, Journal of Polish CIMAC, 6, Gdańsk 2011.
- [4] Pepliński K., Mozer A., *Design of extrusion die for plastic profile using Ansys Polyflow software*, Journal of Polish CIMAC, 6, Gdańsk 2011.
- [5] Pepliński, K., Bieliński, M., *Polyflow software use to optimize the parison thickness in blowing extrusion*, Journal of Polish CIMAC, 4, Gdańsk 2009.
- [6] Pepliński K., Mozer A., *Ansys-Polyflow software use to select the parison diameter and its thickness distribution in blowing extrusion*, Journal of Polish CIMAC, 5, Gdańsk 2010.
- [7] Pepliński, K., Bieliński, M., *Processing and functional properties of the containers prepared by blowing extrusion in variable processing conditions, and evaluation of yield and quality of the process*, Polimery, 54, nr 6, pp. 448–456, 2009.
- [8] Pepliński, K., *Select technical aspect of energy using and management in injection molding process*, Journal of Polish CIMAC, 6, Gdańsk 2011.
- [9] Metwall H., *Virtual prototyping for the blow molding industry*, Ansys U.S.A. 2012.



RESEARCH ON ELASTIC-DAMPING PROPERTIES OF UNIT LOADS

Tomasz Piątkowski

*University of Technology and Life Sciences
ul. Prof. S. Kaliskiego 7, 85-789 Bydgoszcz, Poland
tel.: +48 52 3408145
e-mail: topiat@utp.edu.pl*

Abstract

In the paper, the results of tests of free-fall of unit load (cubicoidal package) from a height on the stiff ground are presented. The aim of this study is to determine the elastic-damping properties of packaging for all surfaces, edges and corners. These tests allow us to evaluate the protective ability of packages in case of impact in any direction - typical for real transport systems. The maximum accelerations registered during experimental tests are subjected to approximation by means of B-spline surface. It enables the visual interpretation of data in three-dimensional space, allowing detection critical packaging places for the safety of transported goods. In addition, the registered acceleration waveforms were used to determine the coefficients of: restitution, damping and rigidity. These parameters are required to the analytical descriptions of loads contact with obstacles - such as in the models of sorting or positioning processes of packagings.

Keywords: *free fall test, impact, damping coefficient, restitution coefficient, rigidity coefficient*

1. Introduction

Products sent from the manufacturer to the customer are closed in the protective packaging (unit loads) to improve their transport susceptibilities. The unit loads during transport and storage are subject to handling operations (such as loading, unloading, download, positioning, sorting) which pose a risk of mechanical damage of packaging and their content. To the most serious causes of security breaches of unit loads is mechanical exposure of a impact character caused by fall of unit loads on ground, on other unit loads or caused by impact when entering into contact with manipulators performing e.g., the sorting process of unit loads transported on conveyors [14], [15].

Available scientific papers dealing with the study of unit loads in the range of mechanical interactions of impact character relate to the analysis of influence of dynamic overloads on packaging damage. Not many works take an attempt to use, in this application, the finite element method [13]. The basic technique for assessing the mitigation effectiveness of overloads caused by impact is experimental test. One of the main methods for evaluation of the protective ability of packaging prototypes is test of free fall from a height (drop test). The plan of drop test realisation is based on the guidelines of standards, e.g. [10], [11], [4], [3]. This test consist in fall of the load from assumed height on the smooth and stiff ground, respectively oriented surfaces, edges and corners. The visual inspection of the packaging and its content form the basis for assessing the protective packaging properties. The content damage of loads, that cause the lack of recipient acceptance, is connected with the need of introduction of structural changes in the packaging or in the product also.

Standards relating to the method of free fall concern only the experimental tests of unit loads [2], [1]. They do not describe any method for determining the parameters that could be used in mathematical models of process of sorting or positioning of load streams [14], [15].

In the present work it was assumed that the method of the free-fall (included in the standards) will be a reference to determine the coefficient of restitution, stiffness and damping of loads. An extension of this method involves in replacing the unit load content with substitute material and use of triaxial acceleration recorder mounted inside the package. Acceleration waveforms (recorded by the sensor) are the base to determine the change velocity and impact duration. Further, these values (assuming knowledge of the free fall height) allow specifying the restitution, stiffness and damping coefficients of loads for each individual directions of impact.

2. Program of experimental tests of impact phenomenon

To record the impact process (during the tests of free fall of unit load on stiff ground) the triaxial acceleration recorder type 3L30 SAVER made by Lansmont (placed inside the package) was used. The device can save 100 waveforms of accelerations not exceeding the maximum value of $\pm 100G$ (1G - gravity acceleration). It is an autonomous recording system made in the form of aluminium cube of size 0,076 x 0, 076x0, 04 m and weight 0.4 kg.

For testing it was prepared cuboidal unit load of dimensions 0,136 x 0, 136x0,1 m and a total mass 0.5 kg. This load consists of a package made of a three-layer corrugated cardboard, filled with polystyrene foam (EPS). The packaging material (fulfilling anti-shock role in the load) has a thickness of 0.03 m.

The load with built in sensor was subjected to series of tests of free fall from the height of $h=0.30$ m on the rigid ground. This height is equivalent to the dynamic interactions of impact character, on which is exposed about 20% of loads in the whole transport process (from the supplier to the end user) [7]. During tests, the load was positioned manually. The falls were so planned to hit the object four times on each corner, edge and surface. In addition, the centre of mass gravity of the load was placed on a normal of collision. Thus the potential energy of gravity was maximally dissipated by the springy-damping forces of the impact process, and in the minimally manner - was converted into kinetic energy of the load rotation.

3. The experimental results and numerical analysis

Fig. 1 shows results of free-fall tests of the unit load from a height of $h=0.3$ m (acceleration - Fig. 1a and the impact duration - Fig. 1b). In the graphs are placed lines representing the average values of measurements (lines marked by reference 1) and limits of confidence interval around the average value, with 95% confidence level (lines marked by references 2 and 3). In addition, for each graph was determined coefficient of trials which were registered outside the confidence interval:

$$\delta = \frac{n_p}{n} 100\% \quad (1)$$

where:

- n_p – number of trials, the results of which go beyond the confidence interval around the average value, with 95% confidence level,
- n – the total number of trials.

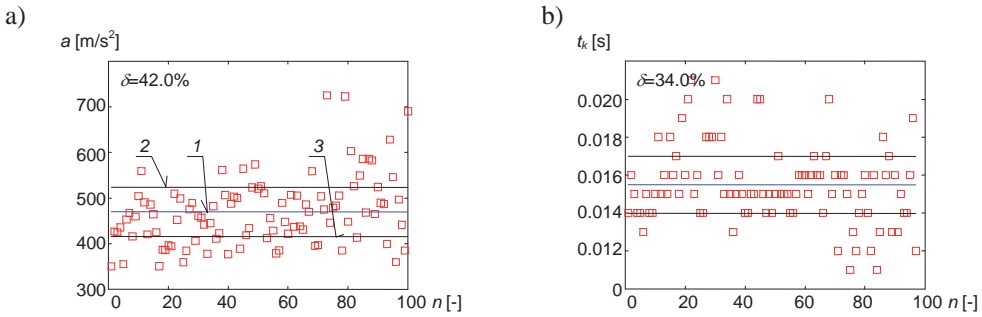


Fig. 1. Data registered during impact tests: a) maximum acceleration, b) the impact duration; 1 - average value, 2, 3 – limits of confidence interval around the average value, with 95% confidence level, δ - rate of test results registered outside the confidence interval

Presented data show a wide variation of results, confirming their strong dependence on the impact direction.

In order to capture the relationship between the direction of impact and registered accelerations the approximation by means of B-spline surface was applied - Fig. 2, [12], [5], [19], [17]. From the analysis of presented graphs show, that in case of the fall of the load on the edges and corners, the dissipation ability of impact energy of the package is greater than the fall on the walls.

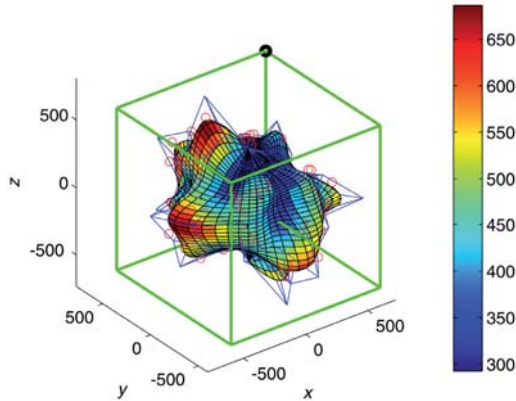


Fig. 2. Result of approximation (in isometric projection) of the of load accelerations registered during free fall from height $h=0.3$ m [17]

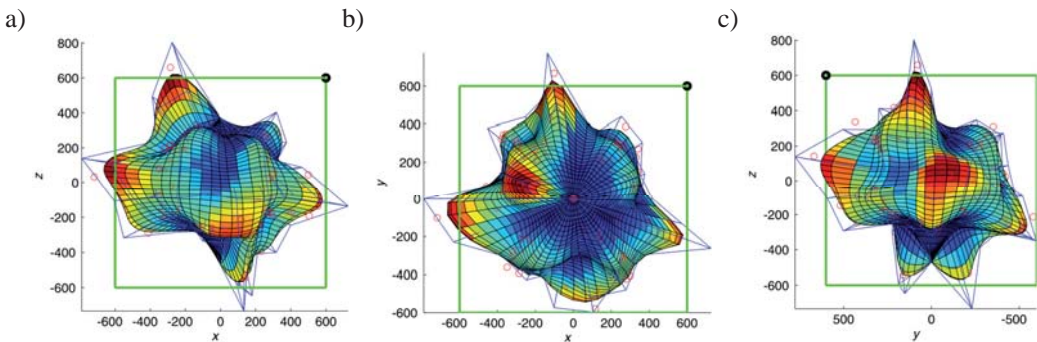


Fig. 3. Orthogonal projection of chart from Fig. 2: a) in the xz plane (main view), b) in the xy plane (top view), c) in the yz plane (left-side view) [17]

3.1. The method of the restitution coefficient determination

On the basis of data obtained (Fig. 4a) during tests of the load free-fall, directly can be determined shapes of acceleration waveform, their extreme values, the extremes' positions, the impact duration. Moreover, in an indirect way also can be determined additional information: the velocity change Δv and coefficient of restitution e .

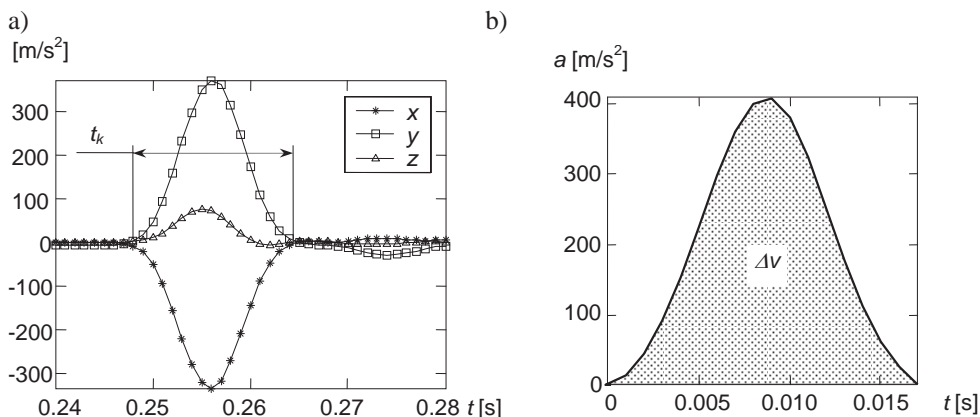


Fig. 4. Example of acceleration waveforms recorded during impact: a) "raw" acceleration waveforms, b) "cut out" acceleration course corresponding to the time of contact between the load and stiff ground; a_x , a_y , a_z – components and resultant of acceleration, t_k – time of impact duration

The velocity change Δv of the unit load during impact is determined by single integration of acceleration.

$$\Delta v = \int_0^{t_k} a dt \quad (2)$$

where:

t_k – the impact duration.

The velocity change Δv is the area contained between the acceleration curve and the abscissa t - Fig. 4b. The time of impact t_k is treated as duration of the compression forces occurring between the load and the ground. These forces appearance corresponds to the moment of impact initiation, and their disappearance - to the impact end.

The unit load velocity (achieved during free fall tests) just before contact with the stiff ground is determined on the basis of conservation principle of the potential and kinetic energy, and the knowledge of the free fall height h_0 :

$$v_0 = -\sqrt{2gh_0} \quad (3)$$

where:

g – gravity acceleration.

The velocity achieved by the unit load just after impact (at the moment t_k , Fig. 4a) is defined by equation:

$$v_k = \Delta v - v_0 \quad (4)$$

Knowing the load velocity just before and after impact, the kinematic coefficient of restitution (the Newton's coefficient of restitution - Fig. 5) can be determined:

$$e = -\frac{v_k}{v_0} \quad (5)$$

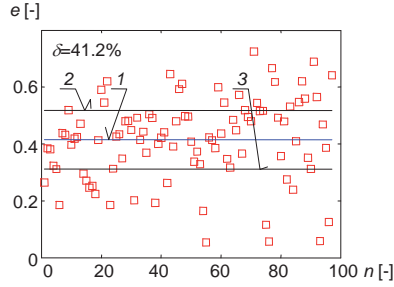


Fig. 5. Restitution coefficient; 1 - average value, 2, 3 – limits of confidence interval around the average value, with 95% confidence level, δ - rate of test results registered outside the confidence interval

3.2. The method of coefficients determination of the rigidity and damping

Coefficient of restitution is required in so-called discrete (classical) impact models (based on Newton's model), in which the impact is treated as an instantaneous (timeless) process - lasting in an infinitely short time. These models allow determining the motion parameters of bodies just before and after collision. However, they are not able to determine the impact reaction forces, nor accelerations and deformations of colliding bodies. To determine these quantities it is necessary to use the continuous impact models, to which belongs local strain model - based on Hertz's theory of contact problems [20], [9], [21]. An example of this class of models is a modified nonlinear Kelvin model (proposed by authors of the work, Fig. 6 [16]):

$$N = b_I m_p^{0.4} \dot{D} D^2 + k_I D^4 \quad (6)$$

where:

- b_I – damping coefficient,
- k_I – rigidity coefficient,
- m_p – mass of the unit load,
- D, \dot{D} – strain and strain velocity, respectively, of colliding bodies.

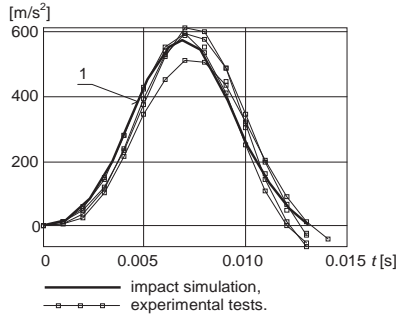


Fig. 6. Chart of impact simulation (curve marked by reference 1) and acceleration courses, registered during experimental tests [16]

The main input parameters of the impact model (equation (6)) are the coefficients of: rigidity k_I and damping b_I . These coefficients can be obtained on the basis of numerical solution of the system of equations:

$$\begin{cases} \hat{e}(b_I, k_I) - e = 0 \\ \hat{t}_k(b_I, k_I) - t_k = 0 \end{cases} \quad (7)$$

where:

$\hat{e}(b_1, k_1), \hat{t}_k(b_1, k_1)$ – restitution coefficient and time of impact, respectively, determined during simulation of impact model (6),

e, t_k – the values of restitution coefficient and time of impact duration determined on the basis of free-fall tests of load dropped from the height.

The results of calculations of damping and restitution coefficients are shown in Fig. 7. A surprising effect is the number of data located in the confidence interval - higher compared to data presented in Fig. 1 and Fig. 5.

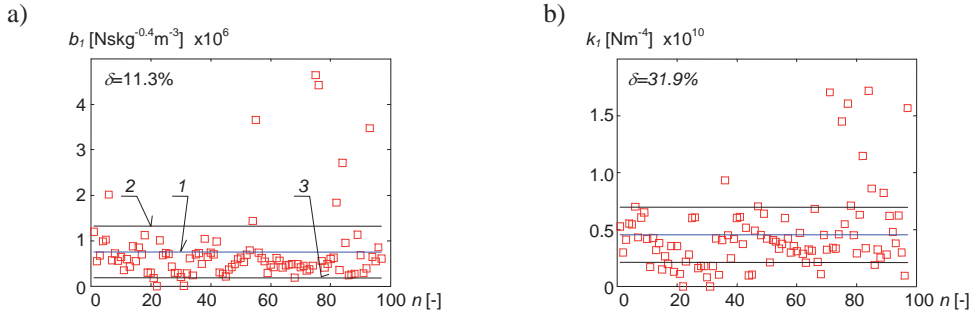


Fig. 7. Springy-damping properties of unit load: a) damping coefficient, b) rigidity coefficient; 1 - average value, 2, 3 – limits of confidence interval around the average value, with 95% confidence level, δ - rate of test results registered outside the confidence inter

4. Summary

The following concluding remarks were formulated:

- The drop tests of unit loads designed to the experimental verification of packaging prototypes can also be used to determine the parameters required in models of the impact phenomenon: coefficient of restitution, damping and stiffness of the package (in any direction of impact).
- To describe the impact phenomenon (and calculate the springy-damping properties of packaging) a modified nonlinear Kelvin model can be used. This model effectively reproduces impact course registered during tests - in relation to the unit load considered in the paper.
- Approximation of test results of a free-fall with the use of B-spline surface allows intuitive identification of places (in the package in three dimensions) that are critical for the safety of the content of load and require changes in its design and construction.

References

- [1] ASTM D1596 – 97(2003), *Standard test method for dynamic shock cushioning characteristics of packaging material*.
- [2] ASTM D3332 – 99(2010), *Standard test methods for mechanical-shock fragility of products, using shock machines*.
- [3] ASTM D4169 – 09, *Standard practice for performance testing of shipping containers and systems*.
- [4] ASTM D5276 – 98(2009), *Standard test method for drop test of loaded containers by free fall*.
- [5] Foley, J.D., *Introduction to Computer Graphics*, WNT, Warsaw 2001.
- [6] Gryboś R., *The theory of impact in discrete mechanical systems*, PWN, Warsaw 1969.

- [7] Herbert H., Schueneman H., *Packaging engineering, design and testing. A step-by-step approach for protection of fragile products*, Westpak Inc., San Jose (USA), www.westpak.com (accessed 2012-04-14).
- [8] Huang H., Dallimore M.P., Pan J., McCormick P.G., *An investigation of the effect of powder on the impact characteristics between a ball and a plate using free falling experiments*, Materials Science & Engineering, 1998, 241, 38-47.
- [9] Huang H., Dallimore M.P., Pan J., McCormick P.G., *An investigation of the effect of powder on the impact characteristics between a ball and a plate using free falling experiments*, Materials Science & Engineering, 1998, 241, 38-47.
- [10] ISO 2248:1985, *Packaging – Complete, filled transport packages – Vertical impact test by dropping*.
- [11] ISO 4180:2009, *Packaging – Complete, filled transport packages – General rules for the compilation of performance test schedules*.
- [12] Kiciak, P., *Basis of curves and surfaces modelling*. Applications in computer graphics, WNT, Warsaw, 2005.
- [13] Low K.H., *Drop-impact cushioning effect of electronics products formed by plates*, Advances in Engineering Software, 2003, 34, 31-50.
- [14] Piatkowski T., *Active fence with flexible link*, Journal of Theoretical and Applied Mechanics, 2010, 48(6), 87-109.
- [15] Piatkowski T., Sempruch J., *Model of the process of load unit stream sorting by means of flexible active fence*, Mechanism and Machine Theory, 2008, 43(5), 549-564.
- [16] Piątkowski T., Sempruch J., *Model of inelastic impact of unit loads*. Packaging Technology and Science, 2009, 22(1), 39-51.
- [17] Piątkowski T., Sempruch J., Tomaszewski T., *Spatial approximation of impact test results of unit load*. Journal of POLISH CIMAC, 2012, 3 (7), 243-251.
- [18] Rajalingham C., Rakheja S., *Analysis of impact force variation during collision of two bodies using a single-degree-of-freedom system model.*, Journal of Sound and Vibration, 2000, 229(4), 823-835.
- [19] Shene, C. K., *De Boor's algorithm*, <http://www.cs.mtu.edu/~shene/COURSES/cs3621/NOTES/spline/de-Boor.html> (accessed 2012-04-14).
- [20] Thornton C., *Coefficient of restitution for collinear collisions of elastic-perfectly plastic spheres*, ASME Journal of Applied Mechanics, 1997, 64, 383-386.
- [21] Zhang D., Whiten W. J., *The calculation of contact forces between particles using spring and damping models*, Powder technology, 1996, 5, 59-64.

THE PROBLEM OF ASSESSMENT OF INITIAL POINT OF CRACK DEVELOPMENT IN IMPACT BENDING TEST

Jan Sadowski

*University of Technology and Life Sciences
Faculty of Mechanical Engineering
7 Kaliskiego Street, 85-791 Bydgoszcz, Poland
e-mail: sadjan@utp.edu.pl*

Abstract

The problem of assessment of the initial point of a crack in in static tests is already recognizable and simple to determine. On the basis of this point the force F_p and energy E_p necessary to initialize fracture, thus due to these parameters it is possible to determine parameters of crack resistance. In case of dynamic loads, especially during the impact bending test of material samples, this problem is much more difficult and at the present level of science it is still current matter. In the article, in compliance with own research, the comparison of different methods of initial point determination in bend-test was performed, which is: compliance change of the sample, strain gauge tests (tensometric), mathematical processing of registered actions $F(t)$, method of maximum force F_{max} with the most accurate method (pattern method): crack alteration, for tested steels 18G2A and St3S and aluminium alloy Ak12, in order to demonstrate essential differences in assessment of initial point of crack in impact bending test.

1. Introduction

The recognition of physical phenomena happening during the test of dynamic bending in tested samples, mainly for determination of force initializing cracking F_p , and energy necessary to initialize cracking E_p , at this level is still subject to research. Precise denotation of cracking initial point enables for correct calculation of parameters of dynamic crack resistance such as:

- dynamic critical ratio of tension intensity K_{Id} [6, 7, 14]

$$K_{Id} = \frac{F_p \cdot S}{B \cdot W^{3/2}} \cdot f(a/w), \quad (1)$$

where:

F_p - force subtending a beginning of crack initialization, N

S - distance between props, mm

B - thickness of tested sample, mm

W - Width of sample, mm

a - length of fracture in sample, mm

$f(a/w)$ - function of interspace shape in a sample.

- dynamic integral J_{Id} [6, 7, 14]:

$$J_{Id} = \frac{2E_p}{B(W-a)}, \quad (2)$$

where:

E_p - energy subtending initialization of crack, J

B - thickness of sample, mm

W - width of sample, mm

a - distance of interspace in sample, mm.

Pursuant to calculated parameters it is possible to assess other measurements such as: critical dynamic extension of crack – CODR, dynamic module of tearing of tested sample T_{mat} or critical size of defect a_d , in conditions of dynamic loads. Determined parameters are very important machining constants applied in engineering calculations of constructions working with impact loads.

Although determination of force (energy) initializing the beginning of material crack in conditions of static load is generally simple and obvious [1], in case of dynamic loads it is a problem, especially for ductile materials - as a result new methods of testing should be invented.

Recently, numerous different approaches are observed about the problem of assessment of initial crack point in condition of dynamic loads. This fact encouraged the author of the article to present the current level of knowledge on the topic and to share his own test results.

According to the suggestion of ruling ASTM norms [2], SEP1315[3] or ISO14556[4] and ESIS[5], the point of beginning of crack initiation is the point of maximum force F_m , determined on the basis of the diagram force-displacement, obtained from dynamic bending test.

Other authors of works [6,7] point out that this can be force located almost in the middle between dynamic force on yield limit F_{gy} and maximum force F_m .

Authors of publications [8,9], on the basis of mathematical processing of removed patterns $P = f(f)$ or $P = f(t)$ in test of impact bending, by usage of program FRACDYNA[9], assessed the initial point of crack, applying static processing of registered patterns by methods: differentiation, approximation, panning and joining of obtained high-frequency patterns.

On the contrary, the authors of research [10,11] in order to determine the point of crack initialization, they applied a wavelet analysis of magnetic signal, obtained from sensors situated on the beater of the impact drill. They showed its accuracy in contrast to the testing method of compliance change of bended sample (CCRM) and method of maximum force F_m .

In publications [12,13] authors applied the method of magnetic emission (ME) to determine the point of crack initiation and testing with application of strain gauge. (PD).

Authors of publications [14,15] used the method suggested by T. Tseng and T. Kobayasi, which is the method of compliance change of a sample [6,7] the assessments of crack initial point.

Described methods at the current level of science are very accurate but they require very sophisticated equipment and complex test methodology as well as advanced software in order to process patterns removed during impact test.

The exception may be the method of compliance change of the sample (CCRM), which is not time-consuming and a result can be obtained from one sample.

Described controversies of presented methods probably discourage the authors publishing standard norms, which would be the ruling norms in the future to assess mentioned parameters of dynamic crack resistance.

2. Own experiments

The author of this publication decided to commence comparison testing of the assessment of crack initiation point in selected materials: steels 18G2A and St3S as well as the alloy of aluminium AK12, applying different testing techniques. Very accurate method was used and accepted as a pattern method: alteration of crack and strain gauge measurement method, both of

them were then compared to other methods: change of compliance of a sample, diagram static proceeding and method of maximum force.

The tests were performed on equipped impact hammer Psd300 with application of FRACDYNA [9] to formulate the results.

Fig. 1 presents methods of proceedings in assessment of cracking initial point, for evaluation of force F_p initializing cracking by multi-sample method (crack alteration), admitted as a pattern method for tested materials.

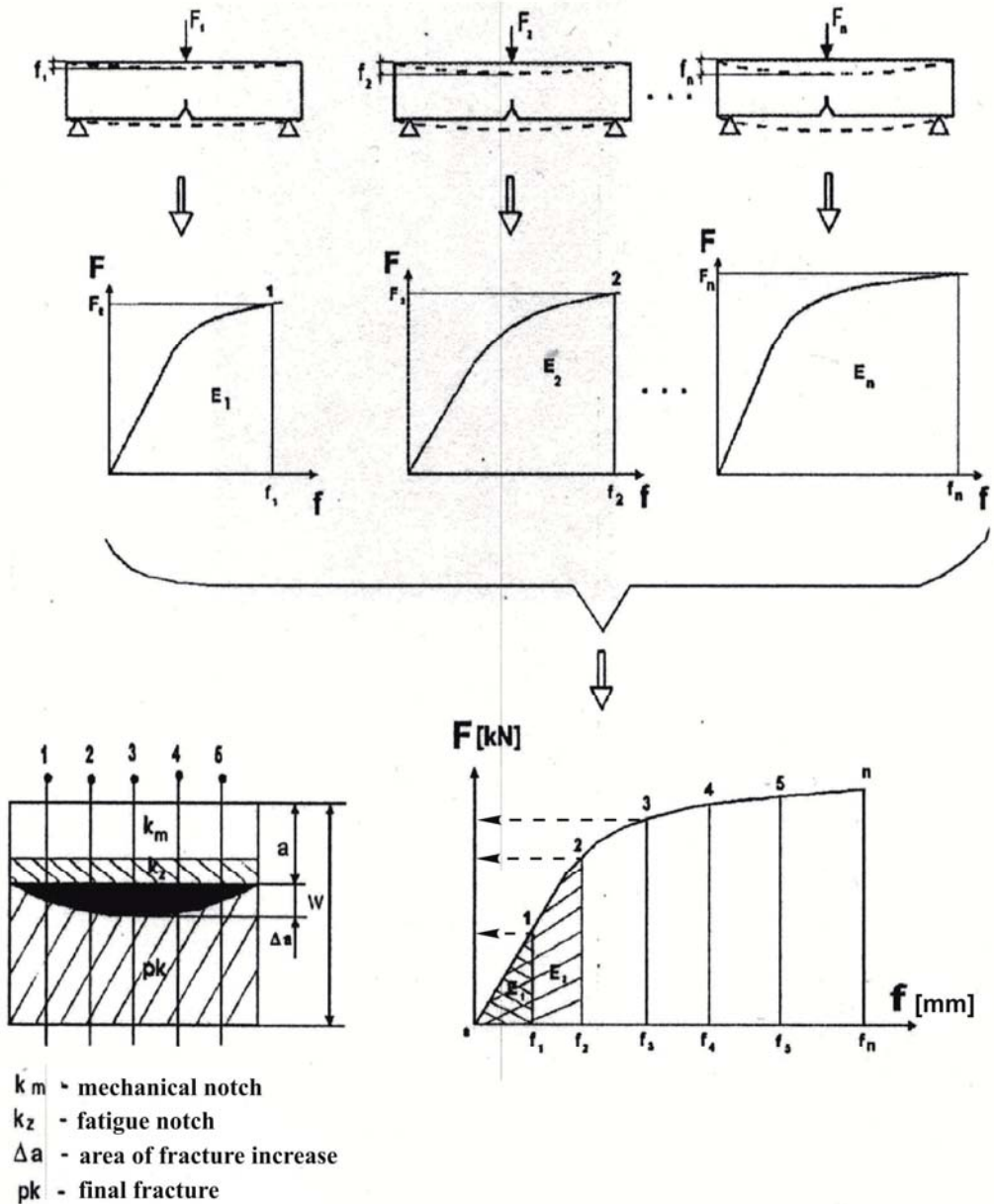


Fig. 1. Methodology of determination of cracking initiation point (force initializing cracking F_p) by method of crack alteration

For each of tested materials 10-15 impact samples were used, each with implemented endurance fracture with equal $a/W = 0,45-0,55$ [2].

According to fig. 1, increasing impact force F was causing stable increase of fracture by Δa in tested samples. In aim to obtain different values in fracture increase Δa with different load force, the instrument limiting knife movement of the pendulum was installed at the base of impact hammer. The scheme of this instrument is shown in the fig. 2.

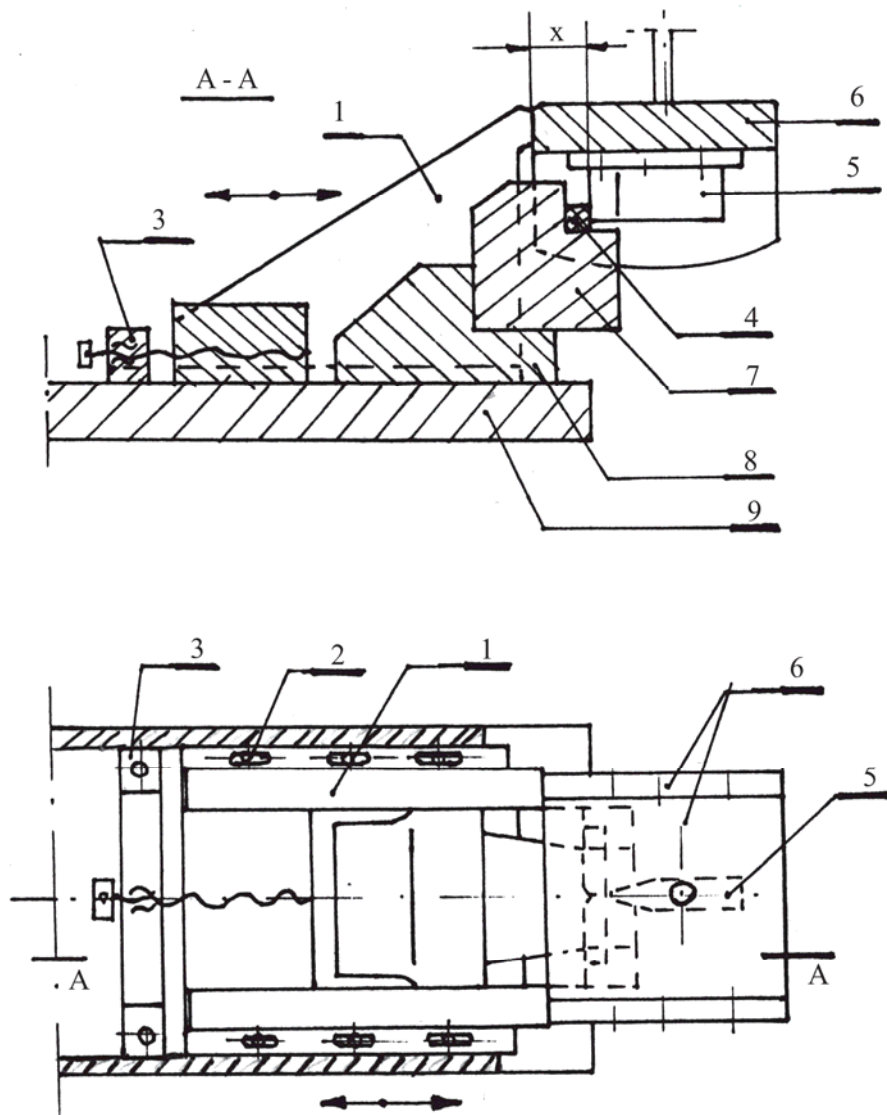


Fig. 2. The instrument limiting the impact force of the pendulum knife of a impact hammer: 1 – mobile resistance platform, 2- platform block, 3 – support pole with micrometer screw, 4 – tested sample, 5 – pendulum knife of impact hammer, 6 – integument of knife, 7 – support coil, integument of support coil, 9 – base of impact hammer

This machine due to function of regulation of the distances X of resistance surfaces of mobile platform from the impact surface of the pendulum knife enabled obtaining different values of fracture increase Δa of tested samples and completely disabled the destruction of the sample (crack alteration).

During each test the steps of load $F(t)$ were recorded on impact hammer as well as the progress of displacement $f(t)$ in the time function. An example of such diagram for alloy of aluminium AK12 is shown in the fig. 3.

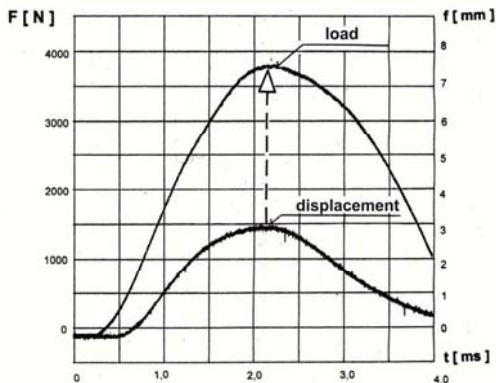


Fig. 3. Example diagram of load F and displacement f in time function t for AK12 alloy

Obtained diagrams were further transformed into investigation of function $F(f)$, which enabled to calculate the energy used by particular samples loaded with different forces.

In order to identify the extension of increasing crack Δa in case of each force, the samples were subject to oxidation in temperature 350°C for 15 minutes in laboratory furnace, then they were cooled and further cracked on impact hammer. On the surfaces of a crack the fracture increase area Δa painted with blue color was measured, easily recognizable in comparison with inserted endurance crack. Measures was taken from 5 points (fig. 1 on the left side), located along the forehead of endurance crack. Thus, value Δa from one sample was treated as an arithmetic average for particular measurements on the surface of crack increase area. By this method it was possible to exactly assess the force F_p initializing cracking and count corresponding energy E_p , which referred to the lowest of obtained crack increases Δa (the beginning of of crack). As an example in the fig. 4a there were shown photographs of sample fracture surfaces after dynamic load with different crack increases Δa for the steel 18G2A.

In the fig. 4b the forces while altered cracks, implemented to the diagram of impact bending of this steel, referring to tested samples from N1 to N6, and the force initializing crack F_p was referred to N1.

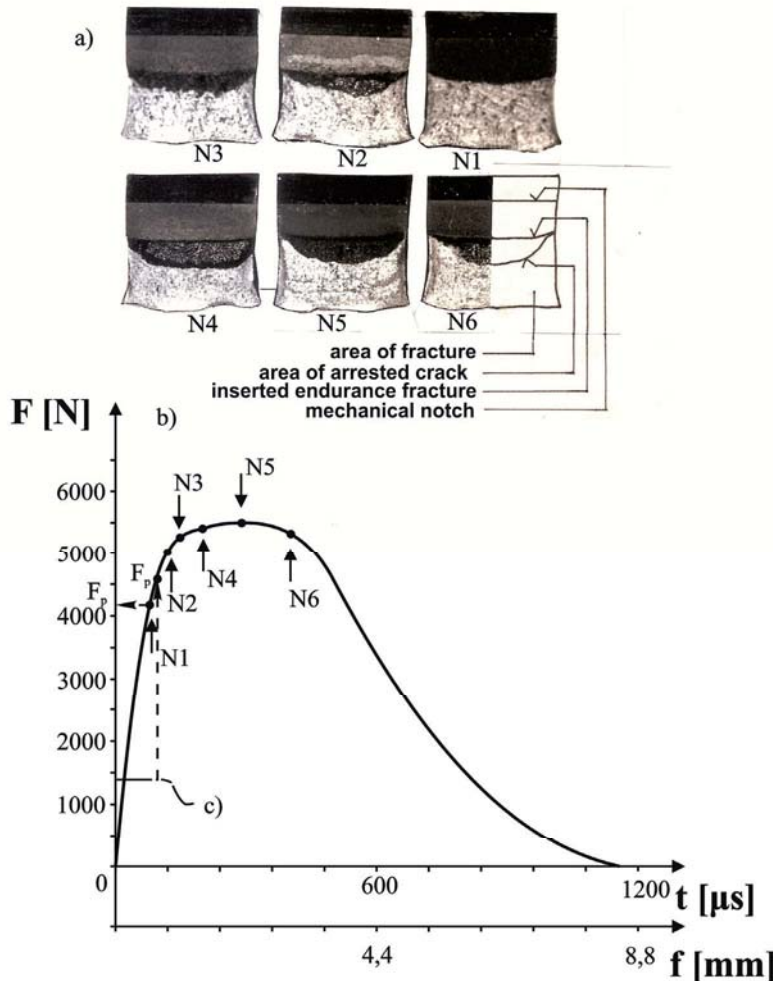


Fig. 4. Photographies of sample fracture surfaces after dynamic load with different crack increases, obtained by the multi-sample method of tested steel 18G2A (a), points referring to particular crack increases for these samples, inserted on the diagram of dynamic destruction of this steel (b), recorded sign after peeling tensometric sensor out, determining force F_p in strain gauge test (c)

In the pictures visible are: area of altered fracture increase Δa , of inserted endurance fracture, area of mechanical notch and fracture of tested samples.

Determination of crack initiation point by tensometric tests is done by tensometer strips on the end of a crack of inserted endurance fracture. The tensometers strips LY58 by Hottinger Baldwin Messtechnik were used, which were further connected in parallel to the force sensor and the sensor of displacement of impact hammer. This method enabled for record of the moment of crack of a sample. Due to this result the force corresponding with the moment of sensor destruction could be determined. The point describing this moment was accepted as the beginning of crack determining the force initializing the cracking F_p . It was demonstrated on fig. 4c regarding the steel 18G2A.

The method of assessment of the beginning of crack by a method of compliance change $\Delta C/C$ was performed in the following way: The dependence on the recorded deviation $F(f)$ was described:

$$\Delta C / C = (C - C_e) / C_e, \quad (3)$$

where:

$\Delta C / C$ – relative compliance change

C – compliance determined along the deviation $F(f)$, $C = \frac{f}{F}$

C_e – elastic compliance described for linear-elastic part of a deviation $F(f)$, $C_e = \frac{f_e}{F_e}$.

On the basis of the analysis of the curve $\Delta C / C$ shape with substantial change of its position while cracking, the point of crack initiation was determined, then due to this point the force F_p and energy E_p (standing for the start of crack) were determined. The scheme of this method is presented below on the fig. 5.

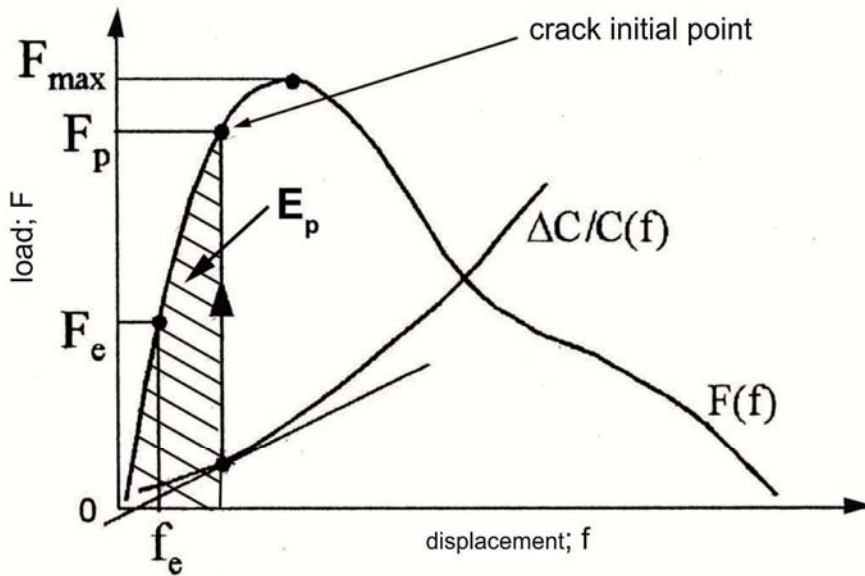


Fig. 5. Scheme of determination of crack initial point by method of compliance change of a sample

The designation of the crack initial point with methods of mathematical processing of recorded deviations during the test of impact bending $F(f)$ or $F(t)$ was performed using already mentioned program FRACDYNA [9], especially the modules 1, 2, 3 and 4 (fig. 6) were applied, with accordance to [8, 9], which enabled to outline the point of initiation of crack and the force initializing crack F_p on the basis of the mathematical analysis.

The force initializing crack in the method of maximum force was applied that F_p is the force F_{max} which is obtained on the recorded deviation by tested sample (point 6, fig. 7).

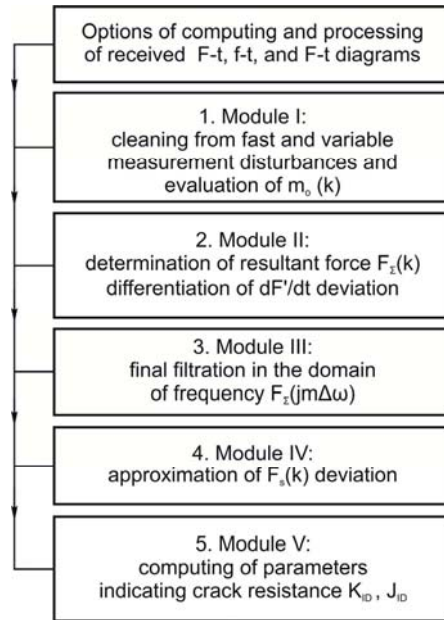


Fig. 6. Adjusted calculation options for determination of crack initial point by mathematical methods of recorded actions $F(f)$ and $F(t)$ by program FRACDYNA

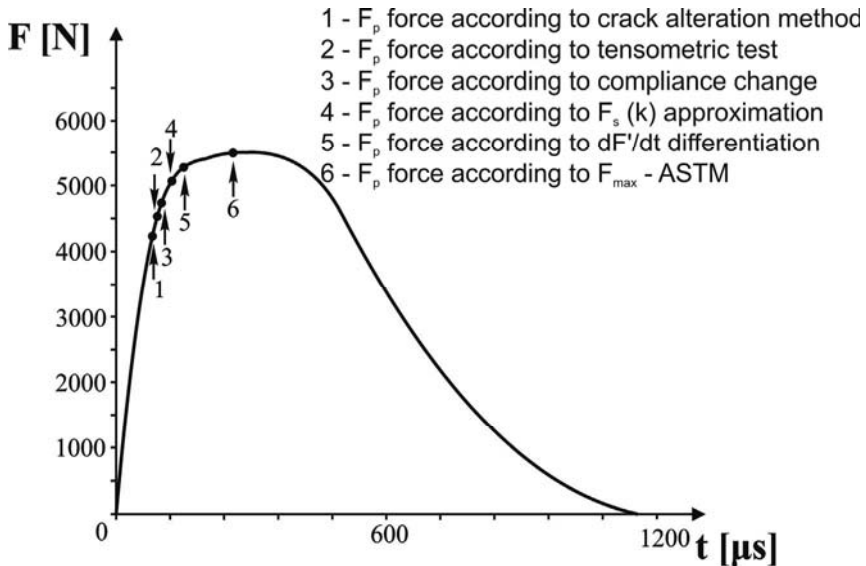


Fig. 7. Assessment of the force point of initial crack F_p by various methods for tested steel 18G2A

On the image 7 the diagram load-to-time was presented for the tested steel 18G2A (averaged for $M=61$ steps), on which the points of initial crack obtained by various methods were inserted and in the table 1 the specific values of F_p were included, concerning different methods of proceeding.

Tab. 1. Value of forces of crack initiation start point F_p in [N], obtained by various methods for tested materials

Tested material	Test method					
	Crack alteration (1)	Tensom. test (2)	Compliance modification (3)	Deviation approximate (4)	Differentiation of deviation (5)	Forces F maximum (6)
18G2A	4276	4512	4685	5102	5269	5389
St3S	3144	3215	3412	3808	3941	4272
AK12	2953	2814	3009	3425	3667	3794

Table 2 presents percentage differences of modifications of particular methods in comparison with accurate methods: pattern method (1) and tensometric tests (2).

Tab. 2. The differences in percentage modifications in particular methods of determining the crack initial point of tested materials (designation of methods as in table 1 and image 1)

Tested material	Percentage differences [%]								
	(1)/(2)	(1)/(3)	(1)/(4)	(1)/(5)	(1)/(6)	(2)/(3)	(2)/(4)	(2)/(5)	(2)/(6)
18G2A	5.52	9.56	19.32	23.22	26.91	2.44	13.08	16.78	19.44
St3S	2.26	8.52	21.12	25.35	35.88	6.13	18.45	22.58	32.88
AK12	-4.71	1.91	15.98	24.18	28.38	6.92	21.71	30.31	34.71

Pursuant to presented results it can be stated that taking into consideration the most accurate testing method which is the method of crack alteration (many samples) and method of tensometric measurements, the method of compliance modification for force initializing crack F_p assessment is the closest to described methods. The differences are minimal and they estimate 8-10%, which weighs in favour of method of compliance modification as the most accurate way in comparison with pattern method (alteration of crack).

3. Conclusion

With support of obtained results of tests it can be implied on current level of knowledge, that in further discussions and changes of norms, the method of compliance modification of impact bended sample should act officially as a pattern method (primary) to determine the point of crack initiation and assessment the dynamic parameters of resistance for crack, especially for materials ductile and elastic.

It is a method universal and uncomplicated at the same time, the result can be obtained from the test of one sample, it is also possible to apply in industrial conditions. The results of crack initial point test by this method slightly differ from the results obtained in pattern method, but more complicated, it is a method of crack alteration (about 2 – 8%).

Such a small value of differences in results can be completely accepted with concerning other methods being time-consuming, complex and expensive.

References

- [1] Neimitz A., *Podstawy mechaniki pękania*, WNT Warszawa 2003.
- [2] ASTM E 24.03.03: *Proposed standard method of test instrumented impact of precracked charpy specimens of metallic materials*.
- [3] SEP 1315: *Kerbschlagbiegeversuch mit Ermittlung von Kraft und Weg*, Stahl-Eisen-Prüfblatt des Vereins Deutscher Eisenhüttenleute, Düsseldorf 1997.
- [4] ISO EN DIN 14556: *Instrumented Impact Test*, Beuth Verlag, Berlin 2008.

- [5] ESIS (TCS) - *Proposed Standard for instrumented Charpy V-Test, Draft (7)*, Committee of Dynamic Testing at Intermediate Strain Rates, 1998.
- [6] Kobayashi T.: *Development in the instrumented impact test - computer aided instrumented impact testing system*. Charpy Centenary Conference, pp. 127-134, Paris 2001.
- [7] Kobayashi T. Yamamoto J. Niinomi M.: *Introduction of a New Dynamic Fracture Toughness Evaluation System*: Journal of Testing and Evaluation vol. 21 No 3, pp. 145-153, 1998.
- [8] Ranatowski E. Sadowski J.: *Possibilities of mathematical processing of the impact bend of charpy v samples diagram*. Journal of Theoretical and Applied Mechanics, pp. 237-248, 1995.
- [9] Ranatowski E. Sadowski J.: *Physical interpretation of impact bend test by means of mathematical methods*, Appl. Math. and comp. sci. vol. 3 No 2, pp. 281 - 300, 1995.
- [10] Lis Z. Narbudowicz K.: *Zastosowanie krzyżowego efektu magnetomechanicznego do wyznaczania inicjacji pęknięcia w próbie Charpy*. VI Konferencja Mechaniki Pęknięcia, pp. 237-249, Kielce 1997.
- [11] Lis Z. Narbudowicz K.: *Identyfikacja procesu dynamicznego pęknięcia na podstawie analizy sygnału emisji magnetycznej po transformacji waveletowej*, XVII Symposium Zmęczenia Materiałów i Konstrukcji, pp. 177-182, Bydgoszcz 1998.
- [12] Radakovic Z. Sedmak A.: *Determination of ductile crack initiation using pre-cracked Charpy specimens*. Charpy Centenary Conference, pp. 611-618, Paris 2001.
- [13] Spies A.: *Instrumented impact testing machine for determining impact fracture toughness by the impact response curve method*: Wolper V37 No2, pp. 14-18, 1997.
- [14] Sadowski J. Szykowny T.: *Relation between dynamic fracture toughness impact resistance KCV and structure of selected frictionally welded joints*, The Archive of Mechanical Engineering vol LI No 3, pp. 453 - 465, 2004.
- [15] Sadowski J.: *Wpływ czynników technologicznych na dynamiczną odporność na pęknięcie wybranych stopów odlewniczych*, Zagadnienia Mechaniki Stosowanej, UTP Bydgoszcz tom 3, pp. 87 - 97, 2011.

STRUCTURAL ANALYSIS OF THE FAN SECTION OF THE AIR HANDLING UNIT ON DYNAMIC LOAD DEFINED BY SEISMIC SPECTRUM

Dariusz Skibicki, Michał Burak, Łukasz Pejkowski, Michał Piotrowski

*University of Technology and Life Sciences in Bydgoszcz
Al. prof. S. Kaliskiego 7, 85-796 Bydgoszcz
e-mail: dariusz.skibicki@utp.edu.pl, mibu@utp.edu.pl*

1. Introduction

The aim of the research was to obtain stress and displacement maps of the structure of the air handling unit under load caused by the earthquake with spectrum that is characteristic for the area of OLKILUOTO 3. On this basis, the critical points of the structure were identified and the strength of the structure was assessed.

The calculation model of the air handling unit was generally based on the Finite Element Method. Calculations were carried out in LS-DYNA software. A finite element model was created and the results have been developed in the LS-PREPOST software.

Regarding to the standard [1] the seismic effects and the effects of the other actions included in the seismic design situation may be determined on the basis of the linear-elastic behaviour of the structure and the method for determining the seismic effects is the Modal Response Spectrum Analysis.

Thus for the calculation of a response of the structure subjected to input spectrum load, such as the acceleration, Response Spectrum Computation Method implemented in LS-DYNA was used (keyword *FREQUENCY_DOMAIN_RESPONSE_SPECTRUM) [3]. The method is based on results of modal analysis of a structure, e.g. natural frequencies and modal shapes. The method assumes that a maximum structure response is a combination of natural frequencies and mode shapes of the structure using free vibration analysis.

Two methods of combination of modes were used: Square Root of Sum of Squares (SRSS) and the complete quadratic combination (CQC), (parameter MCOMB : EQ.0 for SRSS method, EQ.2 for Complete Quadratic Combination method (CQC) [3]. For models with closely spaced mode shapes, the CQC method is precise whereas faster SRSS method estimates less accurate results [2]. The case which gave greater stress has been selected.

2. Structure modeling

The finite element model of the Air Handling Unit adequately represents the distribution of stiffness and mass so that all significant deformation shapes and inertia forces are properly accounted for under the seismic action considered. The model also accounts for the contribution of

joint regions to the deformability of the Unit. Non-structural elements, which may influence the response of the primary seismic structure, are also accounted for. Parts made of angles, shapes and sections or sheet metal plates were modeled via a shell elements, see Fig. 1, 2. Volumetric parts, such as e.g. a fan, have been modeled by solid elements.

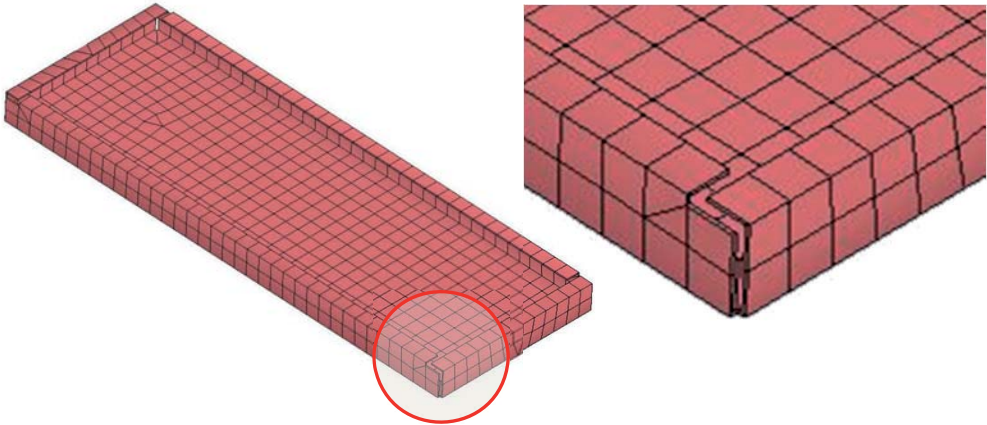


Fig. 1. Membrane type parts

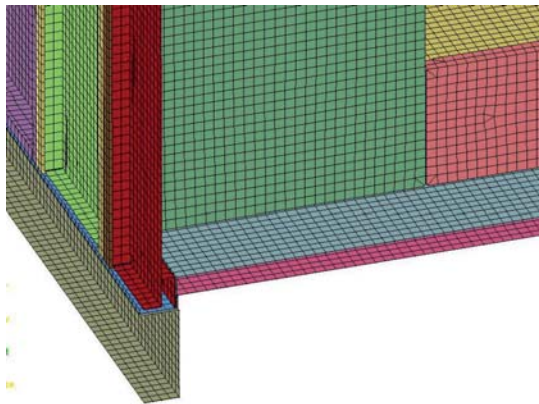


Fig. 2. Part assemblies

Screw connections between sheet metal parts were modelled using solid elements and special kind of part contacts implemented in LS-DYNA by `*CONTACT_SPOTWELD` command [3], Fig. 3. Welded joints were modelled using a special type of LS-DYNA contact between parts by `*CONTACT_TIED_SHELL_EDGE_TO_SURFACE` command [3], Fig. 4. Both doors were fitted with rigid connections in places of three hinges and door locks by `*CONSTRAINED_NODAL_RIGID_BODY` keyword [3]. The structure has been modelled taking into account all geometric interaction between the elements (contacts) using `*CONTACT_AUTOMATIC_SURFACE_TO_SURFACE` keyword [3].

Total number of parts of the structure is 71, not counting connections of elements (screws) and the fan assembly. The complete finite element model were consisted of 144'016 fully integrated linear assumed strain shell elements and 5'162 constant stress solid elements, Fig. 5.

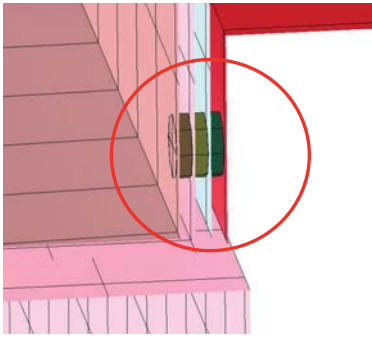


Fig. 3. Screw connection

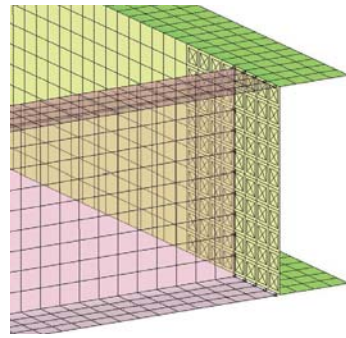


Fig.4. Welding connection

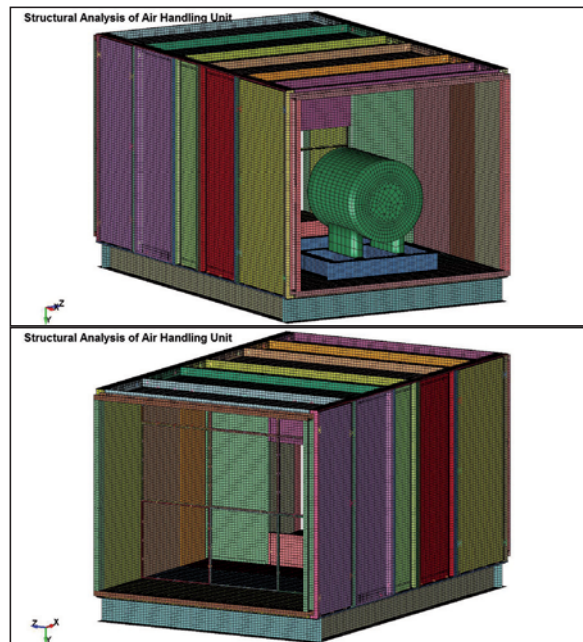


Fig. 5. Complete finite element model of the structure

3. Boundary conditions

Mounting the unit to the ground was modeled by means of withdrawal of all translational and rotational degrees of freedom of nodes lying on the lower surface of the base C-shapes , Fig. 6. A load in the form of spectrum was applied to the ground in the direction of the smallest stiffness of the air handling unit, i.e. in axis Z. The input spectrum was defined as an acceleration function from frequency, Fig. 7.

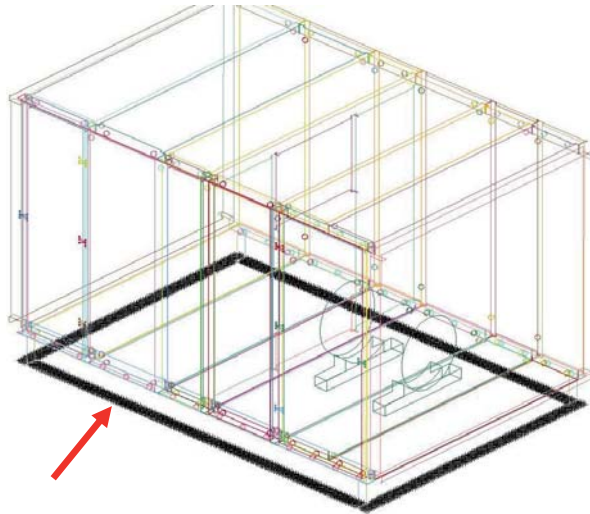


Fig. 6. Boundary conditions

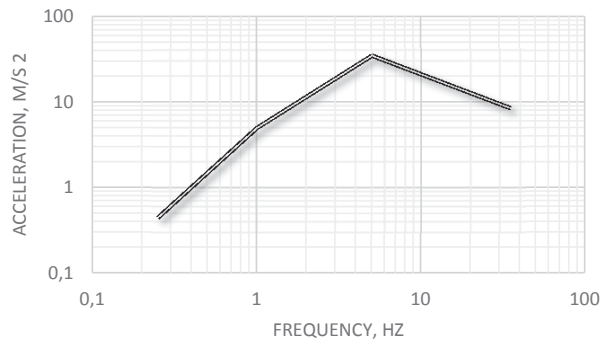


Fig. 7. Input load spectrum

4. Results

4.1. Modal analysis

As a result of modal analysis first 100 frequencies and mode shapes were calculated, Table 1. The examples of the mode shapes (in the form of displacements) are presented at the Fig. 8 – 11.

Table 1. First 100 modal frequencies

Mode	Frequency	Mode	Frequency	Mode	Frequency	Mode	Frequency	Mode	Frequency
1	7.59	21	24.66	41	32.67	61	38.47	81	43.43
2	8.90	22	24.68	42	32.98	62	38.59	82	43.44
3	15.28	23	25.20	43	33.05	63	38.59	83	44.06
4	15.32	24	25.91	44	33.16	64	38.61	84	44.22
5	15.34	25	26.00	45	33.21	65	39.44	85	44.60
6	17.01	26	26.16	46	33.73	66	39.46	86	46.17
7	17.02	27	26.72	47	34.46	67	39.94	87	46.19
8	17.04	28	28.21	48	34.70	68	40.26	88	46.30
9	18.03	29	28.47	49	34.73	69	40.76	89	46.47
10	18.24	30	28.69	50	34.80	70	41.04	90	46.47
11	19.19	31	28.90	51	35.01	71	41.11	91	46.49
12	19.40	32	29.64	52	35.14	72	41.22	92	46.55
13	20.06	33	30.10	53	35.90	73	41.23	93	46.55
14	20.07	34	30.84	54	36.25	74	41.25	94	46.57
15	20.09	35	30.84	55	37.20	75	41.29	95	46.60
16	20.54	36	30.85	56	37.32	76	41.31	96	46.65
17	22.70	37	30.86	57	37.35	77	41.36	97	46.88
18	23.90	38	30.95	58	37.41	78	42.76	98	47.10
19	23.94	39	31.14	59	37.93	79	43.34	99	47.47
20	24.66	40	32.56	60	38.35	80	43.36	100	47.86

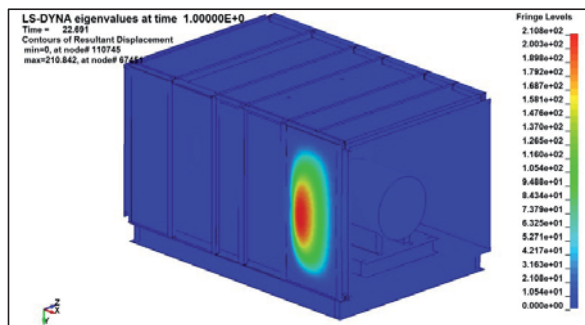


Fig. 8. 10th mode shape

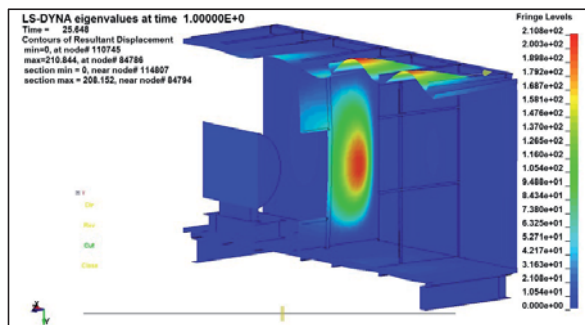


Fig. 9. 11th mode shape

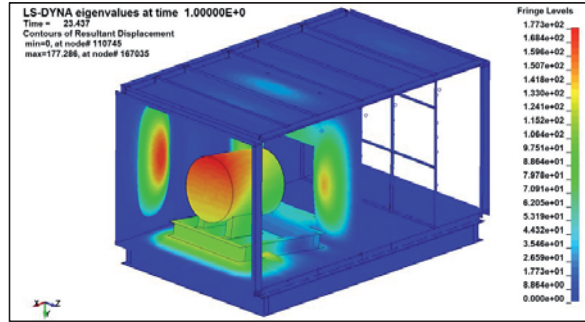


Fig. 10. 13th mode shape

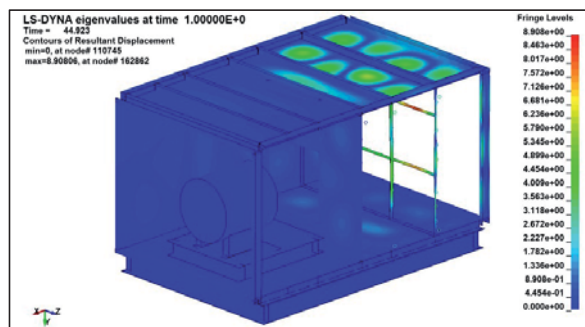


Fig. 11. 82th mode shape

4.2 Response of the structure to the load

The maximum response of the air handling unit subjected to input spectrum load was presented in the form of equivalent stress σ_{HMH} (Huber-Mises-Hencky) maps (Fig. 12). To determine the strength of the structure the maximal equivalent stresses σ_{HMH} were compared with allowable stresses k . Allowable stresses were calculated according to the formula:

$$\sigma_{HMH} \leq k = \frac{R_e}{x} \quad (1)$$

where: R_e – yielding stress, x – safety factor.

Calculated allowable stresses for structural wall, frames and screws are presented in the Table 2.

Table 2. Allowable stresses

Component type	Yielding stress MPa	Safety factors	Allowable stresses MPa
walls and frames	235	1.5	$k1 = 157$
screws	640	1.5	$k2 = 427$

The stresses in the frames and surfaces of membranes are of the order of several MPa's only, Fig. 12. Stresses in all critical points clearly satisfy the condition of strength, Table 3.

Table 3. Equivalent stresses in membrane parts

Point no.	Equivalent stress MPa	Allowable stresses MPa
61515	14.50	$\leq k1 = 157$
61516	14.48	
61514	11.70	
61517	11.50	

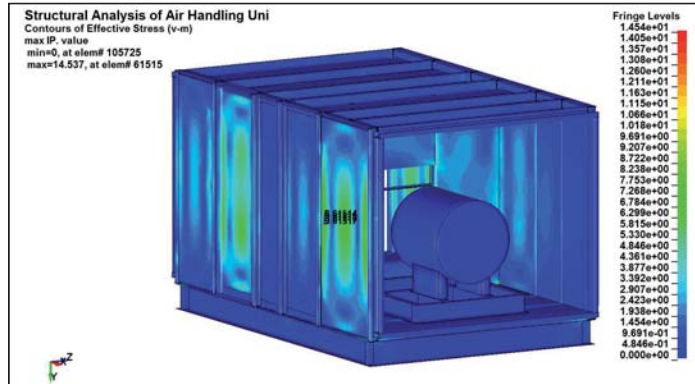


Fig. 12. Equivalent stresses in membrane parts

The highest values of stresses are in the bolts connecting the components. Location of the most loaded screws are shown in Fig. 13. Values of those stresses are given in Table 4.

Table 4. Stresses in the most loaded screws

Screw no.	Stresses MPa	Allowable stresses MPa
290	370.8	$\leq k2 = 427$
262	320.7	
307	319.0	
260	316.9	
139	314.1	
238	295.3	
310	288.2	
308	284.7	
289	272.0	
306	271.8	

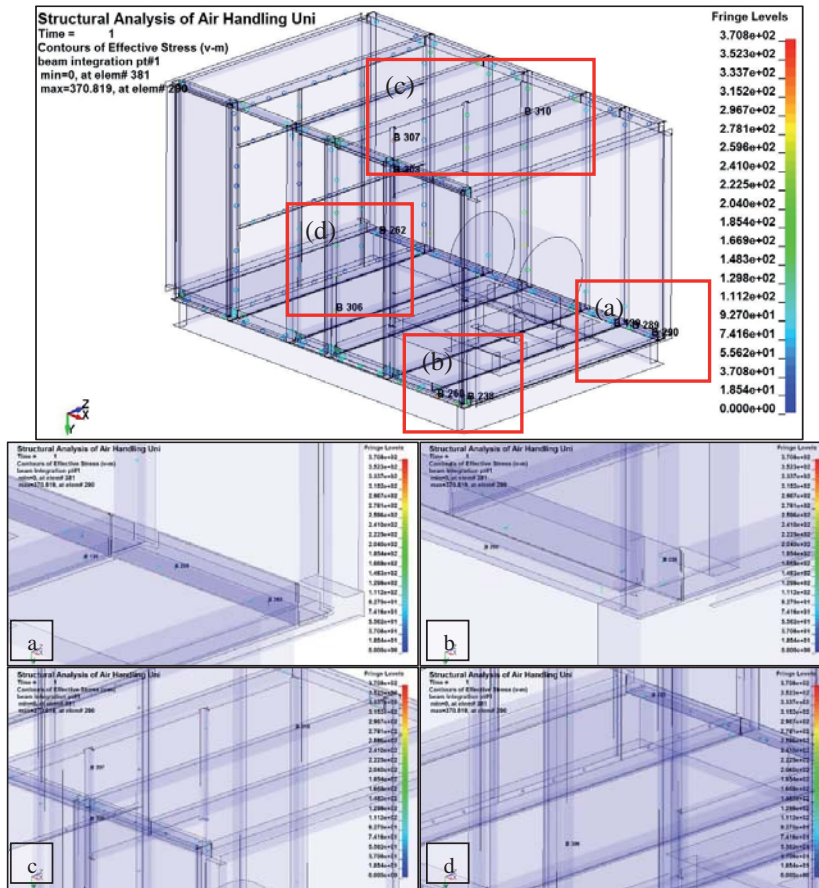


Fig. 13. Location of the most loaded screws

5. Conclusions

5.1. Conclusions about the structural analysis

- 1) The analysis showed which structural elements are most stressed and which are most deformed under load resulting from the earthquake.
- 2) Elements which are the most loaded are the screws. Sheet metal plates of the front doors are the parts which are the most deformed.
- 3) The stresses are in the elastic range and in all critical points satisfy the condition of strength.
- 4) Deflections of structure are very small and do not pose any threat to the stability of the structure. The strains are in the elastic range.

5.2. Conclusions about the calculation method

- 1) Since the stress values did not exceed the yield there is no need to use the Time History Method. Selected Response Spectrum Computation Method is entirely sufficient.

References

- [1] EN 1998-1:2004 Eurocode 8: *Design of structures for earthquake resistance - Part 1: General rules, seismic actions and rules for buildings* EN 1998-1:2004 (E)
- [2] Bavisetty, R., Vinayagamoorthy, M., Duan, L., *Dynamic Analysis. Bridge Engineering Handbook*. CRC Press, 2000
- [3] LS-DYNA Keyword *User's Manual Volumes I and II*, August 2012, Version 971 R6.1.0, Livermore Software Technology Corporation

PROBABILISTIC APPROACH FOR ANALITICALLY-DETERMINED FATIGUE CURVE

Przemysław Strzelecki*, Janusz Sempruch**

*University of Technology and Life Sciences
Faculty of Mechanical Engineering
ul. Prof. S. Kaliskiego 7, 85-789 Bydgoszcz
tel.: 693 897 581*
email: p.strzelecki@utp.edu.pl*
email: janusz.sempruch@utp.edu.pl***

Abstract

When a new machine element is to be designed, the dimension of the element must be defined by calculating fatigue strength or life. To calculate it, fatigue characteristic of this part must be known. To acquire the information on such properties, the analytical method can be applied. Fatigue curve plotted that way is corresponding to 50% probability of the element failure. However, for engineering calculations there must be used a characteristic curve of 95% level of reliability or higher. The paper presents the method of the translocation of the fatigue curve, applying the analytical method to the technical requirements of probability. To verify this approach, an experiment was carried out to get fatigue characteristics of material C45+C and 42CrMo4 and comparisons were made for that estimated curve with the characteristics provided by the analytical method to require reliability. The fatigue test was made using smooth specimen and loaded by rotating bending. The comparison performed indicates sufficient analytical curve as compared with the characteristics estimated from the experiment. One shall note that the reliability coefficient can be used to substitute the safety coefficient which can assume a large value as there is no applicable knowledge available.

Keywords: *high-cycle fatigue strength, fatigue plots, analytical methods of estimating Wöhler characteristics.*

1. Introduction

In designing of new machine elements their dimensioning is performed. To do so, calculations are carried out to evaluate fatigue strength or life. For make that calculation, fatigue characteristics of the material or construction element must be known. To get such data, long and costly fatigue tests are required. Frequently at the beginning of the design project, it is not possible to realize such test and so analytical methods are used, e.g. the one presented in [2,3,6]. The characteristics provided using any of the methods correspond to 50% of the probability of the element failure. From this perspective, real construction reliability is required at 95% level or higher. Further on the paper presents the approach which can be feasible for such characteristics to be received. When an engineer does not have any data on the probability of failure of the design element, the safety coefficient is used. The value of the coefficient ranges from 1.3 to 2.5 according to [1], where the authors noted that the persons who do not have experience in designing elements loaded by variable force should apply the values from 2.5 to 4. However publication [4] suggests the range from 1.1 to 6.12 if there is no credible data available to calculate the value.

2. Presentation of selected analytical method

The method presented in paper [7] is based on FITNET method where the definition of coefficient m has changed. The first step of this approach determines the fatigue limit using the following equations (after[3]):

$$\sigma_W = f_{W,\sigma} \cdot R_m \text{ lub} \quad (1)$$

$$\tau_W = f_{W,\tau} \cdot \sigma_W, \quad (2)$$

where:

R_m – ultimate strength,

$f_{W,\sigma}, f_{W,\tau}$ – coefficient depending from type of material (after[3]).

In the method proposed, the value of slope coefficient is calculated with the following equations [7]:

$$m_e = \frac{\log\left(\frac{10^6}{N_{Re}}\right)}{\log\left(\frac{0,9R_e}{Z_G}\right)}, \quad (3)$$

$$N_{Re} = 400 \left(\frac{R_e}{R_m}\right)^{-10}, \quad (4)$$

where:

R_e – yield strength of material.

Graphic representation of the approach is shown in fig. 1.

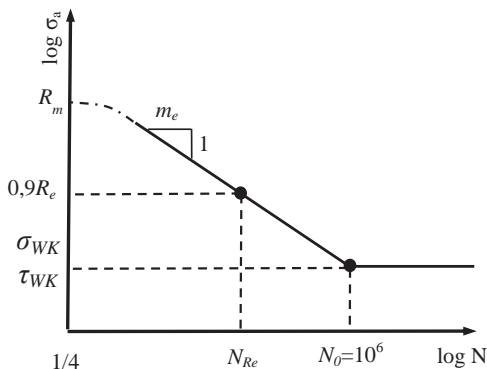


Fig. 1. Fatigue curve according analytical method from [7]

3. Probabilistic approach to determined analytical fatigue limit

It is commonly known that the distribution of fatigue limit is similar to the normal distribution [1,2]. With such assumption it is possible to define the probability of the strength value of unlimited fatigue life [2]. Using the equation for standardizing normal distribution, the following can be noted:

$$Z = \frac{Z_{GR} - \mu}{s}, \quad (5)$$

where:

Z – value of random variable from normal distribution,

Z_{GR} – random variable of fatigue limit,

μ – value of mean of fatigue limit (it can assumption Z_G),

s – standard deviation.

Assuming that probability of failure of sample loaded by defined stress amplitude is given by following equation:

$$P(Z < \mu) = \Phi(Z) = 1 - R, \quad (6)$$

$$Z = \Phi^{-1}(1 - R), \quad (7)$$

where:

$\Phi(Z)$ – standard normal density function,

R – level of reliability.

Coefficient of variation define as:

$$V = \frac{s}{\mu}, \quad (8)$$

and to equation (7) substituting Z with equation (5) and replacing quantity s by the quantity obtained from equation (8) we will get the following:

$$Z_{GR} = \mu + \Phi^{-1}(1 - R) \cdot \mu \cdot V. \quad (9)$$

By introducing the coefficient of reliability which reduces the value of fatigue limit to the value adequate to assuming the probability of failure, the following equation is obtained:

$$Z_{GR} = C_R \cdot \mu, \quad (10)$$

where:

C_R – coefficient of reliability.

By substituting C_R to equation (9), we will obtain the following equation:

$$C_R = 1 + \Phi^{-1}(1 - R) \cdot V. \quad (11)$$

Assuming that the coefficient of variation of fatigue limit assumes the value 0.08 (according [2,4]), it is possible to determine the value of the coefficient of reliability. The value calculated has been presented in Table 1.

Tab. 1 Value of coefficient of reliability for diferend levels of reliability

R	C_R
0,9	0,897
0,95	0,868
0,98	0,836
0,99	0,814
0,999	0,753
0,9999	0,702

Finally the dependence to calculate the fatigue limit for the required level of reliability Z_{GP} can be given as follows:

$$Z_{GP} = Z_G \cdot C_R. \quad (12)$$

4. Comparison of characteristics obtained by analytical and experimental method

The characteristics estimated experimentally for material C45+C and 42CrMo4 are presented in Figures 4 and 5. Static properties are given in Tab. 2. The first material was tested in delivery state in form of cold-drawn bars 10 mm in diameter. The second material (42CrMo4) has been quenched and tempered to harden the surface up to 30 HRC. The dimensions of the specimen are given in Fig. 2. The samples were loaded by rotary bending at the frequency of 28 Hz. The test equipment of own design; the device verification is presented in paper [6].

Tab. 2 Static properties of material C45+C and 42CrMo4

Material	Yield limit /proof stress [MPa]	Tensile strength [MPa]
C45+C	-/647	826
42CrMo4	1095/-	1172

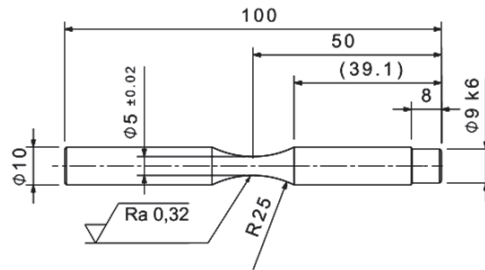


Fig. 2. Sample used for tests

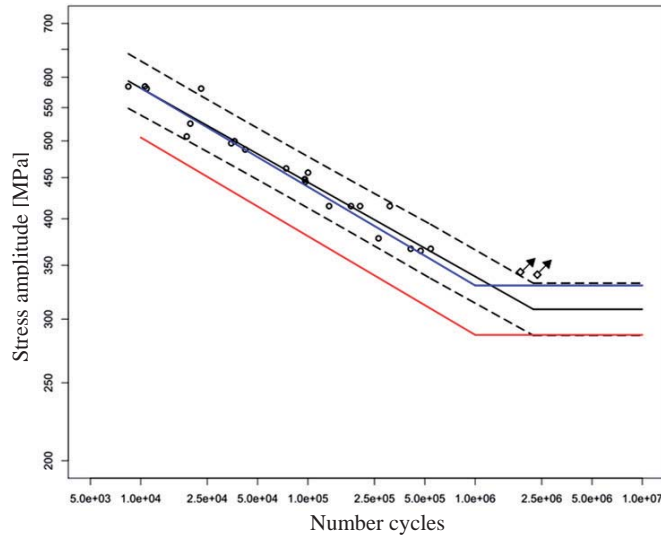


Fig. 3. Fatigue curves for C45+C steel where black line - estimated curve for experimental data for 50% probability, dotted line - fatigue curve for probability of failure 95% and 5%, the curve obtained using the analytical method according to [7], red line - the curve obtained applying the analytical method according to [7] with the fatigue limit corrected with equation (12) for the reliability of 95%

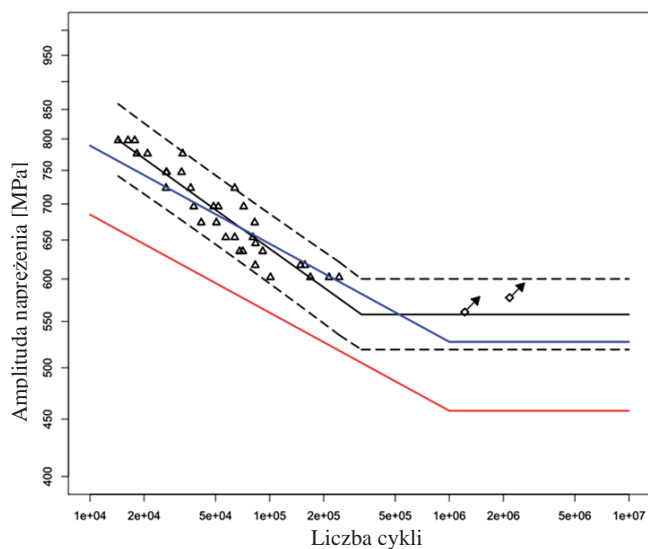


Fig. 4. Fatigue curves for 42CrMo4 steel where black line – the estimated curve for experimental data for 50% probability, dotted line – fatigue curve for probability of failure 95% and 5%, blue line- curve obtained using the analytical method according to [7], red line – the curve plotted applying the analytical method according to [7] with the fatigue limited corrected with equation (12) for the reliability of 95%

Based on the figures plotted, there were determined the strength for 10^5 cycles according to the characteristics of 50% and 95% probability. The results for each material and method are given in Table 3.

Tab. 3 Value of fatigue strength for 10^5 cycles according analytical and experimental method

Method of determine fatigue curve	Material	Fatigue strength for 10^5 cycles for 50% probability [MPa]	Fatigue strength for 10^5 cycles for 95% probability [MPa]	Ratio of strength for 50% and 95% probability characteristics
Analytical method	C45+C	421,1	365,5	1,15
	42CrMo4	645,1	560	1,15
Experimental method	C45+C	443,8	411,9	1,08
	42CrMo4	631,8	594,4	1,06

5. Summary and conclusions

Applying equation (12), it is possible to define the fatigue limit, determined using the analytical method, of the required level of probability of the forecast correctness. Based on that assumption one can receive fatigue characteristics at the reliability level required. The figures show the characteristics are on ‘a safe’ side (underestimated fatigue life/strength estimated).

Additionally, the application of probabilistic approach gives the designer a possibility of giving up conservative values of the safety coefficient. With such approach the engineer can decide himself what safety level is adequate for the machine being designed. In the present example of determining the fatigue characteristics with the analytical method the coefficient of reliability was used at the level of 95%. In that case there was obtained the coefficient of safety of 1.15. It is the value which is relatively low as compared with those offered in literature. One shall note that if required by safety requirements, the value can be increased applying the coefficient of reliability at a higher level.

Acknowledgement

The work has been co-financed by the European Union Social Fund, the state budget of Poland and the budget of the Kujawsko-Pomorskie Province as part of the project '*Krok w przyszłość – stypendia dla doktorantów*', the 4th edition.

Literatura

- [1] Kocańda S., Szala J., *Podstawy obliczeń zmęczeniowych*, PWN, Warszawa, 1997.
- [2] Lee Yung-Li, Pan Jwo, Hathaway R. B., Barkey M. E., *Fatigue testing and analysis*, University of Alabama, Elsevier 2005.
- [3] Neimitz A., Dzioba I., Graba M., Okrajni J., *Ocena wytrzymałości, trwałości i bezpieczeństwa pracy elementów konstrukcyjnych zawierających defekty*, Politechnika Świętokrzyska, Kielce 2008.
- [4] Niezgodziński M.E., Niezgodziński T., *Wzory wykresy i tablice wytrzymałościowe*, wyd. 9, Warszawa WNT, 2004.
- [5] Pook L., *Metal fatigue what it is. Why it matters*, London Springer 2009,
- [6] Strzelecki P., Sempruch J., *Experimental Verification of the Analytical Method for Estimated S-N Curve in Limited Fatigue Life*. Materials Science Forum, Vol. 726, 2012, pp. 11-16.
- [7] Strzelecki P., Sempruch J., *Modification of selected methods of rapid determination of fatigue characteristics in the range of limited fatigue life*, Journal of Polish Cimac Selected problems of designing and operating technical systems Vol. 6 No 3; 2011, pp. 289-296.

MULTIFRACTAL SCALING LAW FOR HIGH-CYCLE FATIGUE STRENGTH APPLIED TO ALUMINUM ALLOY

Tomasz Tomaszewski, Janusz Sempruch

*University of Technology and Life Sciences in Bydgoszcz
ul. Kaliskiego 7, 85-796 Bydgoszcz, Poland
tel.: +48 52 3408202, fax: +48 52 3408245
e-mail: tomaszewski@utp.edu.pl*

Abstract

Fatigue strength of the material decreases with an increase in the cross sectional area of the specimen. Such phenomenon can be described phenomenologically applying the fractal approach, describing a change in the strength properties by applying the fractal dimension. With that approach involves modelling the damage of a material ligament. The damage size depends on the defects and microfractures in the object analysed. The effect of the disordered material microstructure on the mechanical properties is decreasing with an increase in the cross sectional area of the object. Bearing that in mind, the description of the size effect should use nonlinear scaling (multifractal scaling law). That approach was used for the results of high-cycle fatigue studies, for various aluminum alloys. Determining the model parameters facilitates the evaluation of fatigue life and strength for the plants with a different geometry than the specimens studied in the lab.

Keywords: *size effect, fractal approach, aluminum alloy*

1. Introduction

Fatigue strength and fatigue life changes depending on the cross-sectional area. This phenomenon was studied and described in more detail as the size effect. The effect of the change in the cross-section on the strength properties of the material depends on the kind and the local properties of the material; including micromechanical material damage which are indispensable mechanism disturbing its structure [3]. The size effect is described with coefficient K_d which is a quotient of the specimen fatigue strength with any cross-section to the normative specimen fatigue strength determined for the same fatigue life [7]. To present the degree of the change in coefficient K_d against the cross sectional area, Fig. 1 presents the results of the experiments reported for selected aluminium alloys.

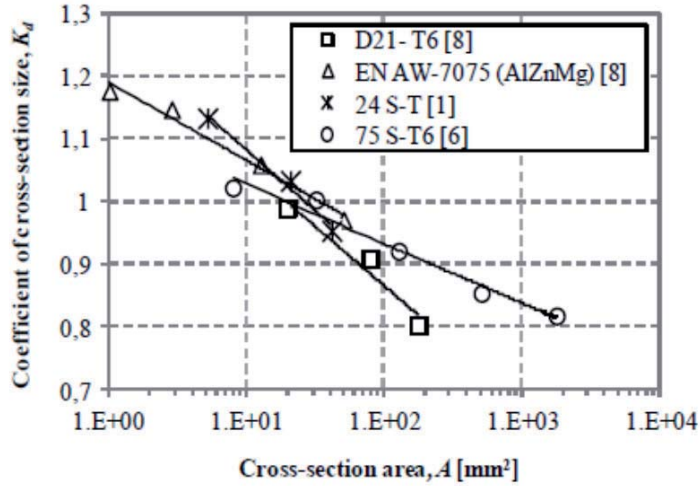


Fig. 1. Dependence of the coefficient of the cross-section (K_d) to the cross sectional area of round bendable specimens – own study based on [1, 6, 8]

To provide a description of the size effect of construction materials, the fractal approaches can be applied [2, 3]. The main assumption is to evaluate the strength properties of the plants different in size than the specimens studied in the lab. The extrapolation of the values can take place towards non-standard specimens (e.g. mini specimens) [7] or real-life plants with a much greater cross sectional area.

The aim of the present paper has been to determine the multifractal model parameters for a given group of construction materials. Additionally the aim of the paper is also to determine the lowest fatigue strength for the infinite value of the cross sectional area and the value transitional for the material structure. The model analysis has been based on the results of experiments reported in literature for various aluminium alloys.

2. Fractal approach

To describe the sensitivity of the material to the change in the size of the cross-section, fractal models are used in the scope of tensile strength [3] and fatigue strength [4, 5]. Applying the fractal approach involves the modelling of a damaged material ligament. Its weakening comes from defects and microfractures all throughout the size scope of the object. In the macroscopic scale, nominal strength σ is defined for nominal area a_0 . As for an increase area, there occurs more and more discontinuity resulting in a decrease in nominal area a_1 responsible for fictional micro-stress σ_1 . On the border of the microscopic scale there is assumed value a^* for renormalized strength σ^* determined from the dependence [3]:

$$\sigma^* = \frac{F}{A^{-d}} \quad (1)$$

where:

- F – external force,
- A – cross-sectional area,
- d – fractal dimension ($0 < d < 0.5$) of the ligament resulting from disordered material.

External force F does not change against the observation scale, which can be written as $F = \sigma a_0 = \sigma_1 a_1 = \dots = \sigma^* a^*$. The cross-sectional area of object A can be compared to nominal areas $a_0 \sim A$, $a^* \sim A^{-d}$. In the bilogarithmic pattern the dependence of the strength to the

cross-sectional area has been described with a straight line with a slope equal β_σ (Fig. 2) where the nominal strength decreases with an increase in the cross-sectional area.

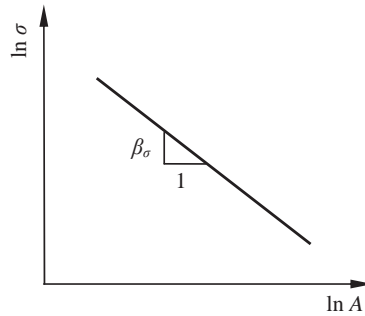


Fig. 2. Monofractal scaling for strength σ against cross-sectional area A [3]

The monofractal approach described is a linear fractal scaling law. It is true only for a narrow range of sizes in which the fractal size is a constant value. The monofractal approach does not have the upper and lower limit for the scaling range. Cross-sectional area A is tending to infinity, which leads to unrealistic values for strength σ tending to zero. For the objects with a large cross-sectional area, it is false since they have a finite strength value.

Besides, there has been suggested the multifractal approach [3] (nonlinear model) which assumes a gradual disappearance of fractality (d tending to zero). Disordered material microstructure does not depend on the size of the object. However, the effect of disorder on the mechanical properties depends on the ratio of characteristic internal length l_{ch} to external specimen cross-sectional area A . It leads to a decrease in the effect of material microstructure together with an increase in the object size. Drawing on that assumption, multifractal scaling law (MFSL) for strength assumes the following form [3]:

$$\sigma(A) = f_t [1 + l_{ch} / A]^{1/2} \quad (2)$$

where:

- f_t – the lowest value of nominal strength,

- l_{ch} – characteristic internal length (material constant dependent on the cross-sectional area).

The graphic representation of dependence (2) is given in Fig. 3. Asymptotic value f_t corresponds to the lowest nominal strength for infinite cross-sectional area A . Characteristic value of internal length l_{ch} represents the variable of the effect of disorder on mechanical properties.

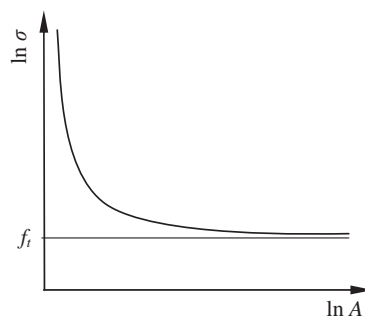


Fig. 3. Multifractal scaling law for strength against cross-sectional area A [3]

3. Multifractal scaling law

Multifractal scaling law (MFSL) can be applied to describe high-cycle fatigue strength. The main relation of MFSL is based on parameter C_r depends on the cross-sectional area A . This relation assumes the form of (original relation [4] depends on the diameter D):

$$C_r = C(A)^{\frac{1}{100}} = \left[\frac{a}{f \cdot (1/A) + 1} + b \cdot (1/A) + c \right]^{\frac{1}{2}} \quad (3)$$

where:

- C – constant parameter of fatigue characteristics σ_a-N with the Basquin equation $C = N(\sigma_a)^k$,
- $a = y_Q - y_P$,
- b – asymptote slope,
- $c = y_P$,
- f – value for the best fitting of the model.

Besides, parameters a , b , c are closely dependent on the material investigated. Exponential equation for C_r^2 is a graphic representation in Fig. 4 considering characteristic points y_P , y_Q .

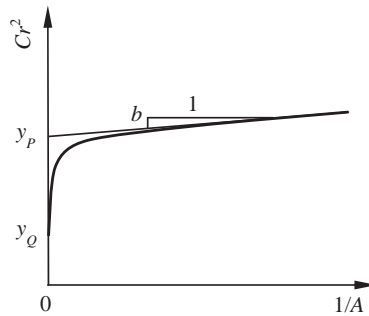


Fig.4. Dependence of the second power of parameter C_r^2 for cross-sectional area $1/A$ considering characteristic points y_P , y_Q [4]

The model facilitates determining the values characteristic for the material analysed. Fig. 5 provides the curve determined from relationship (3) and coordinates of characteristic point T . The first coordinate is the lowest fatigue strength $\ln C_{r\infty}$ for infinitely large cross-sectional area A , determined from the relationship [4]:

$$C_{r\infty} = (a + c)^{1/2} \quad (4)$$

Yet another one is parameter A_T treated as transitional value for the material structure size. It is determined from the dependence [4]:

$$A_T = \frac{b}{a + c} \quad (5)$$

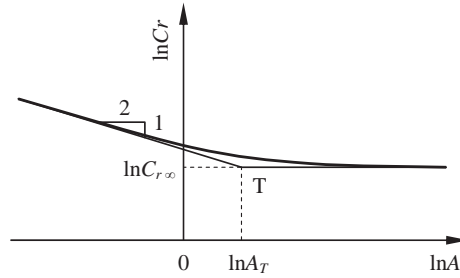


Fig. 5. Dependence of parameter $\ln C_r$ to cross-sectional area $\ln A$ considering intersection T [4]

4. MFSL Application

Multifractal scaling laws have been applied for the results of the tests of high-cycle fatigue testing for aluminum alloy D21-T6 [8], EN AW-7075 (AlZnMg) [8], 24 S-T [1], 75 S-T6 [6] (original material markings following the authors of papers have been applied). The analyses facilitated determining model parameters (Table 1) described with the relationship (3) and served for nonlinear description of parameter C_r^2 for $1/A$ (Fig. 6). For parameters a, b, c , recorded, there was determined parameter f responsible for the best fitting of the model for the results of the experimental studies. The parameters should be treated as similar. As for the case increase in the scope of geometries analysed (greater A scope), the model received will be more detailed.

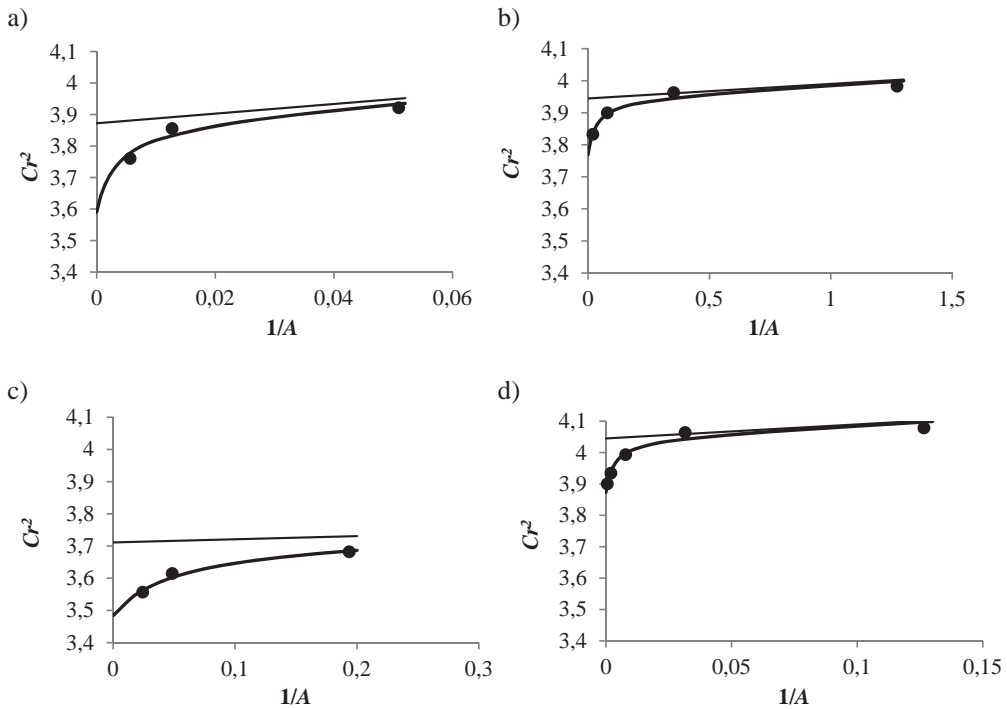


Fig. 6. Dependence of parameter C_r^2 to $1/A$ for the aluminium alloy analysed: a) D21-T6, b) EN AW-7075 (AlZnMg), c) 24 S-T, d) 75 S-T6

Tab. 1. Parameters of the MFSL model for the aluminium alloy analysed

Aluminum alloy	a	b	c	f
D21-T6	-0,282	1,535	3,872	305,7
EN AW-7075 (AlZnMg)	-0,175	0,045	3,945	29,7
24 S-T	-0,227	0,097	3,712	20,5
75 S-T6	-0,171	0,449	4,045	302,6

Fig. 7 shows plotting of the points from the results of experiments and curves received from the model of dependence (3). From dependences (4), (5) there were determined the coordinates of point T (compliant with Fig. 5) given in Table 2. From the plots one can see that parameter C_r decreases with an increase in cross-sectional area A . The size of the slope/decrease is comparable for all the aluminium alloy analysed.

Tab. 2. Characteristic values received for model MFSL for the aluminium alloy s analysed

Aluminum alloy	A_T	$C_{T_{\infty}}$
D21-T6	0,427	1,89
EN AW-7075 (AlZnMg)	0,012	1,94
24 S-T	0,028	1,87
75 S-T6	0,116	1,96

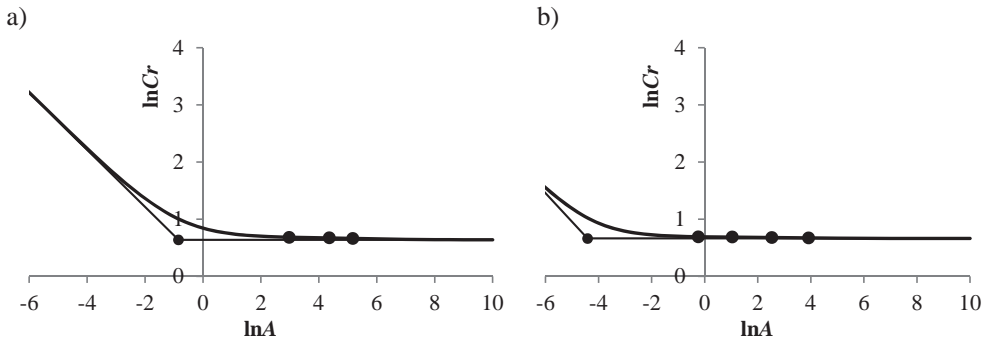


Fig. 7. MFSL model curve for characteristic T and experimental points for the select aluminium alloys analysed: a) D21-T6, b) EN AW-7075 (AlZnMg)

5. Conclusion

A decrease in the strength properties of the construction material as a result of a change in the cross-sectional area can be described with fractal approaches. The decrease/slope gradually disappears together with an increase in the cross-sectional area and so in the case of large objects it is indispensable to apply the nonlinear approach. Knowing the fractal approach model parameters for a given group of construction materials, it is possible to evaluate the fatigue life for the objects with a different geometry than the specimens tested in the lab.

The paper analyses the multifractal scaling law for selected aluminium alloys. The approach was applied in the scope of high-cycle fatigue for fatigue characteristics σ_a-N determined experimentally. For each of the materials analysed there were determined mean characteristic quantities of the MFSL model: structure transition value $A_{T_{\infty}} = 0.15$, infinite

fatigue strength $C_{r_{\infty, S_r}} = 1.92$. Convergent values A_T and $C_{r_{\infty}}$ for the materials analysed show a similar susceptibility to a change in the cross-section and a similar structure of the materials analysed.

References

- [1] Brueggeman, W. C., Mayer., M. Jr., *Axial fatigue tests at zero mean stress of 24S-T and 75S-T aluminum-alloy strips with a central circular hole*, NACA, pp. 1-24, 1948.
- [2] Carpinteri, A., *Scaling laws and renormalization groups for strength and toughness of disordered materials*, International Journal of Solids and Structures vol. 31 no. 3, pp. 291-302, 1994.
- [3] Carpinteri, A., Chiaia, B., *Multifractal scaling laws in the breaking behavior of disordered materials*, Chaos, Solitons & Fractals vol. 8 no. 3, pp. 135-150, 1997.
- [4] Carpinteri, A., Spagnoli, A., *Size effect in S-N curves: A fractal approach to finite-life fatigue strength*, International Journal of Fatigue 31, pp. 927-933, 2009.
- [5] Carpinteri, A., Spagnoli, A., *A fractal analysis of size effect on fatigue crack growth*, International Journal of Fatigue 28, pp. 125-133, 2004.
- [6] Hyler, W. S., Lewis, R. A., Grover, H. J., *Experimental investigation of notch-size effects on rotating-beam fatigue behaviour of 75S-T6 aluminum alloy*, NACA, pp. 1-48, 1954.
- [7] Tomaszewski, T., Sempruch, J., *Determination of the fatigue properties of aluminum alloy using mini specimen*, Materials Science Forum 726, pp. 63-68, Switzerland 2012.
- [8] Troshchenko, V. T., Sosnovskiy, L. A., *Fatigue resistance of metals and alloys*, Academy of Sciences of the Ukrainian SSR [in Russian], 1987.



ANALYSIS OF THE WEIBULL DISTRIBUTION FOR STATIC 3-POINT BENDING OF ZIRCONIUM DIOXIDE

Mateusz Wirwicki, Tomasz Topoliński,

University of Technology and Live Sciences in Bydgoszcz
ul. Kaliskiego 7, 85-796 Bydgoszcz, Poland
tel.: +48 52 3408497, fax: +48 52 3408245
e-mail: wirwicki@utp.edu.pl

Abstract

The paper presents the results of studies of the strength of dental material; zirconium dioxide in terms of the needs of dentists. More and more frequently it happens that dentists require not only mean value (or scope) of strength of a given material as well as the analysis of its reliability under load. It seems that it is necessary each day while taking a decision on the material for the fully-ceramic crown or bridge if the element considering the properties assumed by the manufacturer is to meet the patient's expectations. The aim of the paper is to evaluate the risk and to determine the parameters of distribution of the damage probability for zirconium dioxide specimens. The paper has been based on the results of studies of 3-point bending of cuboid beams. There has been presented a method of zirconium dioxide specimen treatment. It has been considered what effect on the scatter of the results is attributed to the cross-section of the specimens. There were determined characteristic stresses σ_0 , for which 63% of the specimens will get destroyed.

Keywords: zirconium dioxide, biomaterial, three point bending, Weibull analysis

1. Introduction

Contemporary material studies of new biomaterials, including dental ceramics, in many cases cover not only direct material characteristics, such as: compression strength, bending strength, tensile strength, hardness or fragility but also the forecast of maintaining those characteristics under operation conditions. As operation conditions for zirconium dioxide, used for the reconstruction of the tooth crown or 3- and 4-point bridges, one shall understand food chewing or consuming liquids at various temperatures. For each clinical application the dentist must evaluate the risk of damage of the solution proposed. For that reason the mechanical strength studies for ceramics must be extended by the reliability analysis, which often uses the Weibull distribution. The shape parameter, namely the Weibull modulus, is an indicator of variation in the material strength. It has been noted that the higher the value of the Weibull shape parameter m , the higher the clinical reliability [1,2]. The parameter of the Weibull distribution scale σ_0 will determine, in our case, a characteristic value of the material strength for which 63.2% of the elements made from a given material get damaged [3,4]. The value of strength σ_0 can be described referring to e.g. the method of material treatment or syntethisation method. The literature review allows for concluding that the studies reflect the operation conditions of the crown or bridges, the 3- and 4-point ones, made based on bending tests. If you want to investigate the material; zirconium dioxide otherwise referred to as technical advanced ceramics, one shall comply with the PN-EN 843-1:2006 norm. The 3-point bending in its simplest form can be compared, in terms of mechanics,

for two construction elements working: teeth for chewing process in the oral cavity. On the dental market there are dental ceramics of various generations. The study of bending strength for ceramics, namely zirconium dioxide, is to help to evaluate the risk and the damage probability considerably. The study of bending strength is also an important criterion of clinical applicability of ceramic materials and it is especially important while facing a very fast development of ceramic materials.

The aim of this paper is to evaluate the risk and the damage probability for zirconium dioxide used in dental surgeries.

2. Material and method

The research involved the use of material under trade name Cyrkon Lava manufactured by 3M used to create crowns and bridges following the CAD/CAM technology. The material supplied by the producer was been cut-in with the circular saw provided by Buehler ISOMET 5000 [POLAND] into smaller blocks 25 mm x 16mm x 1.87mm in size. The elements are exposed to laser-cutting using Alfalas WS [POLAND] with the laser settings not allowing for zirconium dioxide overheating. From the cut made that way one receives 8 specimens 1.87mm x 1.87mm x 15mm in size. Then the specimens are sent to the manufacturer-licensed laboratory in which sinterization takes place. Sinterization in a special oven at the temperature of 1410°C took 8 hours. During that time there occurs technological shrinkage of the entire crown accounting for about 20% of the crown volume. The material after sinterization is snow-white and shows a significant increase in the mechanical properties parameters. Fig. 2 presents the geometry of the specimens after the process of sinterization. After synthetization one receives specimens for tests about 1.5 mm x 1.5 mm x 12 mm in size.

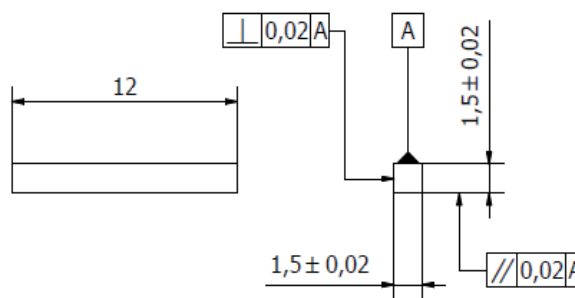


Fig. 1. Specimens geometry

The material tested in dental clinics is used to make single crowns, 3- and 4-point bridges and implant connectors. The advantage of the zirconium dioxide is high strength, excellent and natural aesthetics. The material also has a very good translucency and biocompatibility and its structure shows a lack of metals. When providing functional descriptions it is considered dental ceramics for the representatives of which in Table 1, against the density, the basic mechanical parameters are given. Interestingly, the materials broken down in the table, except for zirconium dioxide, must be placed – surface-welded on metal cups and only when the crowns are prepared that way etc. they can be glued to the natural tooth.

Table 1. Mechanical properties of selected dental ceramics

Ceramics	Bending strength [MPa]	Vickers hardness [GPa]	Density (g/cm ³)
Reinforced with mica	71 -107	3.72 – 4.46	2.56
Reinforced with leucite	109 – 154	6.57 – 6.67	2.50
Aluminium trioxide	601 – 687	15	2.47
Zirconium dioxide	840 - 1200	12.17 – 13.70	5.56 – 6.1

Static bending strength study

The studies of bending strength were performed compliant with the PN-EN 843-1:2006 norm. The norm provides the guidelines how to make a specimen of an assumed geometry, perform research for 3- and 4-point bending and to make auxiliary devices during strength testing. Thirty specimens to be tested were made in a form of cuboid beams 1.5mm x 1.5mm x 12mm in size. The 3-point bending study was performed using the strength testing machine Instron 8874 with the use of strain dynamometer with the measurement range of ± 5 kN. The speed of the dislocation of the upper arm (machine actuator) was 0.5 mm/min, which made it possible to meet the normative guideline that the time of the specimen load until breaking should fall within the range from 5 to 15s. The beams of the support tangent to the specimen corresponded to 1.5 of the specimen thickness, which is also a normative requirement.

Breaking stresses have been calculated from the following formula:

$$\sigma_f = \frac{3Fl}{2bh^2}$$

where:

σ_f – breaking stress in [MPa];

F – maximum force upon breaking in [N];

b – specimen width in [mm], mean for three records;

h – specimen thickness expressed in [mm], mean for three records;

l – distance between the centres of external supporting rollers in [mm] [5].

Fig. 2 demonstrates the plot of the damage probability in the normal distribution network. A high value of the coefficient of determination clearly points to the possibility of making assumption that the variation in strength undergoes normal distribution. The analysis used the results reported in the studies for 23 specimens, compliant with the norm described, 7 results have been rejected as deviating.

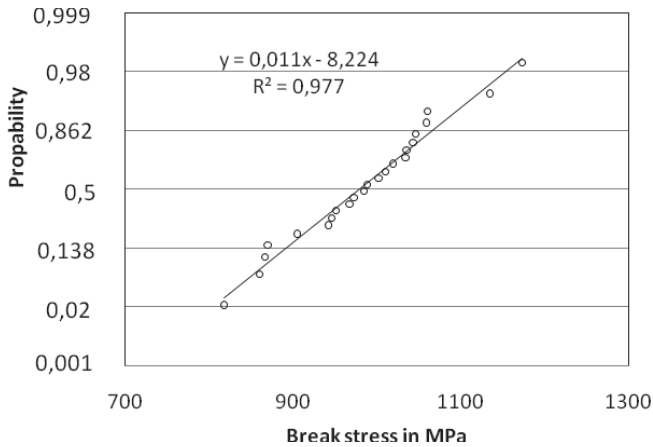


Fig. 2. Specimen damage probability.

Table 2 presents the results from the static 3-point bending test. One can note a considerable scatter of the results. An attempt has been made to identify the dependence between the cross-section of the specimen and the values received. No such dependence was observed.

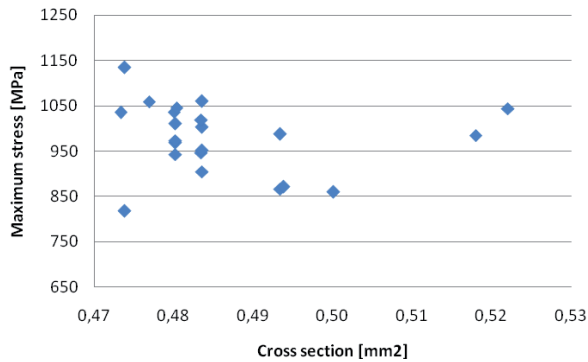


Fig. 3. Dependence of the break force to the coefficient of strength of the cross-section to bending.

Quite a high scatter of the results can suggest that other factors were essential, including a considerable shrinkage of the material, heating and cooling pattern or material homogeneity.

Table 2. Results of static 3-point bending studies

Range of breaking stresses	Mean value	Standard deviation	Relative standard deviation
817 ÷ 1134MPa	986MPa	78.3MPa	8 %

Weibull analysis

The reliability analysis of the zirconium dioxide ceramics was performed using the Weibull distribution based on the guidelines provided for in PN-EN 843-5:2006. Distribution function P_f of the Weibull distribution is described with the following relationship:

$$P_f = 1 - \exp \left[-N \left(\frac{\sigma - \sigma_u}{\sigma_o} \right)^m \right]$$

where:

P_f – damage probability; N – specimen number; σ – breaking stresses; σ_u – location parameter; σ_o – size parameter; m – shape parameter; e – constant = 2.718... [6].

Table 3 presents the number of specimen N , characteristic strength σ_o , coefficient of determination R^2 and the Weibull modulus m for zirconium dioxide Lava provided by 3M.

Table 3. Breakdown of results for the analysis of the Weibull distribution

N	σ_o	R^2	m
22	1026,7	0,955	14

Fig. 3 presents the plot of linear approximation after the logarithmic conversion of the strength results into 3-point bending, the regression equation and the coefficient of determination are presented.

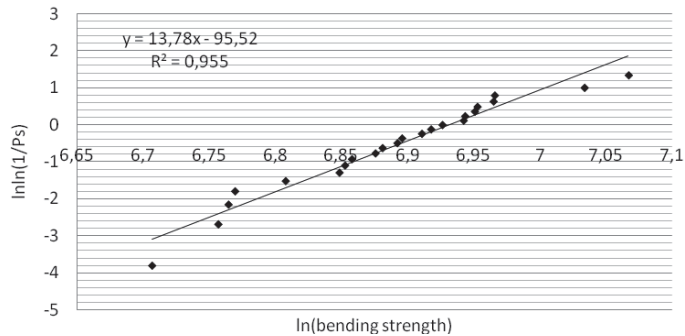


Fig. 4. Approximation of the distribution of probability of strength to 3-point bending of zirconium dioxide

Fig 4 presents the plot of empirical function of reliability; the Weibull distribution functions and in terms of bending strength. The plot shows an additional line of damage probability $P_f = 0.632$ which corresponds to strength σ_o .

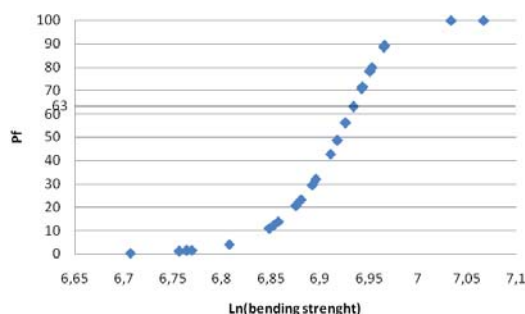


Fig. 5. Function of reliability of zirconium dioxide in terms of bending strength

Summary

The statistical analysis of the results of the present research can facilitate taking the decision of evaluating the risk taken every day in dental surgeries. As for dental materials used for that purpose, the Weibull distribution analysis is used. The distribution is one of the models of probability distribution for damage analysis. The Weibull distribution modulus, referred to as the shape parameter, is assumed as an element of variation in the material strength. The other parameter, referred to as the Weibull distribution scale parameter σ_0 , defines a characteristic material strength value for which 63.2% of the elements made from a given material get damaged. As for our studies, it was found, by a comparison of the descriptions of with normal and the Weibull distribution, that a slightly statistically stronger description provides the use of normal distribution. One could therefore claim that recommending the normative application of the Weibull distribution for the analysis of the results of 3-point dental materials, including zirconium dioxide, has not been confirmed.

At that stage it is difficult to evaluate the cause of a considerable scatter of the studies results and in the scope investigated the variation in the size of the cross-section of the specimens in terms of the size effect on the strength results.

References

- [1] A. M. Niewczas, D. Pieniak, P. Ogrodnik, *Analiza niezawodnościowa wytrzymałości kompozytów stomatologicznych poddanych zróżnicowanym procedurom fotopolimeryzacji, Eksploatacja i niezawodność*, Vol 14, No. 3, (2012) p. 249 - 264
- [2] Pick B., Meira J.B.C., Driemeier L., Braga R.R. *A critical view on biaxial and shortbeam uniaxial flexural strength tests applied to resin composites Rusing Weibull, fractographic and finite element analyses Dent Mater* 2010; 26: 83-90
- [3] Della Bona A. *Characterizing ceramics and the interfacial adhesion to resin: I – The relationship of microstructure composition, properties and fractography J Appl Oral* 2005; 13: 1-9
- [4] Ritter J.E. *Critique of test methods for lifetime predictions Dent. Mater.* 1995; 11: 147-151
- [5] Norm PN-EN 843 – 1: *Techniczna ceramika zaawansowana, Właściwości mechaniczne ceramiki monolitycznej w temperaturze pokojowej, Part 1: Oznaczanie wytrzymałości na zginanie*
- [6] Norm PN-EN 843 – 5: *Techniczna ceramika zaawansowana, Właściwości mechaniczne ceramiki monolitycznej w temperaturze pokojowej, Part 5: Analiza statystyczna*



VIBRATION SUPPRESSION PROBLEMS IN NON-RIGID STRUCTURES TAKING A VIBRATING SIFTER AS AN EXAMPLE

Janusz Zachwieja

*University of Technology and Life Sciences,
Department of Applied Mechanics, Mechanical Engineering Faculty
str. S.Kaliskiego 5, 85-796 Bydgoszcz
email: jz@zmp.com.pl*

Abstract

This paper presents the problems encountered in the suppression of vibration in machines with a low degree of rigidity, especially when the vibration is to be suppressed in only part of a facility, as the oscillatory motion of the remaining equipment in the team is its normal working movement. An example of such a device is a vibrating sifter, this being a machine with a percussive (shock) way of operating. The nature of vibrations in this type of equipment depends on the foundation's rigidity as well as the rigidity of the screen itself. Both may undergo change during operation of the machine, due to cracking of structural elements as a result of the impact of the force causing the movement of the screened material.

Keywords: *own natural vibration, vibration suppression*

1. Introduction

The motion of operating machine units such as mills, sifters and vibrating conveyors [1,2] is vibratory. Diagnosing the dynamic state of a machine with a percussive (shock) operation is a complex issue due to the presence in the system of excitations of considerable amplitudes and frequencies acting not only on the whole operating unit but also on other components of the machine and the environment, which is an undesirable effect. The design of such machines should provide good vibration insulation for the working components. In many cases, however, this is not efficient enough to meet the demands of the machines' work environment, such as the proximity of measuring devices or the presence of people. Often the cause of the incorrect operation of these devices lies in modifications introduced in order to improve performance, or else their foundations being incorrectly constructed. The Building Law requires calculations of the load capacity of foundations for large-scale facilities such as mills or foundry hammers. The conditions governing foundations for vibrating sifters are however less stringent. Usually these are located directly on the factory floor, which is often not adapted to this role. The vibration velocity of the screen – the sifter's operating component – is in the order of $100 \text{ mm}\cdot\text{s}^{-1}$ and its displacement amounts to several millimetres. Thus the forces resulting from the mass and the acceleration of the team when in motion are significant, making it necessary to apply an effective method of insulating the machine's vibration [3].

Both the screen and the structure on which it is installed are not rigid. The effectiveness of screening depends on the sensitivity of the vibration dampers. Both these factors compound to

cause the frequency range in which own, natural vibration occurs to be broad [4,5]. Variable loads on the device's structure, causing a variable state of stress, significantly reduce the machine's endurance. The resulting cracks reduce the structure's rigidity uncontrollably. It is very likely that in these conditions, vibrations will adopt a sudden resonant nature, which involves the risk of damage to or even degradation of the structure.

2. The dynamic state of the device before upgrade of the sifter support method

The sifter support structure in the tested screen was originally made of steel sections measuring 120 mm x 120 mm with the wall thickness of 2 mm. Forced vibration by means of the action of exciters caused cracks in both the sifter body as well as the supporting steel sections.

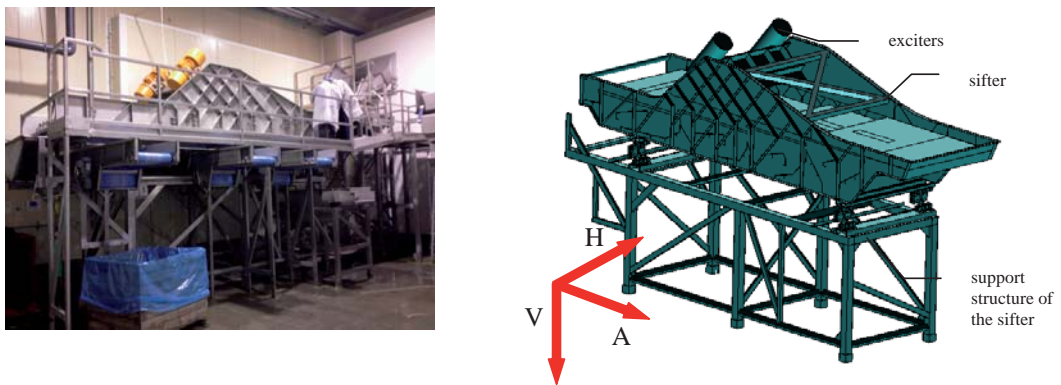


Fig. 1 View and model of a sifter and support structure unit

The kinematics of the screening process requires that the screen's vibrations force movement in the screened material along the axis of the device (Fig. 1). The purpose of the vibration dampers is to suppress the temporally variable force transmitted from the sifter to the support structure. The ideal situation would be that in which the screen's vibrations are not accompanied by vibrations in the support structure.

Figure 2 illustrates the amplitude and frequency characteristics of the screen's and support structure's vibration velocity, indicated on the basis of vibration velocity waveforms.

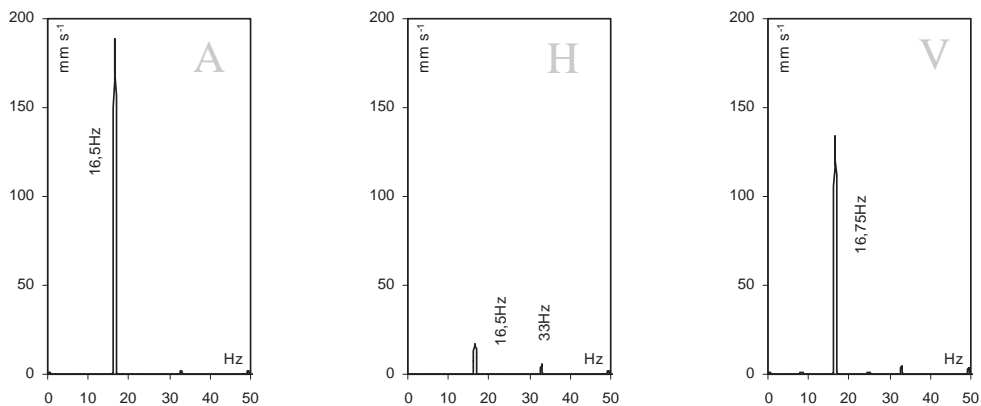


Fig. 2. The amplitude and frequency characteristics of a screen's vibration velocity

The design of the vibration dampers with spring component causes them to exhibit sensitivity in a vertical direction and along the axis of the screen. In the direction perpendicular to the axis,

the vibration damper is rigid, and therefore is not designed to transmit loads. The method used to mount the exciters on the screen's beam in this sifter results in an impermissible excitation direction. Consequently, despite correctly selected vibration damper characteristics, significant vibration velocity amplitudes are observed in the structure in a direction perpendicular to the sifter's axis (Figure 3).

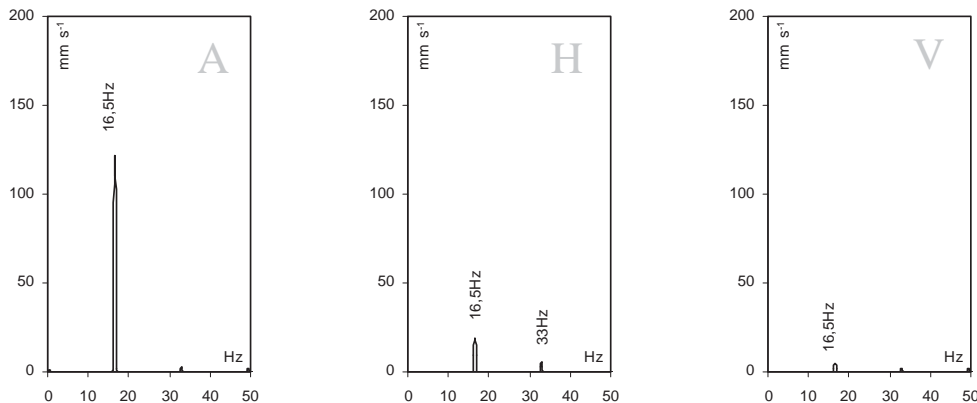


Fig. 3. The amplitude and frequency characteristics of the vibration velocity in a screen's support structure

These vibrations are orbital resonant in nature. The occurrence of this phenomenon is confirmed by resonant characteristics obtained on the basis of vibration velocity waveforms during the coasting and running of the device.

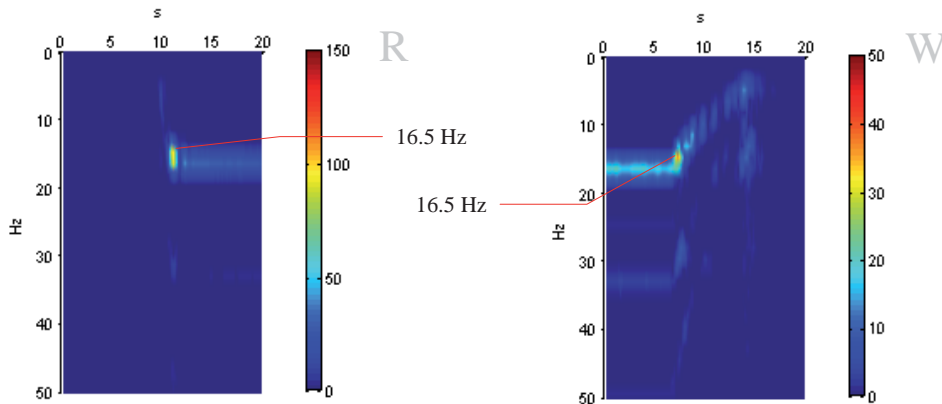


Fig. 4. The screen's short term Fourier vibration velocity transforms during the device's running (R) and coasting (W)

It can be seen in the spectrograms (Fig. 4) that the resonant frequency is slightly lower than the excitation frequency caused by the exciters (16.5 Hz).

Numerous cases of structural damage to the screen support structure forced a change in the way it is supported. The requirements that were imposed in the design assumptions included not only a high degree of rigidity but also simplicity of shape and corrosion resistance of the material from which the structure's components would be made. The latter requirement was imposed by sanitary regulations.

3. The dynamic state of the device following upgrade of the screen support method

Finally, from the many options under consideration [6], the solution shown in Figure 5 was selected.

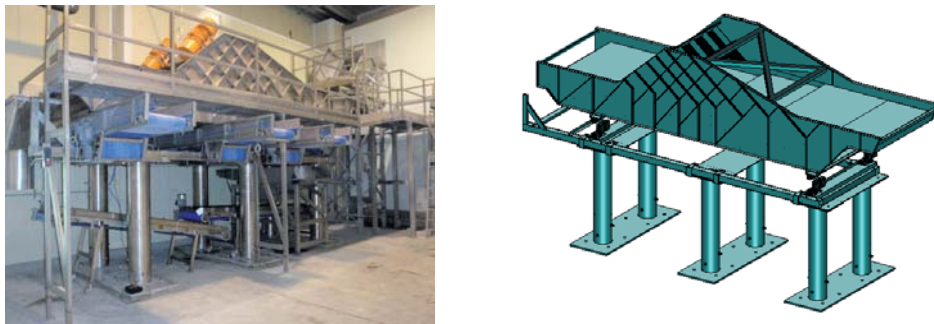


Fig. 5. View and model of the screen support structure after upgrading

Based on the weight of the screen and impact of the exciters, it was calculated at the design stage that the stresses in the cross-sections of the upgraded structure should not exceed 40 MPa. The specified value of the stresses is so low that for the material from which the components are made (namely 1.4301 grade steel), the figure does not exceed the limit even for variable loads. The maximum deformation of the screen's support columns should be less than 1 mm. The support structure's high degree of rigidity following its upgrade is confirmed by the expected frequency of its own natural vibrations - 54 Hz (Fig. 6).



Fig. 6. The lowest expected frequency of the screen support structure's own, natural vibrations following its upgrade and the stresses and strains in cross-sections

Tests of the screen's dynamics were performed following its installation on the upgraded support structure. Based on the amplitude and frequency characteristics of vibration parameters, it can be claimed that the intended effect, namely a significant reduction in the level of vibration in the support structure, while maintaining the screen's required vibration velocity parameters, was successfully achieved (Figs. 7-8).

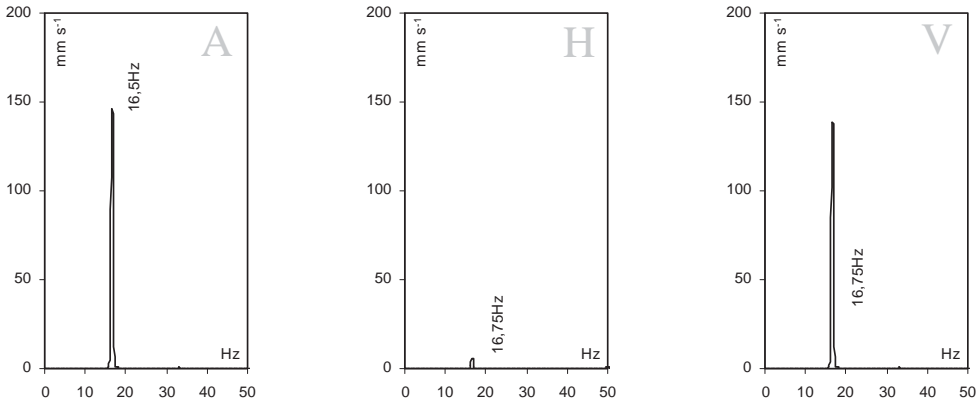


Fig. 7. The amplitude and frequency characteristics of the screen's vibration velocity following the upgrade

The figures for vibration amplitudes in the direction of the screen's axis and in the vertical direction are similar and also are similar to the corresponding parameters measured before the upgrade. This is a beneficial effect, as it means that the screening performance, which is a function of the screen vibration velocity, did not undergo any change. However, the level of screen vibrations in the direction perpendicular to its axis was reduced considerably. This phenomenon is also advantageous in view of the fact that the vibration dampers do not exhibit any suppression properties in this direction.

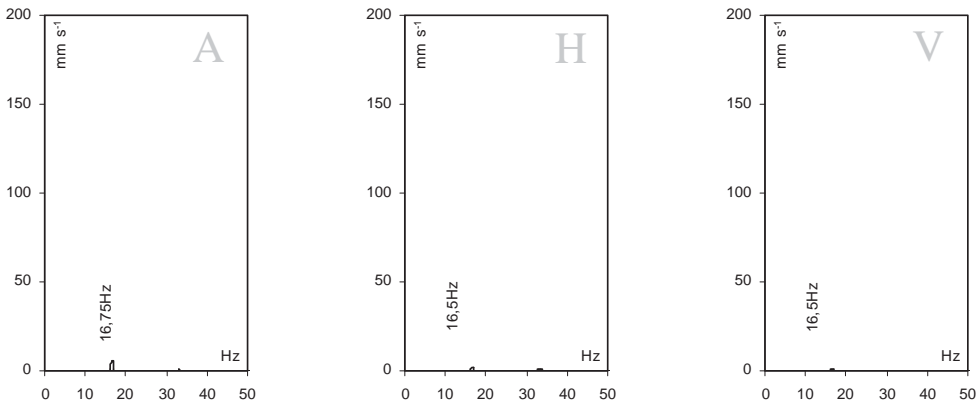


Fig. 8. The amplitude and frequency characteristics of the screen support structure's vibration velocity following the upgrade

The vibration velocity amplitudes of the support structure were dramatically reduced, as illustrated by Figure 8. At low support structure vibration parameters and optimum screen vibration parameters for the production process, the set-up operated for a period of four days. Then, following the failure and repair of one of the exciters, the screen's vibration level changed very rapidly, as shown by the amplitude and frequency characteristics of vibration velocities presented in Figure 9.

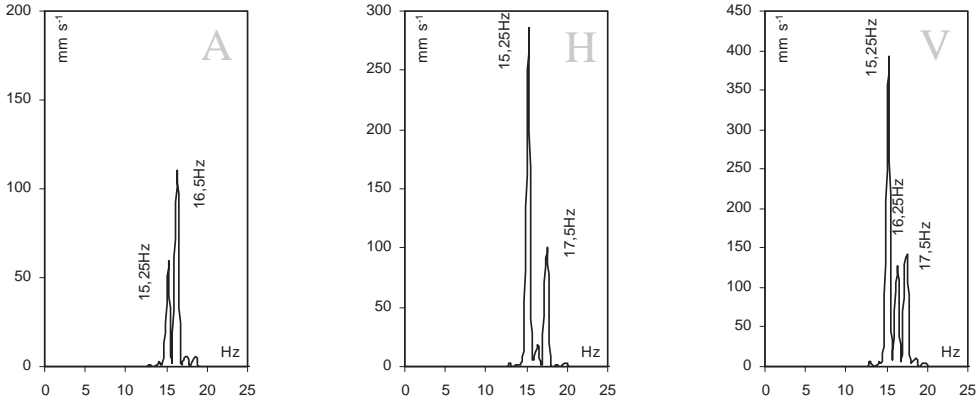


Fig. 9. The amplitude and frequency characteristics of the screen's vibration velocity following the failure of the exciter

While in the direction of the screen's axis the vibration amplitude for the excitation frequency was slightly reduced, it grew rapidly in the vertical direction and in the direction perpendicular to the screen's axis in case of the 15.25 Hz and 17.5 Hz frequencies. The occurrence of very large vibration amplitudes at the frequency of 15.25 Hz would indicate that this is a resonant frequency. Comparison of the charts (Figures 7 and 9) suggests that before the failure of the exciter, the rigidity of the unit must have been greater, and then was reduced, due to which the frequency of resonant vibrations also decreased. Reduction in the rigidity may be linked to the damage to one of the exciters, as for a few hours the screen was subjected to a force perpendicular to its axis. Under normal operating conditions, i.e. when two exciters are in operation, this force does not occur. However, it is puzzling that the vibration spectra presented in Figure 7 show no visible amplitudes for own, natural frequencies in the area of excitation frequencies, which may mean that the suppression in the system is considerable. It must have been reduced, since the amplitudes of resonance vibrations with a frequency of 15.25 Hz show large values at an excitation frequency greater by only 1 Hz. This effect must be considered inexplicable.

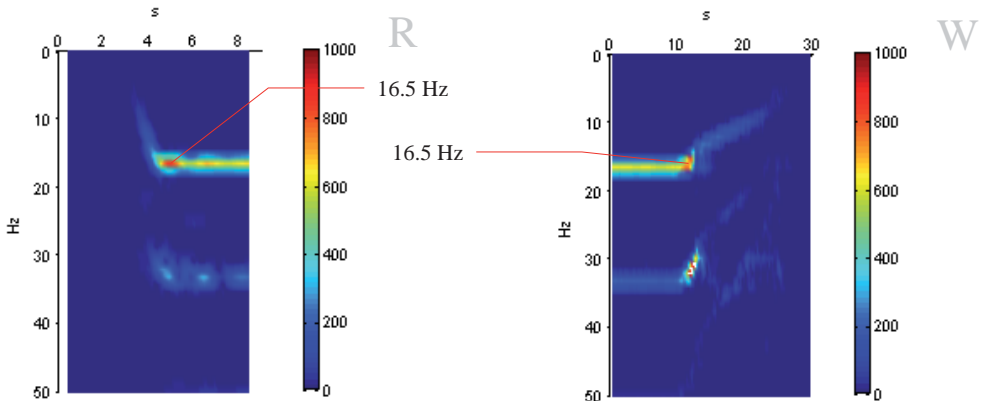


Fig. 10. The screen's short term Fourier vibration velocity transforms as indicated during the device's running (R) and coasting (W) following the failure of the exciter

The screen's vibration velocity spectrograms prove that the frequency of the screen's own, natural vibrations changed following the upgrade of the support structure. Figure 4 shows that prior to the upgrade, the resonance frequency was smaller than the rotational frequency of the exciters and that presently, the excitation frequency falls within the range of orbital resonance

frequencies. This statement is supported by the fact that an amplitude for an ultra-harmonic frequency 2 x the excitation frequency occurs in the vibration velocity spectrum.

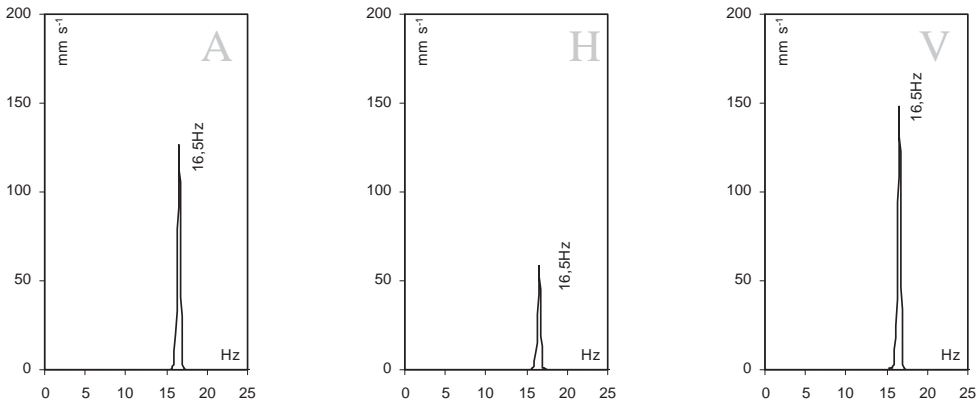


Fig. 11. The amplitude and frequency characteristics of the screen’s vibration velocity following the attachment of mass weighing 1500 N

Also inexplicable is the unit’s reaction to the addition of a weight ~ 1500 N to the front section of the screen, as illustrated by the vibration velocity spectra shown in Figure 11. These show that the frequency of the own, natural vibrations in the vertical direction, amounting to 15.25 Hz, decreased and that these vibrations were effectively damped. But this would in turn contradict the argument of the unit’s poor suppression properties. As a result, the level of the screen’s vibrations in the vertical direction and in the direction of its own axis is similar to that measured in the tests carried out immediately after the device’s start-up, while the level of vibrations in the direction perpendicular to the screen’s axis is very high.

4. Analysis of the causes for changes in the device’s natural vibration frequencies

The effect of the added weight and possible change in the screen’s rigidity on the frequency of its own, natural vibrations was the subject of a numerical modelling study. Two beams each weighing 1400 N were attached to the screen’s base. This procedure was intended to determine which is the prevailing direction of changes. Because on the one hand, an increase in the mass of the unit should result in a reduction in the frequency of its own, natural vibrations, while on the other hand one should expect this to increase as an effect of stiffening the structure. The calculated frequencies of resonant vibrations before the screen’s reinforcement are presented in Figure 12.

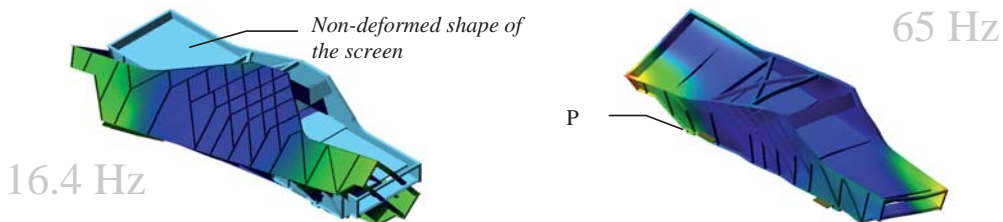
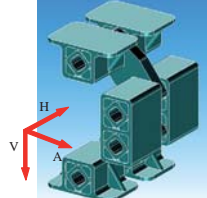


Fig. 12. The frequencies and forms of the screen’s vibrations without stiffening

These frequencies can be considered as characteristic for two reasons. The frequency 16.4 Hz is the highest vibration frequency of the screen-vibration dampers unit when the screen is treated as a rigid body. A frequency of 65 Hz is the lowest screen vibrations frequency when the screen is treated as a pliable body.

Table 1. Rigidity of vibration dampers

	Vibration damper rigidity (N mm^{-1}) in the direction:		
	A	H	V
	170	340	6500

Calculations show that for a screen weight of $\sim 35000 \text{ N}$ and a rigidity of dampers as shown in Table 1, resonant vibrations occur at an excitation frequency of 16.5 Hz . The module for the exciter's excitation force used for the computation is 64 kN . Inclining the exciters at an angle of 0.25π causes the force acting on the structure in the horizontal direction and along the screen's axis to have a module of $\sim 50 \text{ kN}$, while in the direction of the axis perpendicular to the screen's axis this figure is 64 kN . This corresponds to the listed figures in the catalogue for the ROSTA Company's exciters used to power the screen. These forces are vectors rotating in opposite directions. Such a direction of rotation means that with a uniform imbalance of the exciters' discs, the projections of centrifugal forces in a straight direction and perpendicular to the sifter's axis create a double zero, while in other directions the resultant vector module has a value of $\sim 100 \text{ kN}$.

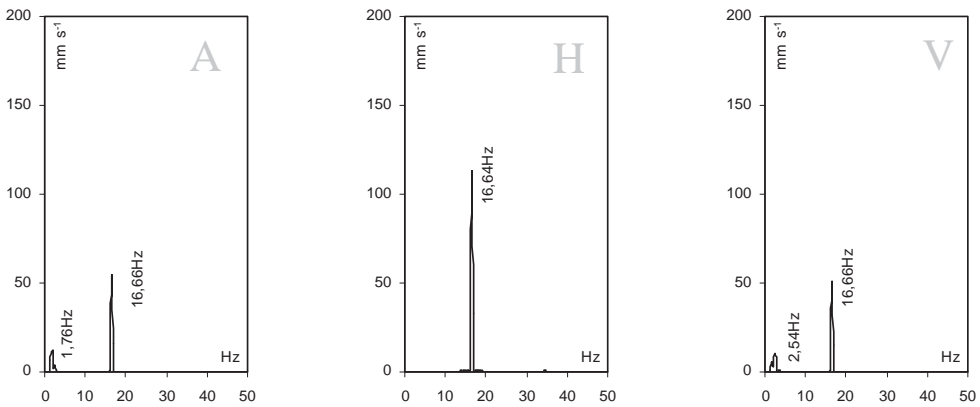


Fig. 13. The amplitude and frequency characteristics of the screen's vibration velocity at point P before attaching extra weights

The vibration spectra shown in Figure 13 refer to the point marked in Figure 12 with the symbol P - a point located on the screen's rear beam near the vibration damper's mounting. The effect of the added weights on the nature of the screen's vibrations is presented in figures 14 and 15.

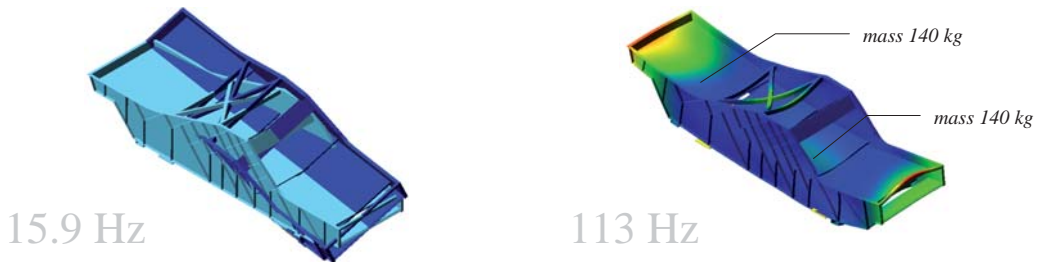


Fig. 14. The frequency and form of the screen's vibrations after adding weights

As one might expect, stiffening did not affect the form of the screen's own, natural vibrations when it was treated as a rigid body. Only the resonant frequency changed slightly. It is worth noting that the attached weight, amounting of 8% of the screen's weight, reduced its resonant frequency by only about 0.5 Hz.

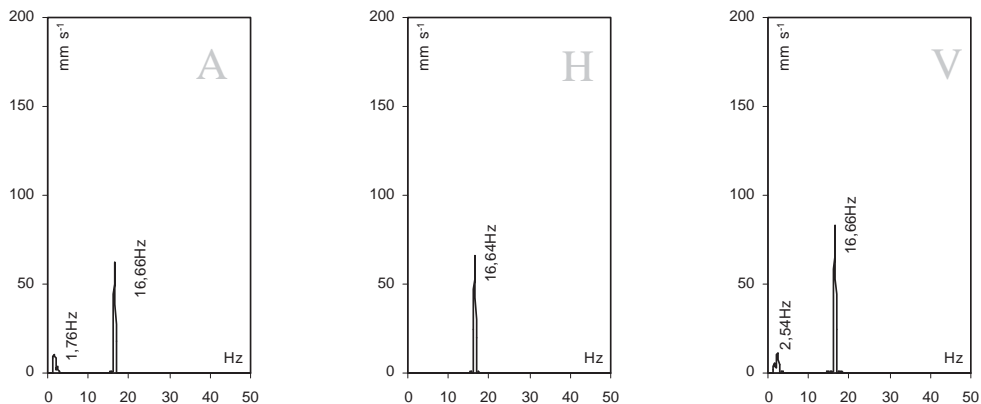


Fig. 15. The amplitude and frequency characteristics of the screen's vibration velocity at point P following attachment of the weights

However, the nature of vibrations changed significantly when the screen was treated as a sensitive body. There is no longer a tendency visible in Figure 12 to torsional vibrations of the screen body, while the frequency of its own, natural vibrations increased almost twofold.

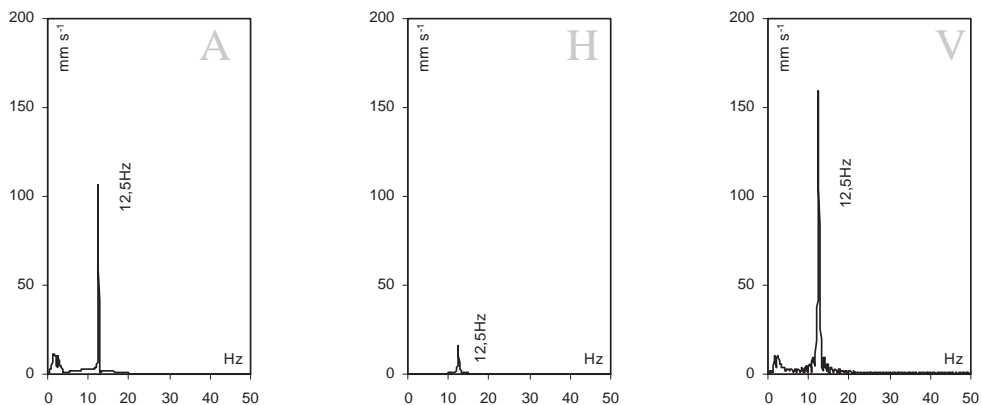


Fig. 16. The amplitude and frequency characteristics of the screen's vibration velocity at point P following a change in the excitation frequency of the exciters

A much better effect than resonance vibration suppression by means of weights is achieved by changing the excitation frequency. This can be seen on the vibration velocity spectra presented in Figure 16. Lowering the excitation frequency by 4 Hz causes the unit to move away from the resonance area. The effectiveness of the screening process will be maintained, because the amplitudes of the vibrations velocity, apart from the direction perpendicular to the screen's axis, exceed $100 \text{ mm}\cdot\text{s}^{-1}$. If, however, it turned out that these figures are too low, one may increase the amount of imbalance in the discs of the exciters.

5. Conclusions

Both the results of testing the nature of the sifter's vibrations as well as the results obtained on the basis of numerical modelling show that suppression for this type of machine is not a simple issue. For example, changing the rigidity of the screen radically affects the sifter's vibration frequency only in relation to the vibrations of a continuous unit. Lower frequencies of own, natural vibrations resulting from treatment of the screen as a rigid body are not substantially changed. The attachment of a weight of 2800 N, representing less than 10% of the screen's weight, reduced the resonance frequency by a mere 0.5 Hz. Although suppression by means of added weights made it possible to remove the unit from the area of resonant vibration, this exhibited a high degree of unpredictability in the obtained results in respect of changes in vibration amplitudes in directions in which resonance did not occur. This effect was observed during tests of the sifter. The dynamic state represented by the amplitude and frequency characteristics in Figure 12 is the best result of transferring weights to various points on the screen. The results of numerical calculations show that a satisfactory suppression effect is achieved by changing the excitation frequency. Vibration amplitudes in directions A and V remained high, which ensures the proper performance of the screening process, while at the same time the vibration velocity amplitude of the sifter in a direction perpendicular to its axis was reduced. This is advantageous, since it ensures lower stress values in the screen's cross-sections. This is because the structure of the vibration dampers used does not provide the proper vibration suppression conditions in this direction.

References

- [1] Chmielewski T., Zembaty Z., *Podstawy dynamiki budowli*, Arkady, Warszawa, 1998.
- [2] Borkowski W., Konopka S., Prochowski L., *Dynamika maszyn roboczych*, WNT, Warszawa, 1996.
- [3] Zachwieja J., Gołębiowska I., *Efektywność wybranych metod ochrony przeciwdrganiowej konstrukcji wsporczej separatorów*, Budownictwo Ogólne, Wydawnictwa UTP, pp. 119-126, 2009.
- [4] Zachwieja J., Gołębiowska I., *Damping building vibrations excited by surface wave propagating in the ground*. Journal of Polish CIMAC, 7(3), 2012, s. 373-381.
- [5] Praca zbiorowa, *Wspomaganie konstruowania układów redukcji drgań i hałasu*, WNT, Warszawa, 2001.
- [6] Zachwieja J., *Application of numerical analysis in dynamic state diagnosis of the machine with a shock character of operation*, Diagnostyka, 63, pp. 63-68, 2012.